

NASA GRANT  
NSG-1023

*N 76-22827*

# GRAVITY SHEAR WAVES ATOP THE CIRRUS LAYER OF INTENSE CONVECTIVE STORMS

BY JAMES G. STOBIE,  
Captain, U.S.A.F.

PRINCIPAL INVESTIGATOR: PETER C. SINCLAIR



US ISSN 0067-0340

Atmospheric Science

PAPER NO.

246



DEPARTMENT OF ATMOSPHERIC SCIENCE  
COLORADO STATE UNIVERSITY  
FORT COLLINS, COLORADO

GRAVITY SHEAR WAVES ATOP THE CIRRUS  
LAYER OF INTENSE CONVECTIVE STORMS

BY

James G. Stobie

Preparation of this report  
has been financially supported by

NASA Grant NSG-1023

Principal Investigator: Peter C. Sinclair

Department of Atmospheric Science

Colorado State University

Fort Collins, Colorado

December, 1975

## ABSTRACT

Recent visual satellite photographs of certain intense convective storms have revealed concentric wave patterns. These waves appear as undulations in the top of the cirrus outflow of such storms, and are usually centered about the area of the most intense convection. They appear in both mid-latitude and tropical storms. This report analyzes two mid-latitude and three tropical cases of these waves.

A model for the generation and growth of these waves is proposed. The proposed initial generating mechanism is similar to the effect noticed when a pebble is dropped into a calm pond. The penetration of the tropopause by overshooting convection is analogous to the pebble's penetration of the water's surface. The model for wave growth involves instability due to the wind shear resulting from the cirrus outflow. This model is based on an equation for the waves' phase speed which is similar to the Helmholtz equation. It, however, does not assume an incompressible atmosphere, but rather assumes density is a logarithmic function of height.

Finally, the model is evaluated on the two mid-latitude and three tropical cases. The data indicate that shearing instability may be a significant factor in the appearance of these waves.

## ACKNOWLEDGMENTS

The author would like to express his deep gratitude to Maj. Charles P. Arnold for his support throughout the preparation of this paper. Not only did Maj. Arnold first introduce the described phenomenon to the author, but he also provided the theoretical hypothesis upon which this paper was developed. In addition, thanks are expressed to Drs. Peter C. Sinclair, William M. Gray, and Paul Mielke for reviewing the manuscript. Appreciation is also extended to Dr. Earl Gossard for his helpful suggestions regarding the theoretical aspects of the paper. A special thanks is extended to Ms. Karen Ray for typing the manuscript.

This research was sponsored by NASA Grant NSG-1023. The author's enrollment at Colorado State University was sponsored by the Air Force Institute of Technology.

## TABLE OF CONTENTS

<u>Section</u>	<u>Page</u>
ABSTRACT . . . . .	i
ACKNOWLEDGMENTS . . . . .	ii
LIST OF TABLES . . . . .	iv
LIST OF FIGURES . . . . .	v
LIST OF SYMBOLS . . . . .	ix
1 INTRODUCTION . . . . .	1
1.1 Scope and Purpose . . . . .	1
1.2 Historical Background . . . . .	1
2 OBSERVED WAVE CHARACTERISTICS . . . . .	6
3 THEORIES OF WAVE GENERATION AND GROWTH . . . . .	12
3.1 Wave Generation . . . . .	12
3.2 Wave Stability Model . . . . .	17
4 DATA ANALYSIS TECHNIQUES . . . . .	38
4.1 Mid-Latitude . . . . .	38
4.2 Tropical . . . . .	46
5 CASE STUDIES . . . . .	48
5.1 Nebraska . . . . .	48
5.2 Kansas . . . . .	68
5.3 Tropical Cases . . . . .	84
6 ERROR ANALYSIS . . . . .	94
6.1 Measurement Errors . . . . .	94
6.2 Stability Model Errors . . . . .	97
7 SUMMARY AND CONCLUSIONS . . . . .	99
8 SUGGESTIONS FOR FURTHER STUDY . . . . .	102
REFERENCES . . . . .	103
APPENDIX A: AMPLITUDE MEASUREMENT TECHNIQUE . . . . .	106
APPENDIX B: SELECTION OF SIGN FOR $\beta_1$ . . . . .	110

LIST OF TABLES

<u>Table</u>		<u>Page</u>
4.1	Mid-Latitude Data Sources . . . . .	38
4.2	Tropical Data Sources . . . . .	47
5.1	Nebraska Case Cloud Measurements . . . . .	51
5.2	Thermal Parameters for Nebraska Case . . . . .	56
5.3	Kansas Case Cloud Measurements . . . . .	78
5.4	Thermal Parameters for Kansas Case . . . . .	80
5.5	Observations from Tropical Cases . . . . .	84
5.6	Thermal Parameters for Tropical Cases . . . . .	88

LIST OF FIGURES

<u>Figure</u>		<u>Page</u>
1.1	Model for parcel motions within a quasi-steady state overshooting dome . . . . .	2
1.2	Apollo 9 photograph of waves atop the cirrus outflow of a thunderstorm . . . . .	3
2.1	SMS-2 visual photograph taken over Kansas at 2348Z, June 18, 1975 . . . . .	7
2.2	SMS-2 visual photograph taken over Nebraska at 0032Z, June 19, 1975 . . . . .	8
2.3	Skylab visual photograph of Tropical Storm Ellen (Pacific, 1973) . . . . .	9
2.4	DMSP visual photograph of Typhoon Bess taken at 2230Z, October 10, 1974 . . . . .	10
2.5	DMSP visual photograph of Typhoon Kit taken at 2230Z, January 4, 1972 . . . . .	11
3.1	SMS-2 visual photograph taken over Nebraska at 0102Z, June 19, 1975 . . . . .	13
3.2	Model for parcel motions caused by a collapsing turret . . . . .	14
3.3	Alternate model for motions within a quasi-steady state dome . . . . .	15
3.4	Observed cloud particle motions on an overshooting turret . . . . .	16
3.5	Diagram of typical concentric wave pattern . . . . .	19
3.6	Vertical profiles of $T$ , $\theta$ , $u_0$ , and $\rho$ for stability model . . . . .	20
3.7	Sample curves of $c_r$ , $ c_1 $ , and $\beta_1$ versus $\Delta u_0$ . . . . .	36
4.1	Map showing area of data coverage for the mid-latitude cases . . . . .	39
4.2	SMS-2 visual photograph with map grid, taken at 0102Z, June 19, 1975 . . . . .	40
4.3	Blow up of Figure 4.2 without map grid . . . . .	42

<u>Figure</u>		<u>Page</u>
4.4	Temperature sounding from North Platte, Nebraska taken at 0000Z, June 19, 1975 . . . . .	44
5.1	Path of tornadoes spawned by Nebraska storm on June 18, 1975 . . . . .	48
5.2	SMS-2 visual photographs taken over the Kansas-Nebraska area on June 18, 1975 . . . . .	49
5.3	Grand Island, Nebraska radar summaries during period of tornado activity . . . . .	50
5.4	SMS-2 visual photograph taken over Nebraska at 2317Z, June 18, 1975 . . . . .	52
5.5	SMS-2 visual photograph taken over Nebraska at 0102Z, June 19, 1975 . . . . .	53
5.6	SMS-2 visual photograph taken over Nebraska at 0132Z, June 19, 1975 . . . . .	54
5.7	SMS-2 visual photograph taken over Nebraska at 0147Z, June 19, 1975 . . . . .	55
5.8	Temperature sounding from North Platte, Nebraska taken at 0000Z, June 19, 1975 . . . . .	57
5.9	Wind profiles from North Platte, Nebraska sounding at 0000Z, June 19, 1975 . . . . .	57
5.10	Winds at 35,000 ft over the Western United States at 0000Z, June 19, 1975 . . . . .	58
5.11	$ c_i $ and $c_r$ versus $\Delta u_o$ for selected $\lambda$ (Nebraska case) . . . . .	61
5.12	$ c_i $ versus $\Delta u_o$ for selected $\lambda$ (Incompressible model, Nebraska case) . . . . .	62
5.13	$\psi$ versus $\lambda$ curve for selected $\Delta u_o = 20$ m/sec (Nebraska case) . . . . .	63
5.14	Right hump of $\psi$ versus $\lambda$ curves for selected $\Delta u_o$ 's (Nebraska case) . . . . .	64
5.15	Left hump of $\psi$ versus $\lambda$ curves for selected $\Delta u_o$ 's (Nebraska case) . . . . .	65
5.16	$\Delta u_o$ versus $\lambda$ curves for selected $\psi$ at $t = 30$ min (Nebraska case) . . . . .	66

<u>Figure</u>		<u>Page</u>
5.17	Dispersion curve for $\Delta u_0 = 10$ m/sec (Nebraska case) . . . . .	68
5.18	Garden City, Kansas radar summaries from June 18-19, 1975 . . . . .	70
5.19	SMS-2 visual photograph taken over Kansas at 2317Z, June 18, 1975 . . . . .	72
5.20	SMS-2 visual photograph taken over Kansas at 2348Z, June 18, 1975 . . . . .	73
5.21	SMS-2 visual photograph taken over Kansas at 0002Z, June 19, 1975 . . . . .	74
5.22	SMS-2 visual photograph taken over Kansas at 0017Z, June 19, 1975 . . . . .	75
5.23	SMS-2 visual photograph taken over Kansas at 0032Z, June 19, 1975 . . . . .	76
5.24	SMS-2 visual photograph taken over Kansas at 0047Z, June 19, 1975 . . . . .	77
5.25	Temperature sounding from Dodge City, Kansas taken at 0000Z, June 19, 1975 . . . . .	79
5.26	Wind profiles from Dodge City, Kansas sounding at 0000Z, June 19, 1975 . . . . .	79
5.27	Right hump of $\psi$ versus $\lambda$ curves for selected $\Delta u_0$ 's (Kansas case) . . . . .	81
5.28	Left hump of $\psi$ versus $\lambda$ curves for selected $\Delta u_0$ 's (Kansas case) . . . . .	82
5.29	$\Delta u_0$ versus $\lambda$ curves for selected $\psi$ at $t = 30$ min (Kansas case) . . . . .	83
5.30	DMSP visual photograph of Typhoon Gilda taken at 2300Z, June 24, 1971 . . . . .	85
5.31	DMSP visual photograph of Typhoon Rose taken at 2200Z, August 12, 1971 . . . . .	86
5.32	DMSP visual photograph of Typhoon Kit taken at 2230Z, January 4, 1972 . . . . .	87
5.33	$\Delta u_0$ versus $\lambda$ curves for selected $\psi$ at $t = 30$ min (Typhoon Gilda) . . . . .	90

<u>Figure</u>		<u>Page</u>
5.34	$\Delta u_o$ versus $\lambda$ curves for selected $\psi$ at $t = 30$ min (Typhoon Rose) . . . . .	91
5.35	$\Delta u_o$ versus $\lambda$ curves for selected $\psi$ at $t = 30$ min (Typhoon Kit) . . . . .	92
6.1	Error curves of $\psi$ versus $\Delta u_o$ for Nebraska case at $t = 30$ min and $\lambda = 11$ km . . . . .	96
A.1	Cross-sectional view of idealized wave pattern . . .	107
A.2	Top view of same wave pattern as that shown in Figure A.1 . . . . .	107

## LIST OF SYMBOLS

Vectors	Definition
$\vec{g}$	Gravity
$\vec{v}$	Velocity
$\vec{\Omega}$	Earth's angular velocity
Scalars	
$\alpha$	Specific volume
$A$	Amplitude of $U$
$\beta$	Coefficient of $z$ in solutions for $U$ , $W$ , and $P$ [see equations (3.60) and (3.95)]
$\gamma$	$C_p / C_v$
$\Gamma$	Defined in equation (3.30)
$C'$	Amplitude of $W$
$C_p$	$\left(\frac{dh}{dt}\right)_p$
$C_v$	$\left(\frac{dh}{dt}\right)_\alpha$
$c$	Phase speed
$\delta$	Constant coefficient of $z$ in exponential equation for $\rho$ . The fact that $\delta$ is constant is a basic assumption of the model.
$D$	Amplitude of $P$
$f$	Coriolis parameter
$g$	Gravity
$h$	Heat
$\theta$	Potential temperature
$i$	$\sqrt{-1}$
$K, K'$	See equations (3.84) and (3.89)
$\lambda$	Wavelength
$\mu$	$2\pi/\lambda$

ScalarsDefinition

m	See equation (3.102)
n	See equation (3.103)
$\rho$	Density
p	Pressure
P	See equation (3.27)
$\sigma$	See equation (3.69)
R	Gas constant for dry air
T	Temperature
t	Time
u	$\frac{dx}{dt}$
U	See equation (3.25)
v	$\frac{dy}{dt}$
w	$\frac{dz}{dt}$
W	See equation (3.26)
$\chi$	See equations (3.45) and (3.56)
x	Horizontal length (measured west-east)
y	Horizontal length (measured south-north)
$\psi$	Amplification factor for U, W, and P [see equation (3.105)]
z	Vertical length

Subscripts

none	Perturbation quantity (except in equations 3.1 - 3.4)
o	Mean quantity
1	Lower layer
2	Upper layer

Subscripts

Definition

i	Imaginary component
r	Real component
s	Reference value

## 1. INTRODUCTION

### 1.1 Scope and Purpose

Since the advent of meteorological satellites, interest in severe storm cloud-tops has increased. This is probably because the cloud-tops are usually all that can be seen of a storm from a satellite. This limited view, however, has exposed a number of new and striking phenomena. This report examines yet another one of these newly revealed phenomena.

In a limited number of intense convective storms, the top surface of the cirrus canopy exhibits a concentric wave pattern. These waves appear to be centered about the area of the most intense convection. They have been observed in both the mid-latitudes and the tropics.

This report proposes a physical and mathematical model, which under similar environmental conditions, would produce this type of wave pattern. The model is then evaluated by analyzing several case studies, two from the mid-latitudes and three from the tropics.

### 1.2 Historical Background

Since these waves are a relatively new discovery, research concerning them is scarce. However, a great deal of study has been carried out on other cloud-top characteristics of severe storms. In addition, much has been written on billow clouds and other gravity shear wave-type phenomena, not necessarily associated with intense convection. Pertinent developments in these two areas will be discussed in the following sections.

Severe Storm Cloud-Top Studies. In one of the earlier studies on storm tops, Roach (1967) used photographs from U-2 aircraft and other

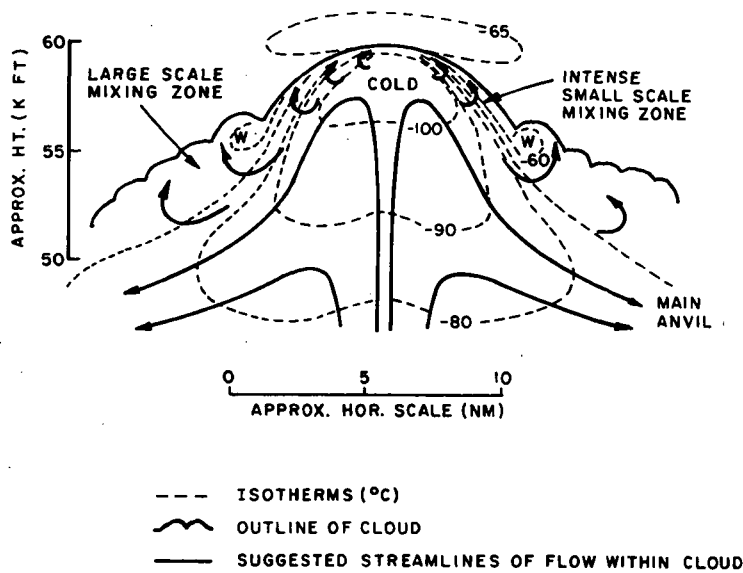


Figure 1.1. Model for parcel motions within a quasi-steady state overshooting dome. (From Roach, 1967).

synoptic data to analyze severe thunderstorm cases over Oklahoma. Using these data he deduced a model for air flow in an overshooting dome (Fig. 1.1). He also observed waves in many of the cases he studied. These waves, however, were on the domes themselves and thus, had much shorter wavelengths than those observed by satellites. He occasionally observed a warm trench, as much as 1 km deep, around the perimeter of an overshooting dome. This may be a significant factor in the generation of longer concentric waves (see section 3.1). Lee (1971), in analyzing this same data, also found the warm trench to be a significant feature. He, however, noticed it in both severe and non-severe storms.

Purdum (1971) analyzed NOAA-1 and ATS-3 satellite photographs of severe storm tops. He found a correlation between tornado occurrence and a pause in the cirrus anvil growth. Fujita (1972) studied ATS-3 photographs of a severe thunderstorm complex over Kansas. He found a correlation between tornado location and the location of an overshooting

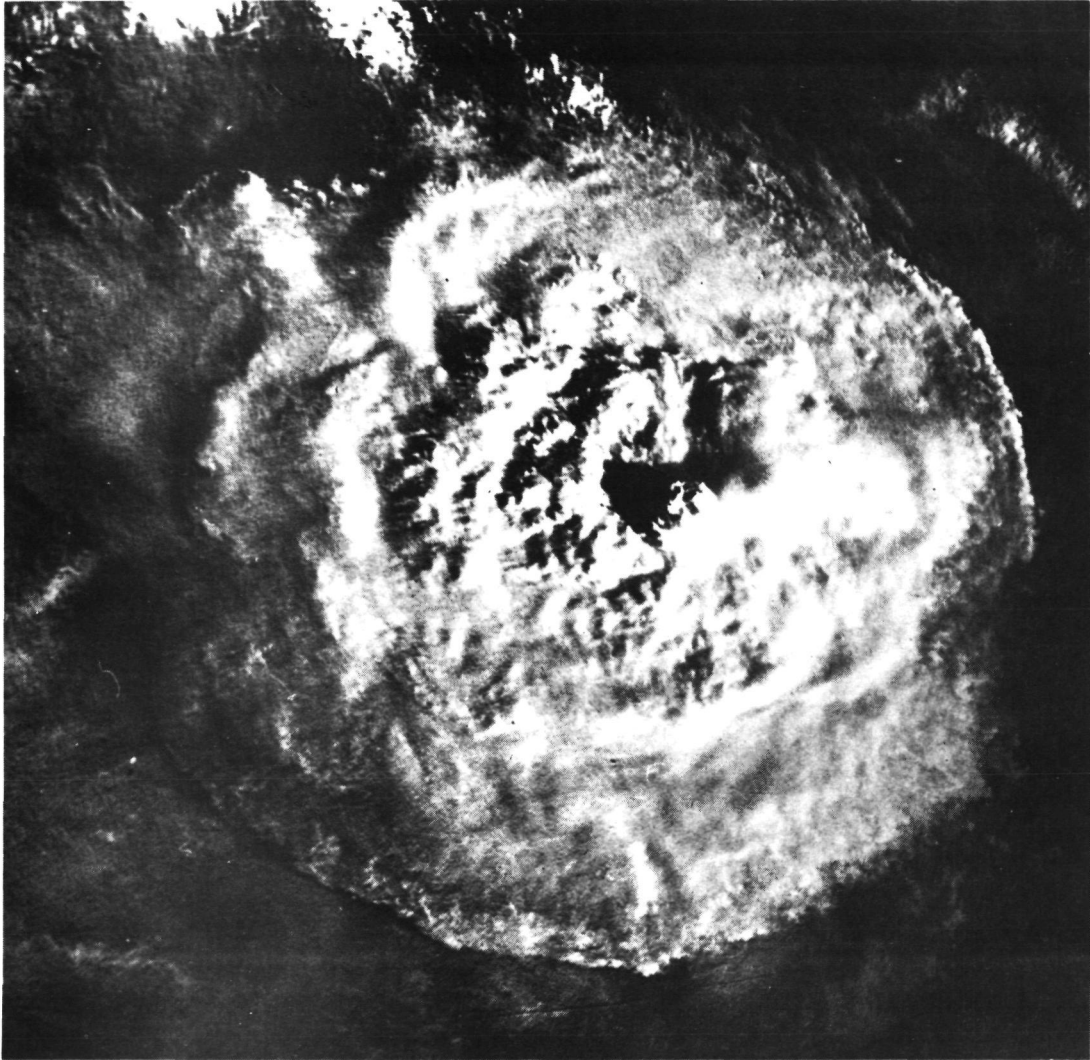


Figure 1.2. Apollo 9 photograph of waves atop the cirrus outflow of a thunderstorm. Photograph was taken over Columbia, South America, March 8, 1969. (From Fujita, 1972).

dome. The relative height of the dome, however, did not appear related to the tornado's formation. One interesting aspect of this paper is that it contained an Apollo 9 photograph of an anvil top over South America (Fig. 1.2). This photograph clearly reveals waves concentric about the storm's center. There was, however, no further discussion of these waves.

Fujita (1973) proposed a model by which a tornado would form when an overshooting dome collapsed. This was based on satellite and aircraft observations and laboratory experiments. Fujita (1974) further investigated overshooting dome characteristics. He likened the overshooting dome to the bulge that would appear on a water surface when an upward shooting jet of water was injected below the water's surface. In the course of these investigations, he never observed concentric wave patterns. In fact, he made special note of the uniformly smooth appearance of the cirrus tops in all cases. This was in spite of the presence of numerous overshooting domes. He did, however, describe the effects of the rapid collapse of an overshooting dome. These effects appear to be a feasible means of wave generation. This is elaborated on in section 3.1.

Arn (1975) studied anvil growth rates from ATS-3 and SMS-1 photographs of seven severe storms over the United States. Again concentric waves were not observed.

Arnold (1975) discussed concentric wave patterns observed in DMSP photographs of tropical storms. He stated that these patterns had been observed in DMSP photographs for some time. In fact, satellite meteorologists at Guam had been quite successful in using the focus of these waves for locating storm centers. He also postulated that they were gravity shear-type waves.

Gravity Shear Wave Theories. As was mentioned earlier, a great deal has been written about gravity shear waves. However, only those publications utilized in creating the model in section 3.2 of this report will be mentioned.

Haurwitz (1941) described the derivation of the "Helmholtz" wave equation for an incompressible atmosphere. This equation is also derived by using various other methods in Haltiner and Martin (1957), Haltiner (1971), and Gossard and Hooke (1975).

Gossard and Hooke (1975) also discussed stability criteria for a number of models for gravity shear waves. Much of their discussion is also contained in Drazin and Howard (1966). Einaudi and Lalas (1974) explored wave stability for Kelvin-Helmholtz waves.

The model described in section 3.2 of this report was first proposed by Gossard and Munk (1954) and further elaborated on in Gossard and Hooke (1975). Neither publication, however, contained a discussion of stability implications for this particular model.

## 2. OBSERVED WAVE CHARACTERISTICS

Figures 2.1 through 2.5 are visual satellite photographs of cirrus outflow layers resulting from intense convection. These photographs display wave patterns with the following characteristics:

1. The waves are visible as undulations in the top of the cirrus outflow.
2. The waves appear to form concentric arcs or rings.
3. The focal point of these arcs or rings appears to be the center of the most intense convection. This is characterized by either an overshooting dome, or in the case of Tropical Storm Ellen, by the apparent circulation center.
4. In the Nebraska and Kansas cases the waves appear in the direction of greatest cirrus outflow (Figs. 2.1 - 2.2).
5. Areas of apparent amplification may occur away from the center of convection (Fig. 2.3).
6. The range of observed wavelengths is 3.5 km (Fig. 2.5) to 14 km (Fig. 2.2).
7. The wavelength is not necessarily constant for a given cirrus outflow region. In the Nebraska case (Fig. 2.2) the wavelength increases further out from the dome center. In Tropical Storm Ellen (Fig. 2.3) the wavelength appears smaller further out from the storm center.



Figure 2.1. SMS-2 visual photograph taken over Kansas at 2348Z, June 18, 1975.

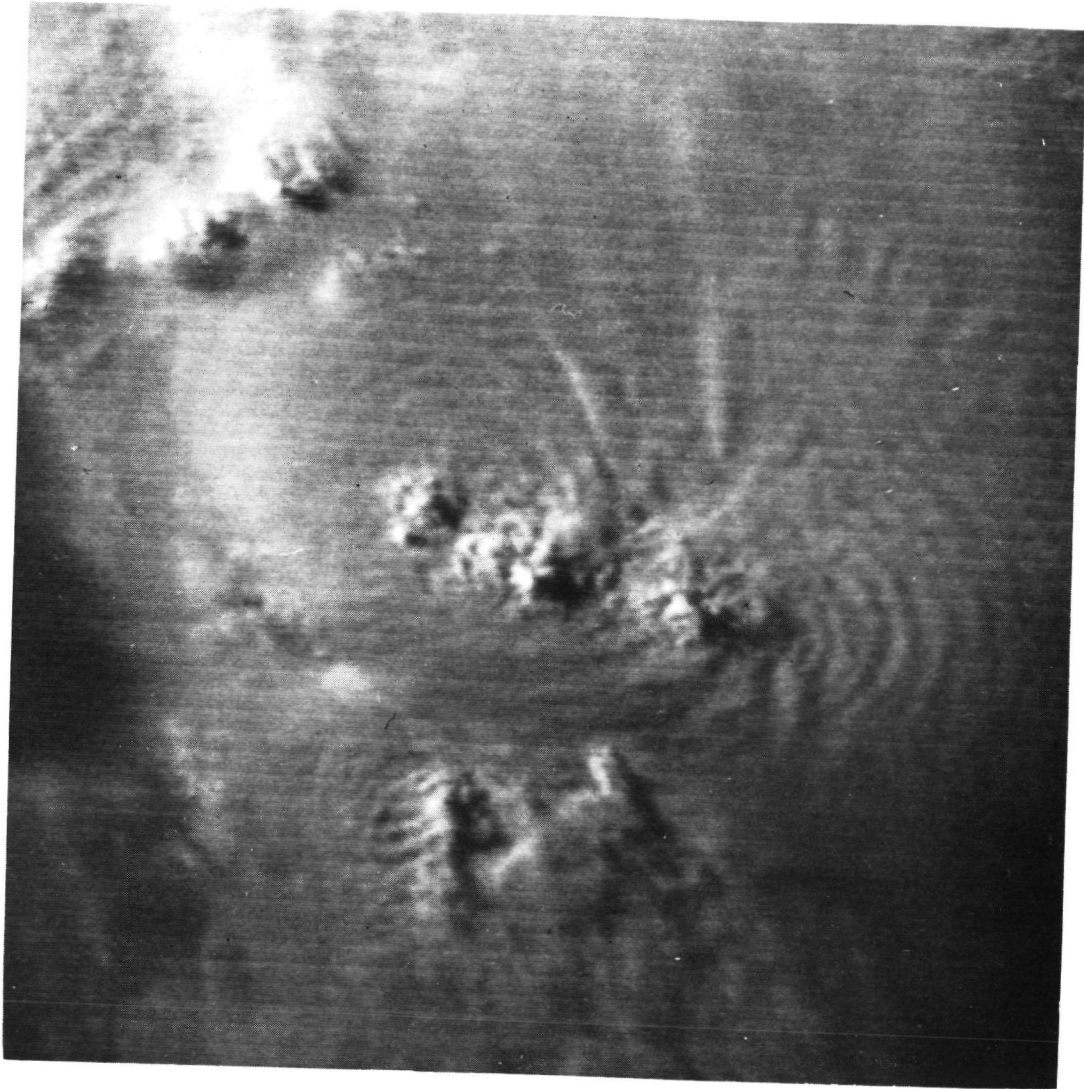


Figure 2.2. SMS-2 visual photograph taken over Nebraska at 0032Z, June 19, 1975.

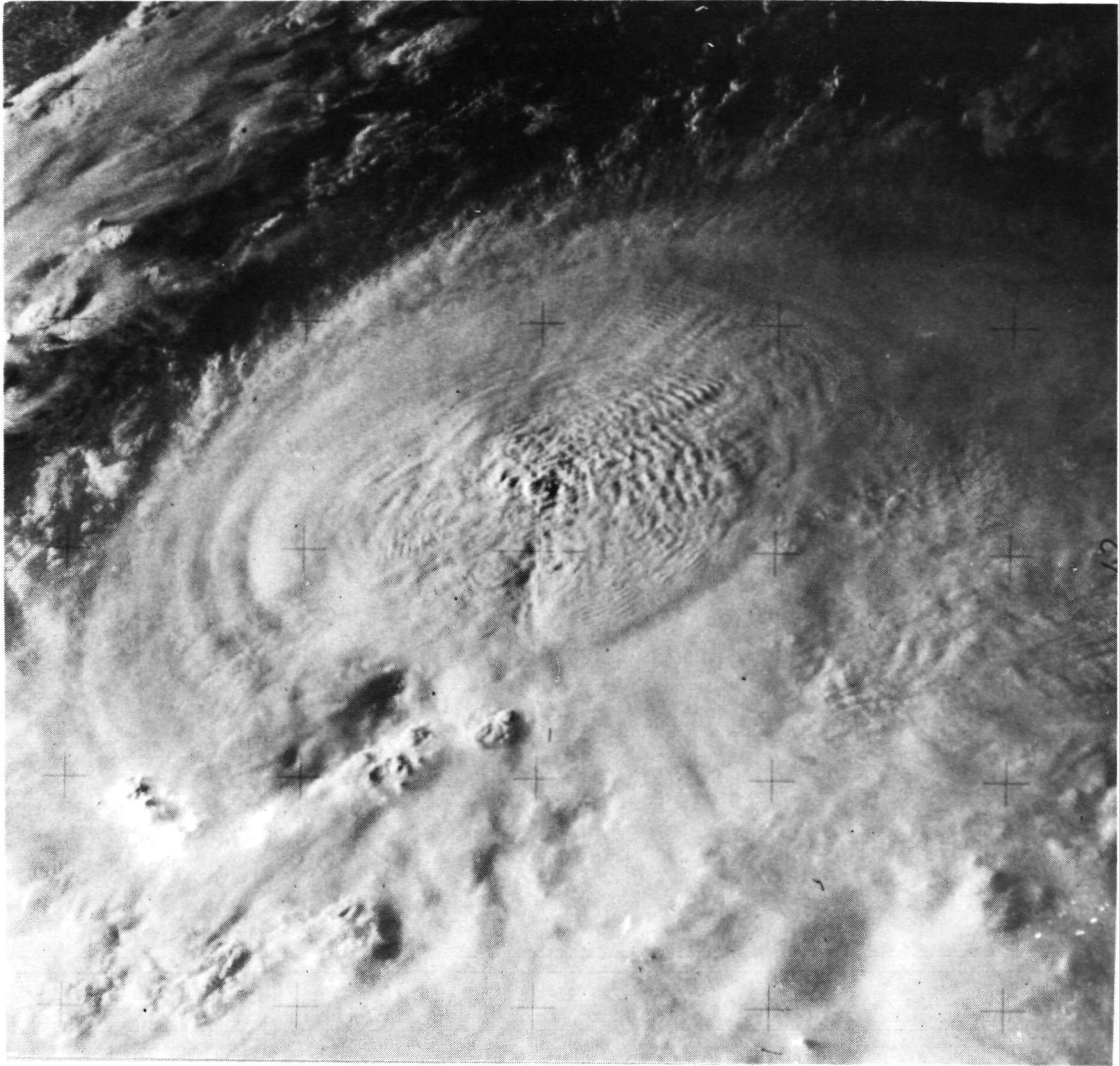


Figure 2.3. Skylab visual photograph of Tropical Storm Ellen (Pacific, 1973).

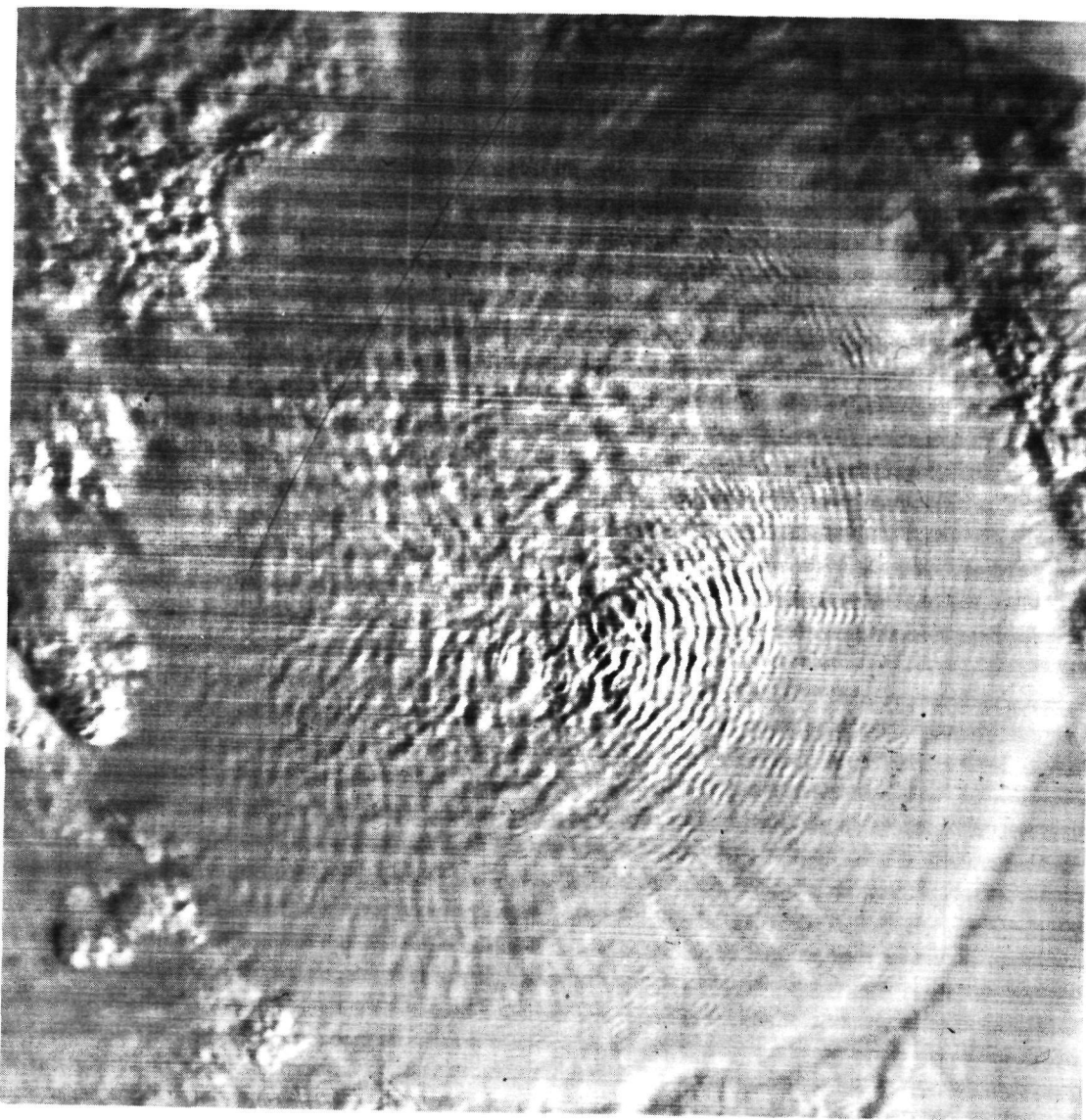


Figure 2.4. DMSP visual photograph of Typhoon Bess taken at 2230Z, October 10, 1974.

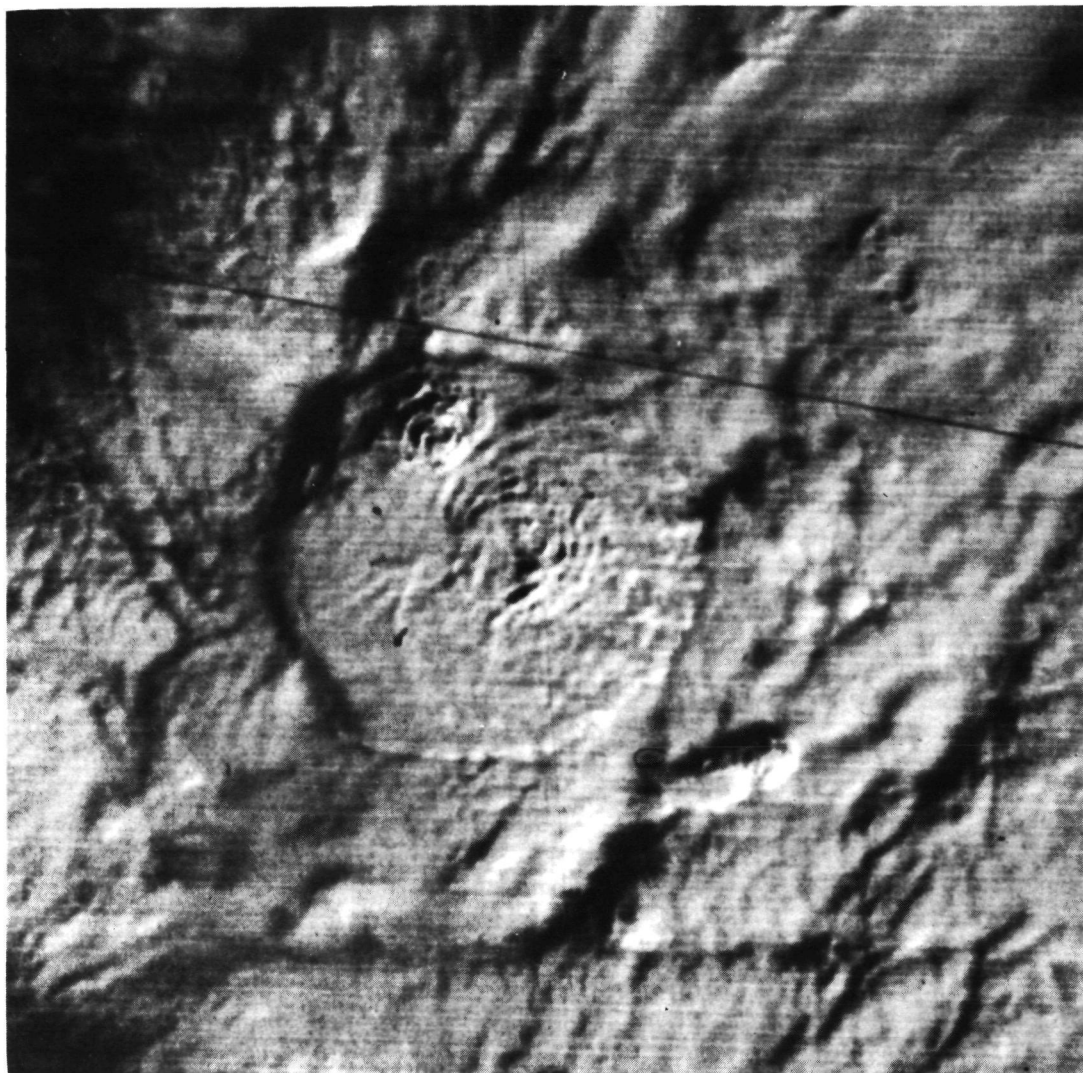


Figure 2.5. DMSF visual photograph of Typhoon Kit taken at 2230Z, January 4, 1972.

### 3. THEORIES OF WAVE GENERATION AND GROWTH

#### 3.1 Wave Generation

The concentric orientation of the waves suggests generation at a point source. This point source would be located at the focus of the waves. As was mentioned in section 2.0, the focus of the waves generally coincides with the center of the most intense convection. In the mid-latitude storms, this is marked by an overshooting dome penetrating deep into the stratosphere. In the tropics, this region is also characterized by deep convective penetration. Here, however this may be associated with either the eye wall of a tropical storm (Figs. 2.3-2.4), or the overshooting dome of an individual cell (Fig. 2.5). In all cases, however, it appears that convection penetrating through the tropopause is the key to generating the waves.

Assuming this, the problem now is to determine what facet of this deep convection causes the waves. One guess may be that the waves are similar to the ripples caused when a pebble is dropped into a calm pond. The rapid penetration of the dome through the tropopause is analogous to the pebble's penetration of the pond's surface. In such a case, the wavelength would be expected to be similar in scale to the diameter of the penetrating body. The generating mechanism, however, would only be present during the initial penetration. Once the dome had reached a quasi-steady state (vertical and horizontal extent remain constant), this means of wave generation would cease. Therefore, some type of instability would have to exist in order to sustain wave activity after the dome had reached a quasi-steady state. The Nebraska case as well as the tropical storm cases indicate continued wave generation even though the penetrative convection appears to be

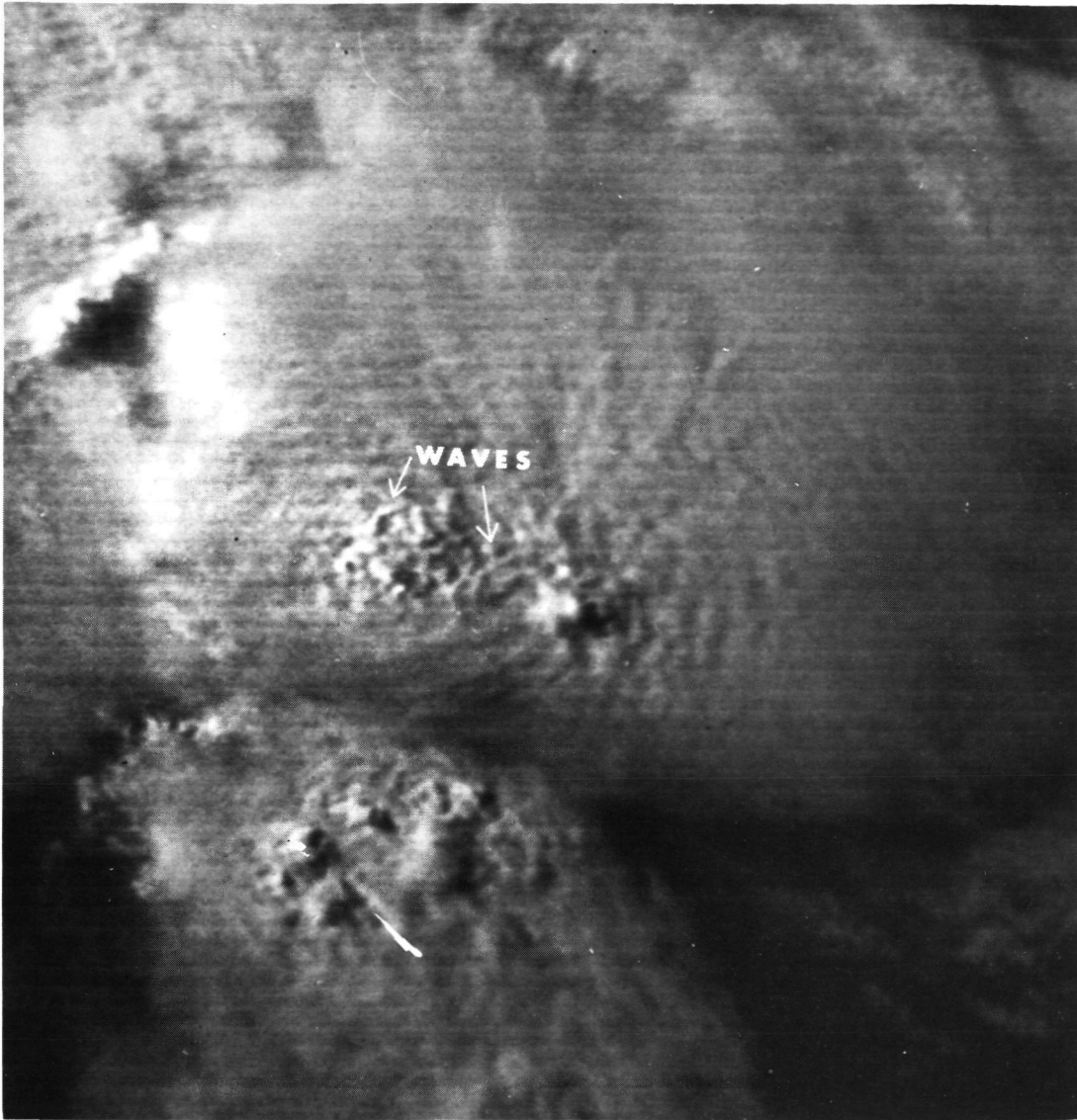


Figure 3.1. SMS-2 visual photograph taken over Nebraska at 0102Z, June 19, 1975.

Figures 2.5 and 3.1 exhibit waves that appear to have been generated by this mechanism.

Another possible means by which the waves could be generated would be by the periodic collapse and re-growth of the dome itself. This periodic dome growth could continually set up waves by generating wake

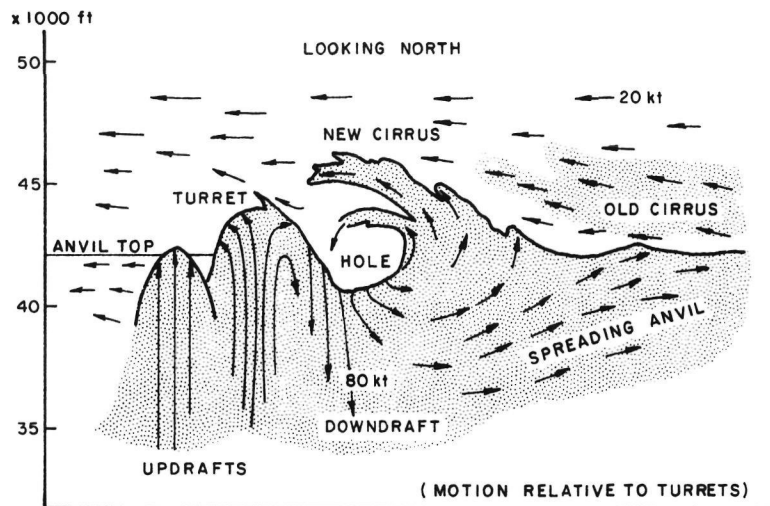


Figure 3.2. Model for parcel motions caused by a collapsing turret, (From Fujita, 1974).

cirrus similar to the "turret eater" described by Fujita (1974) (see Fig. 3.2). This model can also be described by the pebble in the pond concept, except that repeated tropopause penetration continues to generate waves. Further wave instability is not necessary in this model. One drawback, however, is that the concentric nature of the waves requires the periodic collapse and growth of a single dome in roughly the same place. There is no evidence of such stationary oscillating domes presented by Fujita (1974) or Shenk (1974). Even more obscure is the means by which such a regularly periodic dome oscillation could be generated and sustained.

The last proposed mechanism for wave generation is by quasi-steady state dome. A diagram of the particle motions within such a dome is given in Figure 3.3. Notice that this model is very similar to that proposed by Roach (1967) (see Fig. 1.1), except that it includes a warm trench along the dome perimeter. Roach (1967) did observe such a

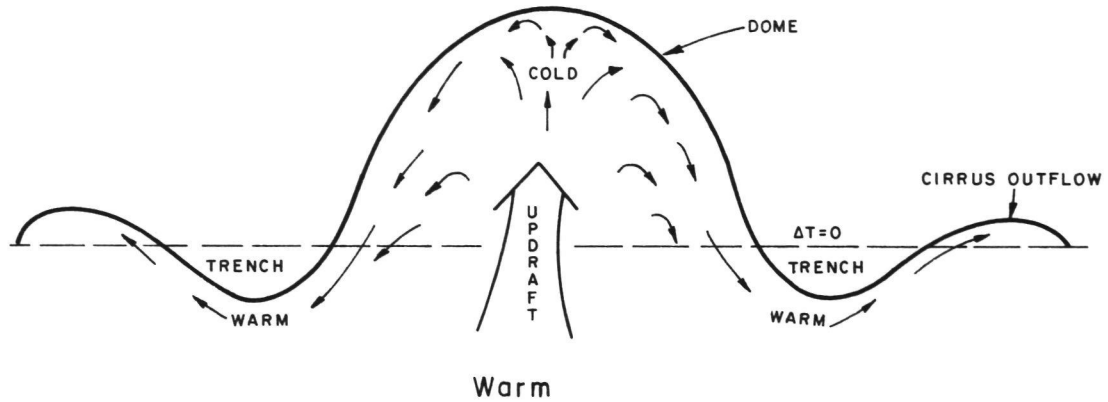


Figure 3.3. Alternate model for motions within a quasi-steady state dome.

trench around a quasi-steady state dome. However, he chose not to include it in his model diagram.

The creation of this trench is most simply explained by the "parcel method." A parcel of air located near the overshooting dome top (Fig. 3.3) will be colder than its environment. This negative buoyancy will cause a downward acceleration of the parcel. As it moves downward, it will also accelerate horizontally outward from the dome. A local high pressure created by the cold overshooting dome causes this acceleration. Figure 3.4 shows this type of motion on a single turret observed by Fujita (1974).

Once the parcel sinks adiabatically below the level of neutral buoyancy, it becomes warmer than its environment. Thus, this downward "overshooting" along with the horizontal parcel motion causes the creation of the warm trench. The mechanism responsible for the

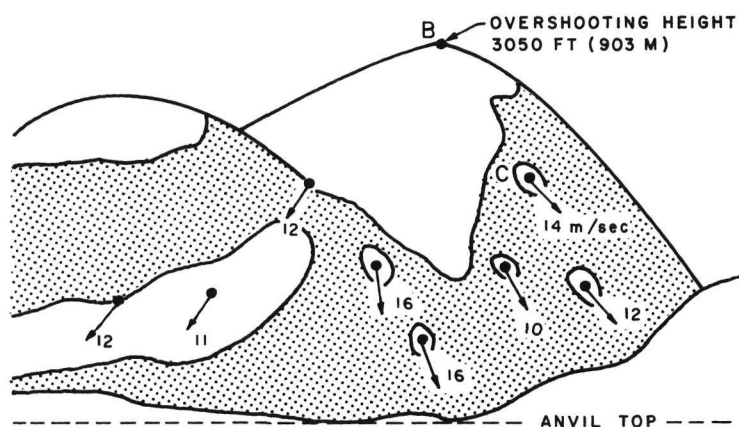


Figure 3.4. Observed cloud particle motions on an overshooting turret, (From Fujita, 1974).

formation of the warm trench would also be responsible for the generation of the waves further out from the dome. In fact, the warm trench may be viewed as merely a section of such a wave.

By the preceding description, the phase speed of the trench (relative to the dome) is always zero. The phase speed of the waves further out, however, does not appear to be zero (see case studies). Again, further wave instability is not required in this model.

Of the three generating mechanisms just described, the first appears to be the most reasonable. As will be shown in the case studies, shearing instability does appear to exist for waves in the cirrus outflow region of the storm. Thus, wave motion will persist, even after the dome becomes quasi-steady state.

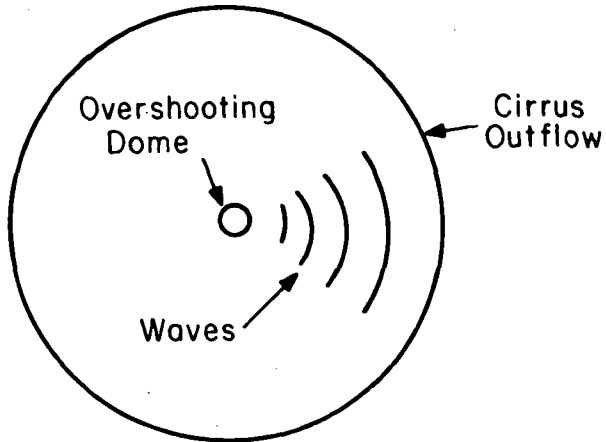


Figure 3.5. Diagram of typical concentric wave pattern.

Model. Before describing the details of the model, let us examine the characteristics of the observed phenomenon. Figure 3.5 shows the features observed in visual satellite photographs. There are two important features to be considered in Figure 3.5. First, notice that the wavelength changes farther out from the dome. To simplify the model we will assume a mean wavelength over a given  $\Delta x$ , where  $\Delta x$  is measured along a specified radial emanating from the center of the dome. Secondly, if the cirrus outflow is diverging in two dimensions, then the horizontal speed of the outflow, measured along a given radial, will be inversely proportional to the distance from the dome center. To simplify this, we will assume a mean outflow rate over  $\Delta x$ . Since we are dealing with cirrus outflow resulting from intense convection, we will assume the cirrus cloud top to be at the tropopause. Figure 3.6 contains the vertical profiles for  $\theta$ ,  $T$ ,  $\rho$ , and  $u$  for the model. Notice the two-dimensional flow in the  $xz$  plane is assumed.

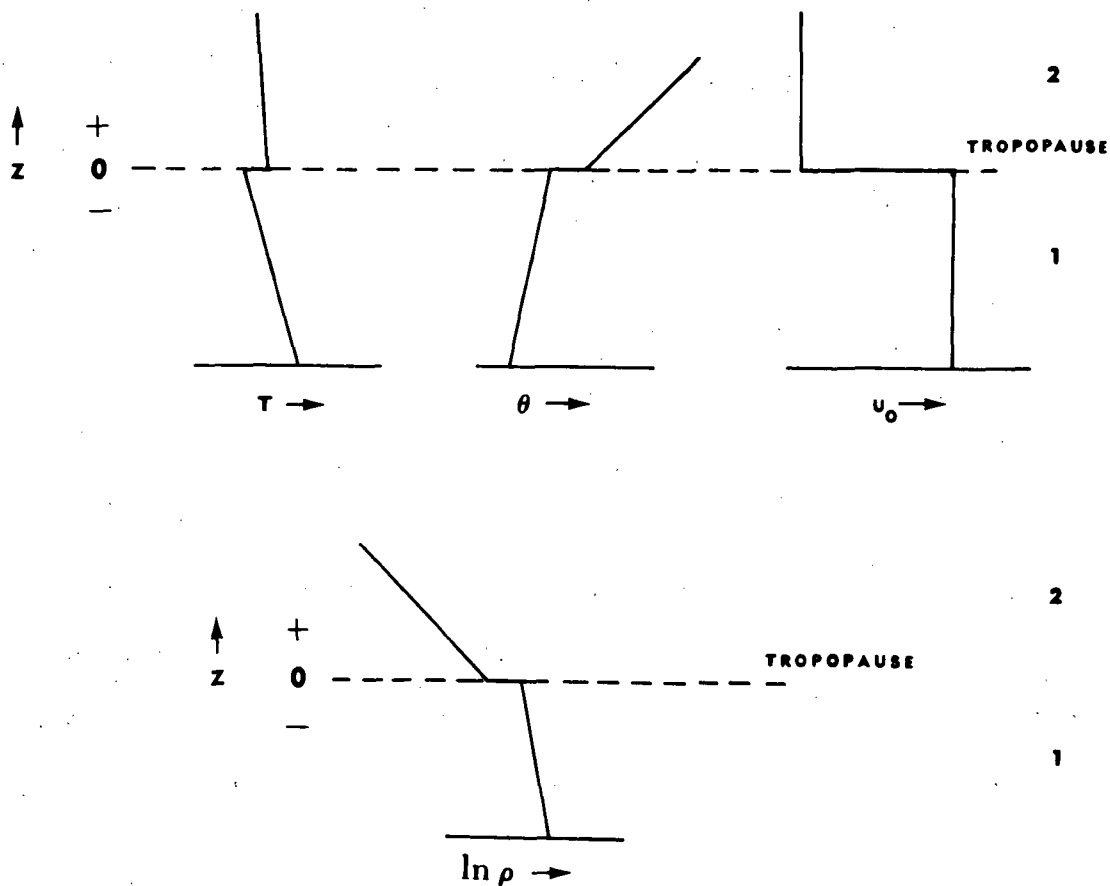


Figure 3.6. Vertical profiles of  $T$ ,  $\theta$ ,  $u_0$ , and  $\rho$  for stability model.

Layer 1 is the layer of cirrus outflow. It is located immediately below the tropopause. Layer 2 is the layer immediately above the cirrus outflow and the tropopause.

The following additional assumptions will be applied to (3.5) through (3.9).

1.  $v_0 = 0$ , and  $v = 0$ . This is a result of the earlier assumption that all the motion takes place in the  $xz$  plane. This eliminates (3.6) from the basic set of equations.
2. The tropopause is horizontal for undisturbed motion and  $z = 0$  describes the height of the tropopause. This implies

that there are no significant motions resulting from a slope in the tropopause.

3. The top layer is unbounded. This imposes a boundary condition at  $z = \infty$  which is discussed later.
4. The bottom layer is not infinitely deep but there are no effects from the lower boundary. Haurwitz (1941) described this assumption and showed that if the depth of the lower layer is greater than  $.4\lambda$ , less than 1% error is introduced by this assumption.
5.  $w_o = 0$ . This means that the mean vertical velocity relative to the tropopause is zero.
6.  $\frac{\partial p_o}{\partial x} = 0, \frac{\partial p_o}{\partial t} = 0$ . Since  $p_o$  is the average pressure on a horizontal surface, the first of these statements follows by definition. The second merely implies that the pressure at a given level does not change with respect to time.
7.  $\frac{\partial \rho_o}{\partial x} = 0, \frac{\partial \rho_o}{\partial t} = 0$ . Again, the first statement is true by definition. The second states that local changes in  $\rho_o$  with respect to time are negligible.
8.  $\frac{\partial u_o}{\partial x} = 0, \frac{\partial u_o}{\partial t} = 0$ . Again, the first statement results from the chosen method of averaging. The second implies that the average motion at any level does not change with respect to time.
9.  $\frac{\partial u_o}{\partial z} = 0$  within each layer. This has already been described by the selected vertical profile for  $u_o$  in Figure 3.6.
10. The effects from the earth's rotation are negligible ( $f = 0$ ).

Using these assumptions, (3.5) through (3.9) are rewritten as:

$$\rho_o \left( \frac{\partial u}{\partial t} + u_o \frac{\partial u}{\partial x} \right) + \frac{\partial p}{\partial x} = 0 \quad (3.10)$$

$$\rho_o \left( \frac{\partial w}{\partial t} + u_o \frac{\partial w}{\partial x} \right) + \frac{\partial p}{\partial z} + \rho g = 0 \quad (3.11)$$

$$\frac{\partial \rho}{\partial t} + u_o \frac{\partial \rho}{\partial x} + w \frac{\partial \rho_o}{\partial z} + \rho_o \frac{\partial u}{\partial x} + \rho_o \frac{\partial w}{\partial z} = 0 \quad (3.12)$$

$$\frac{\partial p}{\partial t} + u_o \frac{\partial p}{\partial x} + w \frac{\partial p_o}{\partial z} = \gamma RT \left( \frac{\partial \rho}{\partial t} + u_o \frac{\partial \rho}{\partial x} + w \frac{\partial \rho_o}{\partial z} \right) \quad (3.13)$$

Rewriting (3.12):

$$\frac{\partial \rho}{\partial t} + u_o \frac{\partial \rho}{\partial x} + w \frac{\partial \rho_o}{\partial z} = -\rho_o \frac{\partial u}{\partial x} - \rho_o \frac{\partial w}{\partial z} \quad (3.14)$$

Assume hydrostatic atmosphere:

$$\frac{\partial p_o}{\partial z} = -\rho_o g \quad (3.15)$$

Substituting (3.14) and (3.15) into (3.13):

$$\frac{\partial p}{\partial t} + u_o \frac{\partial p}{\partial x} - \rho_o g w = -\gamma RT \left( \rho_o \frac{\partial u}{\partial x} + \rho_o \frac{\partial w}{\partial z} \right) \quad (3.16)$$

Define operator  $\frac{D}{Dt}$  as:

$$\frac{D}{Dt} = \frac{\partial}{\partial t} + u_o \frac{\partial}{\partial x} \quad (3.17)$$

Since  $w_o = 0$  and  $v_o = 0$ :

$$\left( \frac{d}{dt} \right)_o = \frac{\partial}{\partial t} + u_o \frac{\partial}{\partial x} = \frac{D}{Dt}$$

Rewriting (3.11) using (3.17):

$$\frac{Dw}{Dt} + \frac{1}{\rho_o} \frac{\partial p}{\partial z} + \frac{\rho}{\rho_o} g = 0 \quad (3.18)$$

Taking  $\frac{D}{Dt}$  of equation (3.18):

$$\frac{D^2 w}{Dt^2} + \frac{1}{\rho_0} \frac{D}{Dt} \left( \frac{\partial p}{\partial z} \right) + \frac{g}{\rho_0} \frac{D\rho}{Dt} = 0 \quad (3.19)$$

Rewriting (3.13) using (3.15) and (3.17):

$$\frac{g}{\rho_0} \frac{D\rho}{Dt} = \frac{g}{\rho_0 \gamma RT} \left( \frac{Dp}{Dt} \right) - \frac{g^2}{\gamma RT} (w) - \frac{g}{\rho_0} \frac{\partial \rho_0}{\partial z} w \quad (3.20)$$

Define:

$$N^2 = -g \left( \frac{g}{\gamma RT} + \frac{1}{\rho_0} \frac{\partial \rho_0}{\partial z} \right) \quad (3.21)$$

Gossard and Hooke show that  $N^2$  is actually the Brunt-Vaisala frequency squared. Also, by use of the first law of thermodynamics for adiabatic motion and the equation of state, it can be shown that:

$$N^2 = \frac{g}{\theta} \frac{d\theta}{dz} \quad (3.22)$$

Substitute (3.21) into (3.20):

$$\frac{g}{\rho_0} \frac{D\rho}{Dt} = \frac{g}{\rho_0} \frac{1}{\gamma RT} \frac{Dp}{Dt} + N^2 w \quad (3.23)$$

Substitute (3.23) into (3.19):

$$\frac{D^2 w}{Dt^2} + \frac{1}{\rho_0} \frac{D}{Dt} \left( \frac{\partial p}{\partial z} \right) + \frac{g}{\rho_0} \frac{1}{\gamma RT} \frac{Dp}{Dt} + N^2 w = 0$$

or:

$$\left( \frac{D^2}{Dt^2} + N^2 \right) w + \frac{1}{\rho_0} \frac{D}{Dt} \left[ \left( \frac{\partial}{\partial z} + \frac{g}{\gamma RT} \right) p \right] = 0 \quad (3.24)$$

Employing the techniques of Gossard and Hooke (1975), define the following parameters:

$$U \equiv \left( \frac{\rho_o}{\rho_s} \right)^{1/2} u \quad (3.25)$$

$$W \equiv \left( \frac{\rho_o}{\rho_s} \right)^{1/2} w \quad (3.26)$$

$$P \equiv \left( \frac{\rho_o}{\rho_s} \right)^{-1/2} p \quad (3.27)$$

where:

$\rho_s$  = density at some reference level

$$\rho_o = e^{-\delta z} \rho_s$$

$\delta$  = some constant

These substitutions are a direct result of the density profile illustrated in Figure 3.9. That is,  $\rho_o$  varies exponentially with respect to height. (See section 6.0 for further discussion on the errors associated with this assumption.) This transformation is made to maintain constant coefficients in our equations while still allowing compressibility.

Using (3.25), (3.26), and (3.27), we will now develop a new set of basic equations based on (3.10), (3.16), and (3.24). First, substitute (3.24) and (3.27) into (3.10):

$$\rho_o \left( \frac{\rho_s^{1/2}}{\rho_o^{1/2}} \right) \left( \frac{DU}{Dt} \right) + \frac{\rho_o^{1/2}}{\rho_s^{1/2}} \left( \frac{\partial P}{\partial x} \right) = 0$$

or:

$$\frac{DU}{Dt} + \frac{1}{\rho_s} \frac{\partial P}{\partial x} = 0 \quad (3.28)$$

Substitute (3.26) and (3.27) into (3.24):

$$\left( \frac{D^2}{Dt^2} + N^2 \right) W + \frac{1}{\rho_s} \frac{D}{Dt} \left[ \left( \frac{1}{2\rho_o} \frac{\partial \rho_o}{\partial z} + \frac{g}{\gamma RT} + \frac{\partial}{\partial z} \right) P \right] = 0 \quad (3.29)$$

Again, following Gossard and Hooke (1975), define:

$$\Gamma = \frac{1}{2\rho_0} \frac{\partial \rho_0}{\partial z} + \frac{g}{\gamma RT} = \frac{1}{2} \left( \frac{g}{\gamma RT} - \frac{N^2}{g} \right) \quad (3.30)$$

Substitute (3.30) into (3.29):

$$\left( \frac{D^2}{Dt^2} + N^2 \right) W + \frac{1}{\rho_s} \frac{D}{Dt} \left[ \left( \Gamma + \frac{\partial}{\partial z} \right) P \right] = 0 \quad (3.31)$$

Substitute (3.25), (3.26), and (3.27) into (3.16):

$$\frac{1}{\rho_s \gamma RT} \frac{DP}{Dt} + \frac{\partial U}{\partial x} + \left( \frac{\partial}{\partial z} - \frac{g}{\gamma RT} - \frac{1}{2\rho_0} \frac{\partial \rho_0}{\partial z} \right) W = 0 \quad (3.32)$$

Substitute (3.30) into (3.32):

$$\frac{1}{\rho_s \gamma RT} \frac{DP}{Dt} + \frac{\partial U}{\partial x} + \left( \frac{\partial}{\partial z} - \Gamma \right) W = 0 \quad (3.33)$$

For convenience, the three basic equations just discussed are rewritten below:

$$\frac{DU}{Dt} + \frac{1}{\rho_s} \frac{\partial p}{\partial x} = 0 \quad (3.28)$$

$$\frac{1}{\rho_s} \left( \frac{1}{\gamma RT} \right) \frac{DP}{Dt} + \frac{\partial U}{\partial x} + \left( \frac{\partial}{\partial z} - \Gamma \right) W = 0 \quad (3.33)$$

$$\left( \frac{D^2}{Dt^2} + N^2 \right) W + \frac{1}{\rho_s} \frac{D}{Dt} \left[ \left( \Gamma + \frac{\partial}{\partial z} \right) P \right] = 0 \quad (3.31)$$

Utilizing these three equations, we will now investigate the possible forms of solutions for U, W, and P for each layer of the model. A subscript of "1" will denote the lower layer and a subscript of "2" the upper layer.

Let us first investigate solutions for the upper layer. Assume solutions of the form:

$$U_2 = A_2 e^{-\beta_2 z} \cos [\mu(x-ct)] \quad (3.34)$$

$$W_2 = C_2' e^{-\beta_2 z} \sin [\mu(x-ct)] \quad (3.35)$$

$$P_2 = D_2 e^{-\beta_2 z} \cos [\mu(x-ct)] \quad (3.36)$$

To limit the possible solutions, two boundary conditions were imposed.

First, at  $x = 0$  and  $t = 0$ , let  $W_2 = 0$ . Second, at  $z = \infty$ , let  $w_2 = 0$ .

A solution set for the lower layer may be obtained in a similar fashion resulting in:

$$U_1 = A_1 e^{\beta_1 z} \cos [\mu(x-ct)] \quad (3.37)$$

$$W_1 = C_1' e^{\beta_1 z} \sin [\mu(x-ct)] \quad (3.38)$$

$$P_1 = D_1 e^{\beta_1 z} \cos [\mu(x-ct)] \quad (3.39)$$

The second boundary condition does not necessarily apply in the lower layer since it is not infinitely deep. Let us look at  $w_1$  as a function of  $z$  for both positive and negative values of  $\beta_1$ . From (3.26) and (3.37):

$$w_1 = C_1' e^{(\beta_1 + \frac{1}{2} \delta_1) z} \sin [\mu(x-ct)]$$

Notice that an amplification in  $w_1$  as we move downward from  $z = 0$  (tropopause) will occur only if  $\beta_1 < -\frac{1}{2} \delta_1$ . This form of amplification in the vertical of the lower layer should be minimized as much as possible. Otherwise, if our wave is effecting a significant  $\Delta z$  in the lower layer, large amplitude errors in the vertical will be introduced. Nevertheless, the condition  $\beta_1 > -\frac{1}{2} \delta_1$ , does not require  $\beta_1 > 0$  for the lower layer. That is, for certain  $\beta_1 < 0$ , amplification of  $w_1$  will still not occur as we move downward from  $z = 0$ . Thus,  $\beta_1$  can be positive

or negative so long as the magnitude of a given negative  $\beta_1$  is not extremely large.

Now, directing our attention to the upper layer only, substitute (3.34), (3.35), and (3.36) into (3.28), (3.33), and (3.31):

$$A_2 (c-u_{o2}) - \frac{1}{\rho_{s2}} D_2 = 0 \quad (3.40)$$

$$\frac{1}{\rho_s} \frac{1}{\gamma R T_2} (c-u_{o2}) D_2 - A_2 - C'_2 \left( \frac{\beta_2 + \Gamma_2}{\mu} \right) = 0 \quad (3.41)$$

$$\left[ \mu^2 (c-u_{o2})^2 - N_2^2 \right] C'_2 - \frac{\mu}{\rho_{s2}} (\Gamma_2 - \beta_2) (c-u_{o2}) D_2 = 0 \quad (3.42)$$

Solve (3.40) for  $D_2$  and substitute into (3.41):

$$\left[ \frac{1}{\gamma R T_2} (c-u_{o2})^2 \right] A_2 - A_2 - C'_2 \left( \frac{\beta_2 + \Gamma_2}{\mu} \right) = 0 \quad (3.43)$$

or:

$$\chi_2 A_2 - C'_2 \left( \frac{\beta_2 + \Gamma_2}{\mu} \right) = 0 \quad (3.44)$$

where:

$$\chi_2 = \frac{1}{\gamma R T_2} (c-u_{o2})^2 - 1 \quad (3.45)$$

Solve (3.44) for  $A_2$  and substitute into (3.40):

$$\frac{C'_2}{\chi_2} \left( \frac{\beta_2 + \Gamma_2}{\mu} \right) (c-u_{o2}) - \frac{1}{\rho_{s2}} D_2 = 0 \quad (3.46)$$

Solve (3.46) for  $D_2$  and substitute into (3.42):

$$\mu^2 (c-u_{o2})^2 - N_2^2 - \frac{\Gamma_2^2 - \beta_2^2}{\chi_2} (c-u_{o2})^2 = 0 \quad (3.47)$$

Solve (3.47) for  $\beta_2$ :

$$\beta_2 = \left\{ \Gamma_2^2 + \chi_2 \left[ \frac{N_2^2}{(c-u_{02})^2} - \mu^2 \right] \right\}^{1/2} \quad (3.48)$$

where the real component of  $\beta_2$  is always greater than zero.

Using (3.44) and (3.46) to substitute for  $A_2$  and  $D_2$  in terms of  $C_2'$  in (3.34) and (3.36), the solution set for the upper layer may now be written as:

$$U_2 = C_2' \left( \frac{\beta_2 + \Gamma_2}{\mu \chi_2} \right) e^{-\beta_2 z} \cos [\mu(x-ct)] \quad (3.49)$$

$$W_2 = C_2' e^{-\beta_2 z} \sin [\mu(x-ct)] \quad (3.50)$$

$$P_2 = C_2' \rho_{s2}(c-u_{02}) \left( \frac{\beta_2 + \Gamma_2}{\mu \chi_2} \right) e^{-\beta_2 z} \cos [\mu(x-ct)] \quad (3.51)$$

Now performing a similar analysis of the lower layer, substitute (3.37), (3.38), and (3.39) into (3.28), (3.33), and (3.31):

$$(c-u_{01}) A_1 - \frac{1}{\rho_{s1}} D_1 = 0 \quad (3.52)$$

$$\frac{1}{\rho_{s1}} \left( \frac{1}{\gamma R T_1} \right) (c-u_{01}) D_1 - A_1 + C_1' \left( \frac{\beta_1 - \Gamma_1}{\mu} \right) = 0 \quad (3.53)$$

$$[\mu^2 (c-u_{01})^2 - N_1^2] C_1' - \frac{\mu}{\rho_{s1}} (\beta_1 + \Gamma_1) (c-u_{01}) D_1 = 0 \quad (3.54)$$

Solve (3.52) for  $D_1$  and substitute into (3.53):

$$\frac{1}{\gamma R T_1} (c-u_{01})^2 A_1 - A_1 + C_1' \left( \frac{\beta_1 - \Gamma_1}{\mu} \right) = 0 \quad (3.55)$$

or:

$$\chi_1 A_1 + C_1' \left( \frac{\beta_1 - \Gamma_1}{\mu} \right) = 0 \quad (3.56)$$

where:

$$\chi_1 = \frac{1}{\gamma R T_1} (c-u_{o1})^2 - 1 \quad (3.57)$$

Solve (3.56) for  $A_1$  and substitute into (3.52):

$$\left( \frac{\beta_1 - \Gamma_1}{\chi_1 \mu} \right) (c-u_{o1}) C_1' + \frac{1}{\rho s_1} D_1 = 0 \quad (3.58)$$

Solve (3.58) for  $D_1$  and substitute into (3.54):

$$\mu^2 (c-u_{o1})^2 - N_1^2 - \frac{(\Gamma_1^2 - \beta_1^2)}{\chi_1} (c-u_{o1})^2 = 0 \quad (3.59)$$

Solve (3.59) for  $\beta_1$ :

$$\beta_1 = \pm \left\{ \Gamma_1^2 + \chi_1 \left[ \frac{N^2}{(c-u_{o1})^2} - \mu^2 \right] \right\}^{1/2} \quad (3.60)$$

Using (3.56) and (3.58) to substitute for  $A_1$  and  $D_1$  in terms of  $C_1'$  in (3.37) and (3.39), the solution set for the lower layer may now be written as:

$$U_1 = C_1' \left( \frac{\Gamma_1 - \beta_1}{\mu \chi_1} \right) e^{\beta_1 z} \cos [\mu(x-ct)] \quad (3.61)$$

$$W_1 = C_1' e^{\beta_1 z} \sin [\mu(x-ct)] \quad (3.62)$$

$$P_1 = C_1' \rho s_1 (c-u_{o1}) \left( \frac{\Gamma_1 - \beta_1}{\mu \chi_1} \right) e^{\beta_1 z} \cos [\mu(x-ct)] \quad (3.63)$$

Utilizing the boundary condition for a surface of discontinuity described by Haurwitz (1941), the following equations for each layer are obtained:

$$\begin{aligned} & \frac{\partial(P_1 - P_2)}{\partial t} + u_{o1} \frac{\partial(P_1 - P_2)}{\partial x} + u_1 \frac{\partial(\rho_{o1} + \rho_{o2})}{\partial x} + v_{o1} \frac{\partial(P_1 - P_2)}{\partial y} \\ & + v_1 \frac{\partial(\rho_{o1} - \rho_{o2})}{\partial y} + w_{o1} \frac{\partial(P_1 - P_2)}{\partial z} + W_1 \frac{\partial(\rho_{o1} - \rho_{o2})}{\partial z} = 0 \end{aligned} \quad (3.64)$$

$$\begin{aligned} \frac{\partial(P_1 - P_2)}{\partial t} + u_{o_2} \frac{\partial(P_1 - P_2)}{\partial x} + u_2 \frac{\partial(p_{o_1} - p_{o_2})}{\partial x} + v_{o_2} \frac{\partial(P_1 - P_2)}{\partial y} \\ + v_2 \frac{\partial(p_{o_1} + p_{o_2})}{\partial y} + w_{o_2} \frac{\partial(P_1 - P_2)}{\partial z} + w_2 \frac{\partial(p_{o_1} - p_{o_2})}{\partial z} = 0 \end{aligned} \quad (3.65)$$

Employing the assumptions discussed earlier, (3.64) and (3.65) reduce to:

$$\frac{\partial(P_1 - P_2)}{\partial t} + u_{o_1} \frac{\partial(P_1 - P_2)}{\partial x} + w_1 \frac{\partial(p_{o_1} - p_{o_2})}{\partial z} = 0 \quad (3.66)$$

$$\frac{\partial(P_1 - P_2)}{\partial t} + u_{o_2} \frac{\partial(P_1 - P_2)}{\partial x} + w_2 \frac{\partial(p_{o_1} - p_{o_2})}{\partial z} = 0 \quad (3.67)$$

From (3.51) and (3.63):

$$P_1 - P_2 = \sigma \cos [\mu(x-ct)] \quad (3.68)$$

where:

$$\sigma = C_1' \rho_{s_1} (c - u_{o_1}) \left( \frac{\Gamma_1 - \beta_1}{\mu \chi_1} \right) e^{\beta_1 z} - C_2' \rho_{s_2} (c - u_{o_2}) \left( \frac{\beta_2 + \Gamma_2}{\mu \chi_2} \right) e^{-\beta_2 z} \quad (3.69)$$

From the hydrostatic equation, (3.15):

$$p_{o_1} - p_{o_2} = gz (\rho_{o_1} - \rho_{o_2}) \quad (3.70)$$

We will now choose  $\rho_{s_1}$  and  $\rho_{s_2}$  such that:

$$\rho_{s_1} = \rho_{o_1} \text{ measured at the upper surface of the tropopause} \quad (3.71)$$

$$\rho_{s_2} = \rho_{o_2} \text{ measured at the lower surface of the tropopause} \quad (3.72)$$

Substitute (3.71) and (3.72) into (3.70):

$$p_{o_1} - p_{o_2} = -gz (\rho_{s_1} - \rho_{s_2}) \quad (3.73)$$

Substitute (3.68) and (3.73) into (3.66) and (3.67):

$$(c - u_{o_1}) \sigma - C_1' e^{\beta_1 z} g (\rho_{s_1} - \rho_{s_2}) = 0 \quad (3.74)$$

$$(c-u_{o_2})\sigma - C_2' e^{-\beta_2 z} g(\rho_{s_1} - \rho_{s_2}) = 0 \quad (3.75)$$

Substitute (3.69) back into (3.74) and (3.75) and rearrange terms:

$$\frac{C_1' e^{\beta_1 z}}{C_2' e^{-\beta_2 z}} = \frac{(c-u_{o_1})(c-u_{o_2})\rho_{s_2} \left(\frac{\beta_2 + \Gamma_2}{\chi_2}\right)}{(c-u_{o_1})^2 \rho_{s_1} \left(\frac{\Gamma_1 - \beta_1}{\chi_1}\right) - g(\rho_{s_1} - \rho_{s_2})} \quad (3.76)$$

$$\frac{C_1' e^{\beta_1 z}}{C_2' e^{-\beta_2 z}} = \frac{(c-u_{o_2})^2 \rho_{s_2} \left(\frac{\beta_2 + \Gamma_2}{\chi_2}\right) + g(\rho_{s_1} - \rho_{s_2})}{(c-u_{o_2})(c-u_{o_1})\rho_{s_1} \left(\frac{\Gamma_1 - \beta_1}{\chi_1}\right)} \quad (3.77)$$

Equate (3.76) and (3.77):

$$\frac{(c-u_{o_1})(c-u_{o_2})\rho_{s_2} \left(\frac{\beta_2 + \Gamma_2}{\chi_2}\right)}{(c-u_{o_1})^2 \rho_{s_1} \left(\frac{\Gamma_1 - \beta_1}{\chi_1}\right) - g(\rho_{s_1} - \rho_{s_2})} = \frac{(c-u_{o_2})^2 \rho_{s_2} \left(\frac{\beta_2 + \Gamma_2}{\chi_2}\right) + g(\rho_{s_1} - \rho_{s_2})}{(c-u_{o_2})(c-u_{o_1})\rho_{s_1} \left(\frac{\Gamma_1 - \beta_1}{\chi_1}\right)} \quad (3.78)$$

or:

$$(c-u_{o_1})^2 \rho_{s_1} \left(\frac{\Gamma_1 - \beta_1}{\chi_1}\right) + (c-u_{o_2})^2 \rho_{s_2} \left(\frac{\Gamma_2 + \beta_2}{\chi_2}\right) + g(\rho_{s_1} - \rho_{s_2}) = 0 \quad (3.79)$$

Using the equation of state and Poisson's equation, we will now substitute for  $\rho_{s_1}$  and  $\rho_{s_2}$  in terms of  $\theta_1$  and  $\theta_2$  (each measured immediately below and above the tropopause respectively). First, from the equation of state:

$$\rho_{s_1} = \frac{p_{s_1}}{RT_{s_1}} \quad (3.80)$$

(Subscript  $s_1$  indicates lower surface of tropopause.)

$$\rho_{s_2} = \frac{p_{s_2}}{RT_{s_2}} \quad (3.81)$$

(Subscript  $s_2$  indicates upper surface of tropopause.)

Secondly, from Poisson's equation:

$$T_{s_1} = \theta_{s_1} \left( \frac{p_{s_1}}{1000} \right)^{R/C_p} \quad (3.82)$$

$$T_{s_2} = \theta_{s_2} \left( \frac{p_{s_2}}{1000} \right)^{R/C_p} \quad (3.83)$$

Along the tropopause  $p_{s_1} = p_{s_2}$ :

$$\left( \frac{p_{s_2}}{1000} \right)^{R/C_p} = \left( \frac{p_{s_1}}{1000} \right)^{R/C_p} = K \quad (3.84)$$

where:

$K = \text{constant}$

Substitute (3.82), (3.83), and (3.84) into (3.80) and (3.81):

$$\rho_{s_1} = \left( \frac{p_{s_1}}{RK} \right) \frac{1}{\theta_{s_1}} \quad (3.85)$$

$$\rho_{s_2} = \left( \frac{p_{s_2}}{RK} \right) \frac{1}{\theta_{s_2}} \quad (3.86)$$

Again, since  $p_{s_1} = p_{s_2}$ :

$$\rho_{s_1} = K' \frac{1}{\theta_{s_1}} \quad (3.87)$$

$$\rho_{s_2} = K' \frac{1}{\theta_{s_2}} \quad (3.88)$$

where:

$$K' = \frac{P_{s_1}}{RK} = \frac{P_{s_2}}{RK} = \text{constant} \quad (3.89)$$

Substitute (3.87) and (3.88) into (3.79):

$$(c-u_{o_1})^2 \theta_{s_2} \left( \frac{\Gamma_1 - \beta_1}{\chi_1} \right) + (c-u_{o_2})^2 \theta_{s_1} \left( \frac{\Gamma_2 + \beta_2}{\chi_2} \right) + g (\theta_{s_2} - \theta_{s_1}) = 0 \quad (3.90)$$

We will now define a mean horizontal wind speed between the two layers:

$$\bar{u}_o = \frac{u_{o_1} + u_{o_2}}{2} \quad (3.91)$$

Align the coordinate system such that:

$$\bar{u}_o = 0$$

Therefore:

$$u_{o_2} = -u_{o_1} \quad (3.92)$$

and:

$$2u_{o_1} = \Delta u_o \quad (3.93)$$

where  $\Delta u_o$  is the difference between the mean wind speeds of each layer, measured across the tropopause. Thus, under this new coordinate system, (3.90) becomes:

$$(c-u_{o_1})^2 \theta_{s_2} \left( \frac{\Gamma_1 - \beta_1}{\chi_1} \right) + (c+u_{o_1})^2 \theta_{s_1} \frac{\Gamma_2 + \beta_2}{\chi_2} + g (\theta_{s_2} - \theta_{s_1}) = 0 \quad (3.94)$$

where:

$$\beta_2 = \left\{ \Gamma_2^2 + \chi_2 \left[ \frac{N_2^2}{(c+u_{o_1})^2} - \mu^2 \right] \right\}^{1/2} \quad (3.95)$$

$$\chi_2 = \frac{1}{\gamma RT} (c + u_{o_1})^2 - 1 \quad (3.96)$$

$$\Gamma_1 = \frac{1}{2} \left( \frac{g}{\gamma RT_1} - \frac{N_1^2}{g} \right) \quad (3.97)$$

$$\Gamma_2 = \frac{1}{2} \left( \frac{g}{\gamma RT_2} - \frac{N_2^2}{g} \right) \quad (3.98)$$

and  $\beta_1$  and  $\chi_1$  are defined by (3.60) and (3.57).

Equation (3.94) will be the basic equation used to determine wave stability. As was mentioned earlier, the real component of  $\beta_2$  is always positive. However, no such restriction was placed on  $\beta_1$ . Therefore, for a given  $u_{o_1}$  there are two possible solutions for  $c$ , (assuming a solution does exist for both  $\beta_1 > 0$  and  $\beta_1 < 0$ ). One feature, however, must be maintained, and that is,  $c$  must be a continuous function of  $u_{o_1}$ . Appendix B discusses the selection of  $\beta_1 > 0$  or  $\beta_1 < 0$ .

Wave Stability. The ultimate goal of this model is to accurately depict wave instability with respect to time. From equations (3.38) and (3.35), it can be seen that if  $c$  is purely real, no amplification will occur, and thus, the waves will be neutrally stable. If, however,  $c$  is complex, growth will occur based on the following:

Let:

$$c = c_r + c_i i$$

Since:

$$W_2, W_1 \propto \sin [\mu(x-ct)] \quad (3.99)$$

and:

$$c_r, c_i, \mu, x \text{ and } t \text{ are all real}$$

Therefore:

$$W_2, W_1 \propto \sin [(\mu x - \mu c_r t) - (\mu c_i t)i] \quad (3.100)$$

or:

$$W_2, W_1 \propto \sin (m + ni) \quad (3.101)$$

where:

$$m = \mu x - \mu c_r t \quad (3.102)$$

$$n = -\mu c_i t \quad (3.103)$$

From Kreyszig (1968):

$$\sin (m + ni) = \sin m \cosh n + i \cos m \sinh n \quad (3.104)$$

If  $C_1'$  and  $C_2'$  in (3.38) and (3.35) are assumed to be purely real, the imaginary term on the right side of (3.104) is not physically significant. Therefore, the amplification rate of  $W_2$  and  $W_1$  is  $\cosh (-\mu c_i t)$ , where  $c_i$  is the imaginary component of  $c$ . For convenience, we will define the instability amplification factor,  $\psi$ :

$$\psi = \cosh (-\mu c_i t) \quad (3.105)$$

Figure 3.7 contains traces of  $c_r$ ,  $|c_i|$ , and  $\beta_1$  versus  $\Delta u_o$ . The characteristics displayed in this example are also found in each of the case studies. Those characteristics considered most significant are:

1. In the  $c_r$  versus  $\Delta u_o$  curve,  $c_r$  is a continuous function of  $\Delta u_o$ .
2. In the  $|c_i|$  versus  $\Delta u_o$  curve,  $|c_i|$  is greater than zero only over a range of  $\Delta u_o$ . Also,  $|c_i|$  displays an additional point of neutral stability ( $|c_i| = 0$ ) within this range.

This point occurs at  $c = \frac{\Delta u_o}{2}$ .

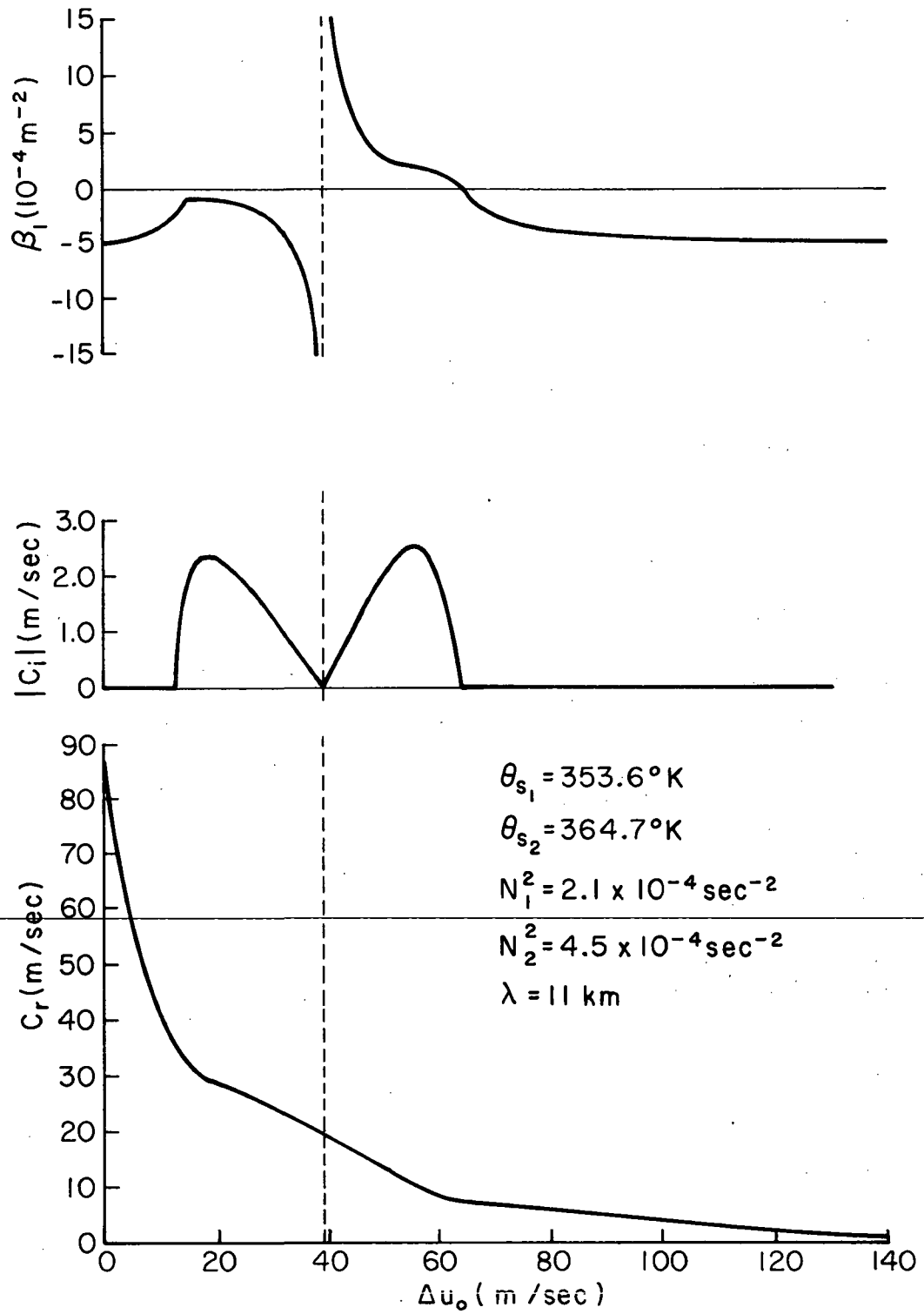


Figure 3.7. Sample curves of  $c_r$ ,  $|c_i|$ , and  $\beta_1$  versus  $\Delta u_o$ .

3. In the  $\beta_1$  versus  $\Delta u_0$  curve,  $\beta_1$  does go from a positive to a negative value. At  $c = \frac{\Delta u_0}{2}$ ,  $\beta_1 = \pm \infty$ . This is difficult to interpret physically as far as  $\beta_1$  itself is concerned. However, it does not introduce discontinuities in  $c_i$  and  $c_r$  since the coefficient of  $\beta_1$  is zero at this point.

Thus, we see that the model can be used to infer instability regimes.

This will be elaborated on further in the case studies.

#### 4. DATA ANALYSIS TECHNIQUES

##### 4.1 Mid-Latitude

The data used to analyze the mid-latitude cases (Nebraska and Kansas) is summarized in Table 4.1. Figure 4.1 shows the area of coverage for the upper air, radar, and surface observations.

Table 4.1. Mid-Latitude Data Sources

<u>Type of Data</u>	<u>Time of Observations</u>	<u>Data Source</u>
Satellite Photographs (IR and Visible)	Once every 15 to 30 min from 12Z June 18, 1975 to 12Z June 19, 1975	SMS-1 and SMS-2 photographs received at the Satellite Field Service Station (SFSS) in Kansas City, Missouri
Upper Air Soundings	12Z June 18, 1975 and 00Z June 19, 1975	Computer plotted soundings received at the Severe Local Storms Forecast Center in Kansas City, Missouri
Radar Reports and Surface Observations	Once every hour plus specials from 12Z June 18, 1975 to 12Z June 19, 1975	Teletype reports received at F. E. Warren Air Force Base, Wyoming
NMC Facsimile Maps	In accordance with NAMFAX schedule from 12Z June 17, 1975 to 12Z June 20, 1975	Facsimile products received via NAMFAX circuit GF-10201 at the Department of Atmospheric Science, Colorado State University

Scale factors for the satellite photographs were derived from map overlays such as the one shown in Figure 4.2. These overlays were added to the prints made by the SFSS in Kansas City. They were not on the original negatives. The following example illustrates two distance measurements on a blow up of this photograph.

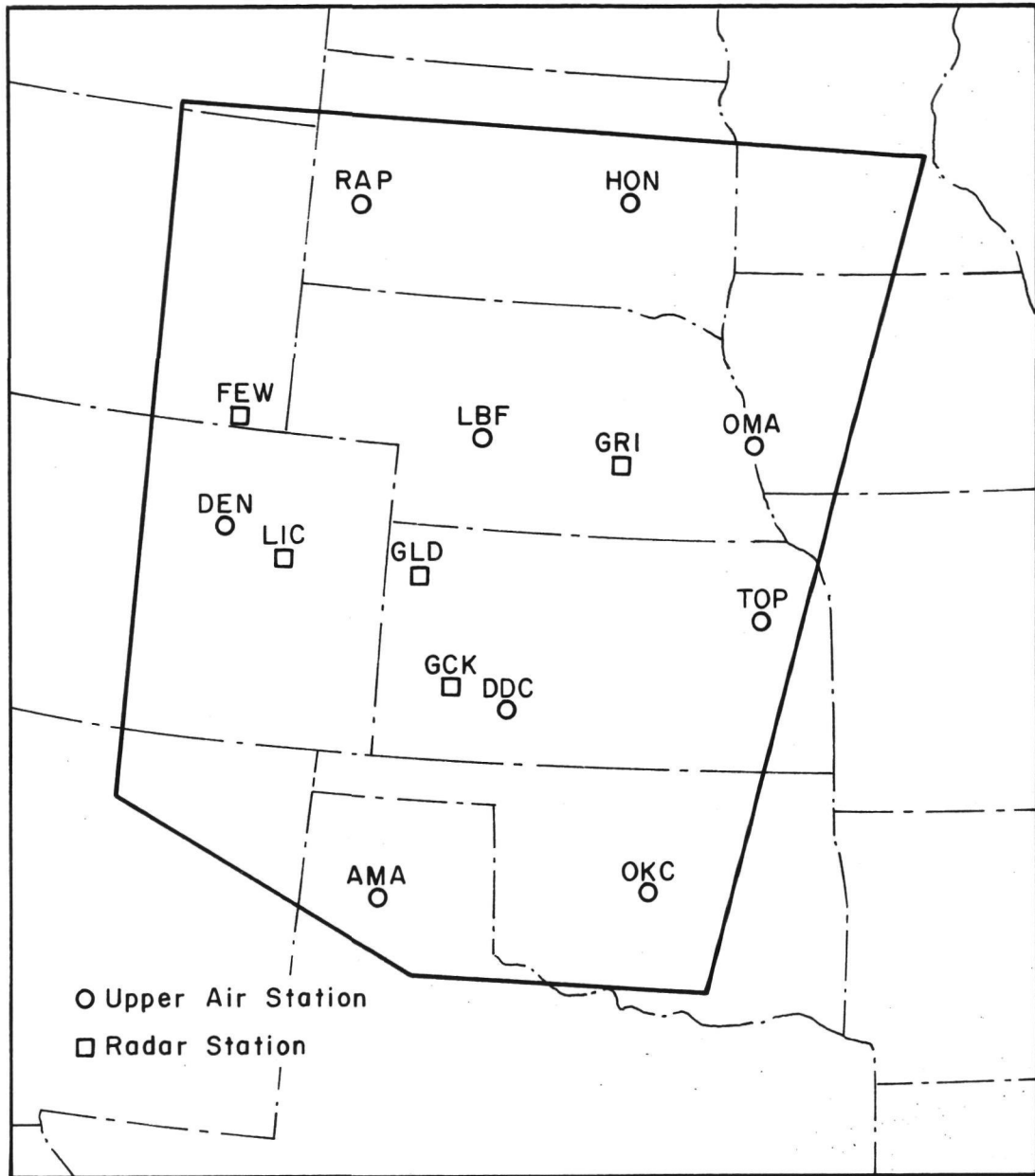


Figure 4.1. Map showing area of data coverage for the mid-latitude cases.

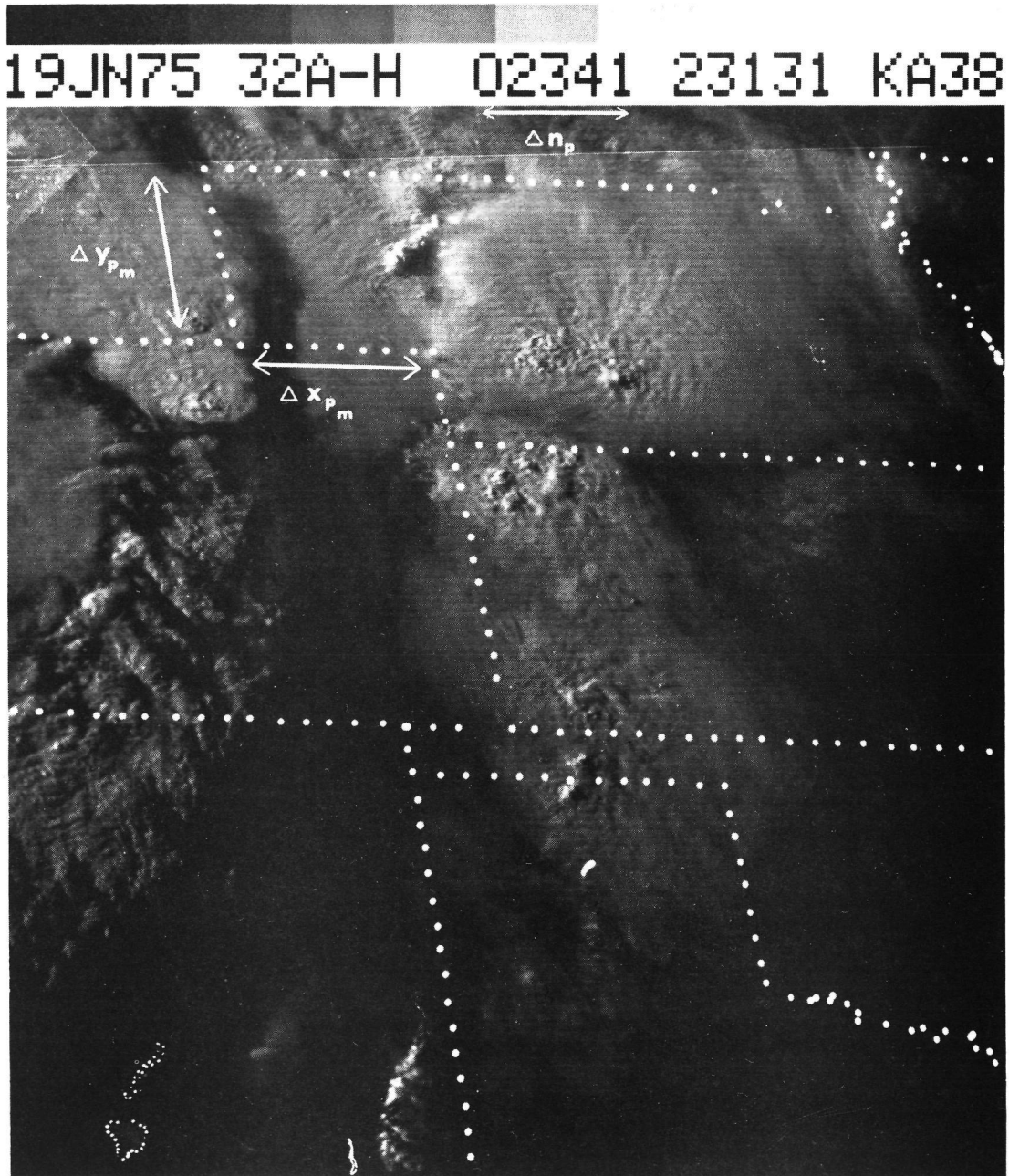


Figure 4.2. SMS-2 visual photograph with map grid, taken at 0102Z, June 19, 1975.

1. In Figure 4.2, calculate the east-west map scale factor,  $E_s$ , for the Nebraska area. To do this, measure the length of the southern border of the Nebraska panhandle on the map,  $\Delta x_{p_m}$ , and compare this to its actual length on earth,  $\Delta x_{p_a}$ :

$$\Delta x_{p_m} = 27.5 \text{ mm}$$

$$\Delta x_{p_a} = 165 \text{ km}$$

$$E_s = \frac{\Delta x_{p_m}}{\Delta x_{p_a}} = \frac{1}{6 \times 10^5}$$

2. Again in Figure 4.2, calculate the north-south map scale factor,  $N_s$ , for Nebraska by similar means, this time using the western border of the panhandle as a reference:

$$\Delta y_{p_m} = 26 \text{ mm}$$

$$\Delta y_{p_a} = 222 \text{ km}$$

$$N_s = \frac{\Delta y_{p_m}}{\Delta y_{p_a}} = \frac{1}{8.5 \times 10^6}$$

3. Measure the distance between two numbers on the legend of the original print ( $\Delta N_p$  in Fig. 4.2) and between the same two numbers on the blow-up ( $\Delta N_B$  in Fig. 4.3). Compare these distances to calculate an enlargement factor,  $F$ :

$$F = \frac{48 \text{ mm}}{22 \text{ mm}} = 2.18$$

4. Multiply  $E_s$  and  $N_s$  by  $F$  to get the corresponding scale factors for the blow-up,  $E_B$  and  $N_B$ :

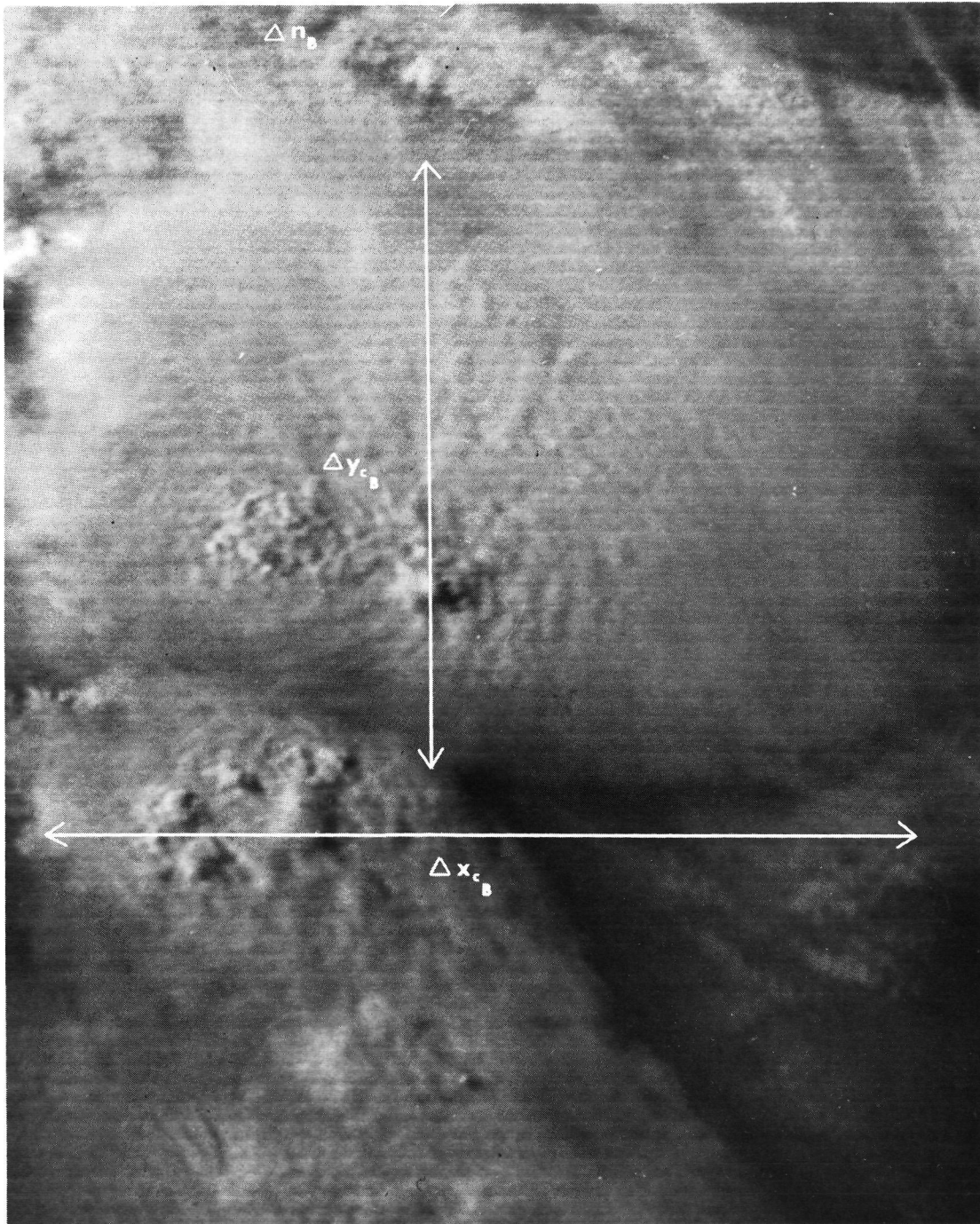


Figure 4.3. Blow up of Figure 4.2 without map grid.

$$E_B = (2.18) \times \frac{1}{6 \times 10^6} = \frac{1}{2.75 \times 10^6}$$

$$N_B = (2.18) \times \frac{1}{8.5 \times 10^6} = \frac{1}{3.9 \times 10^6}$$

5. Measure the east-west diameter of the cloud on the blow-up,

$\Delta x_{c_B}$ , and multiply it by  $\frac{1}{E_B}$  to obtain the cloud's actual east-west diameter,  $\Delta x_{c_a}$ :

$$\Delta x_{c_B} = 135 \text{ mm}$$

$$\Delta x_{c_a} = (135 \text{ mm}) \times (2.75 \times 10^6)$$

$$= 371 \text{ km}$$

6. Measure the north-south diameter of the cloud on the blow-up,

$\Delta y_{c_B}$ , and multiply it by  $\frac{1}{N_B}$  to obtain the cloud's actual north-south diameter,  $\Delta y_{c_a}$ :

$$\Delta y_{c_B} = 83 \text{ mm}$$

$$\Delta y_{c_a} = (83 \text{ mm}) \times (3.9 \times 10^6)$$

$$= 324 \text{ km}$$

The data used to calculate wave stability criteria, according to the model in section 3.2, were taken from the nearest upper air sounding (time and space) to each storm. The following is an example of how these data are incorporated into the computer program which solves equation (3.94) for  $c$  in terms of  $\Delta u_0$  and  $\lambda$ :

1. Read the temperature and pressure immediately above and below the tropopause ( $T_2$ ,  $P_2$  and  $T_1$ ,  $P_1$  in Fig. 4.4).
2. Read the temperature and pressure of the next reported level above and below the tropopause ( $T_{2_{up}}$ ,  $P_{2_{up}}$  and  $T_{1_{low}}$ ,  $P_{1_{low}}$  in Fig. 4.4).

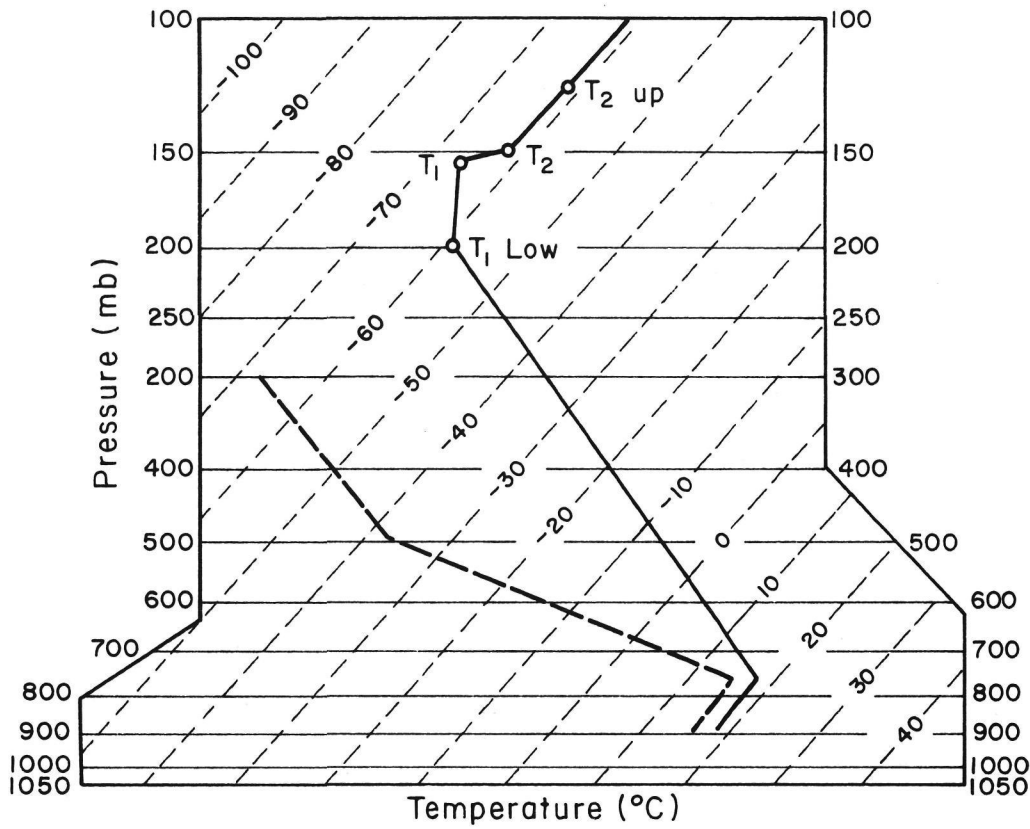


Figure 4.4. Temperature sounding from North Platte, Nebraska taken at 0000Z, June 19, 1975.

3. Calculate a mean temperature in each layer using:

$$\bar{T}_1 = \frac{T_1 + T_{1_{low}}}{2}$$

$$\bar{T}_2 = \frac{T_2 + T_{2_{up}}}{2}$$

4. Using the hydrostatic equation, calculate  $\Delta z_1$ , between  $P_1$  and  $P_{1_{low}}$ , and  $\Delta z_2$  between  $P_2$  and  $P_{2_{up}}$ . Using the equation of state to substitute for  $\rho$  in the hydrostatic equation, the solutions for  $\Delta z_1$  and  $\Delta z_2$  become:

$$\Delta z_1 = \frac{R\bar{T}_1}{g} \ln \left( \frac{P_{1_{low}}}{P_1} \right)$$

$$\Delta z_2 = \frac{\bar{RT}_2}{g} \ln \left( \frac{P_2}{P_{2up}} \right)$$

5. Using Poisson's equation, calculate  $\theta$  for each of the four pressure levels. For example:

$$\theta_2 = T_2 \left( \frac{1000}{P_2} \right)^{.286}$$

6. Solve for  $N_1^2$  and  $N_2^2$  using the finite difference form of equation (3.22):

$$N_1^2 = \frac{g}{\Delta z_1} \ln \left( \frac{\theta_1}{\theta_{1low}} \right)$$

$$N_2^2 = \frac{g}{\Delta z_2} \ln \left( \frac{\theta_{2up}}{\theta_2} \right)$$

Once these parameters are determined, equation (3.94) is solved for  $c$ , for selected  $\Delta u_o$  and  $\lambda$ . This is done by iteration using "Muller's Method with Deflation," which is contained in Colorado State University IMSL subroutine ZANLYT.

As was described in section 3.2, the real component of  $c$  is the phase speed of the wave relative to the coordinate system where  $\bar{u}_o = 0$ . Therefore, the phase speed of the wave relative to the dome is:

$$c^* = c_r + \bar{u}_o^*$$

where:

$$\bar{u}_o^* = \frac{u_{o1}^* + u_{o2}^*}{2}$$

and  $c^*$ ,  $\bar{u}_o^*$ ,  $u_{o1}^*$ , and  $u_{o2}^*$  are now measured relative to the dome.

Therefore:

$$c^* = \frac{u_{o1}^* + u_{o2}^*}{2} + c_r$$

Also,  $\Delta u_o$  is the same regardless of the coordinate system. Thus:

$$\Delta u_o = u_{o_1} - u_{o_2} = u_{o_1}^* - u_{o_2}^*$$

$$\therefore c^* = \frac{\Delta u_o}{2} + u_{o_2}^* + c_r \quad (4.1)$$

This equation is used to calculate  $c^*$ , the phase speed relative to the dome, when  $\Delta u_o$ ,  $u_{o_2}^*$ , and  $c_r$  are known. Since  $u_{o_2}^*$  is the stratospheric wind speed relative to the dome, it is calculated by subtracting the dome's motion from the observed stratospheric wind on the nearest sounding.

#### 4.2 Tropical

The data used to analyze the tropical cases is summarized in Table 4.2. The method of analysis is essentially the same as for the mid-latitude cases. However, the map scale factor for DMSP photographs is given as  $1:1.5 \times 10^7$  and is assumed uniform in all directions throughout each photograph. This is permitted because the satellite is more directly overhead in the DMSP photographs than in the mid-latitude SMS-2 photographs.

Table 4.2. Tropical Data Sources

<u>Type of Data</u>	<u>Time of Observations</u>	<u>Data Source</u>
Satellite Photographs	Once per case, usually near 2300Z	DMSP photographs received at observing sites in the western Pacific
Upper air soundings	00Z and 12Z daily	"Daily Weather Maps with Synoptic Data Tabulation," pub- lished by Japan Meteorological Agency, Tokyo, Japan
Daily Synoptic Maps	00Z and 12Z for surface analysis, 12Z for upper air analysis	"Daily Weather Maps with Synoptic Data Tabulation," pub- lished by Japan Meteorological Agency, Tokyo, Japan

## 5. CASE STUDIES

### 5.1 Nebraska

Between 2300Z on June 18, 1975 and 0230Z on June 19, 1975, a severe thunderstorm cell moved through Central Nebraska, spawning eight tornadoes over a nearly continuous path 170 km long (Fig. 5.1). This storm is the subject of our first case study and will henceforth be referred to as the "Nebraska" storm.

Figure 5.2 contains SMS-2 visual photographs showing the early evolution of the storm. The rapid growth of this storm is evident in these photographs. The radar reports from Grand Island, Nebraska during the most active period of the storm are plotted in Figure 5.3. Notice

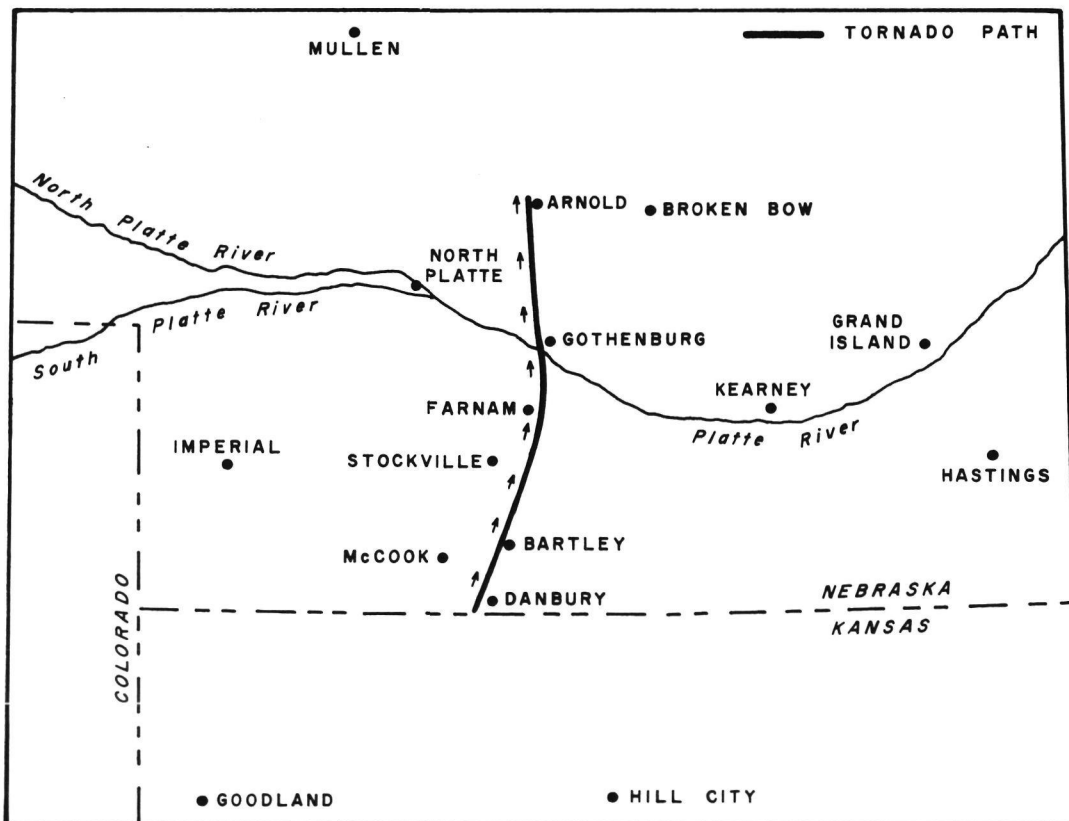
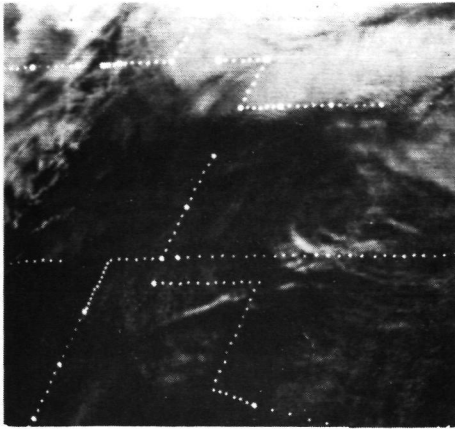
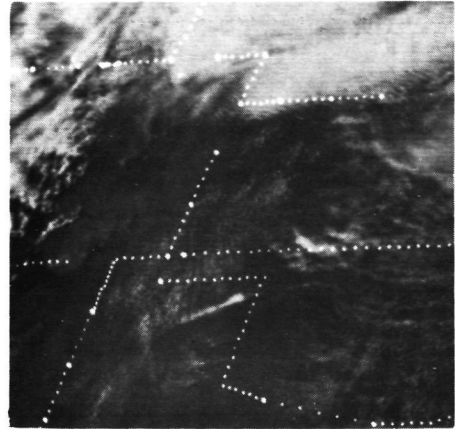


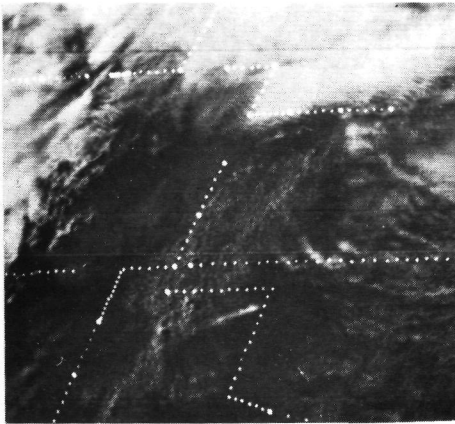
Figure 5.1. Path of tornadoes spawned by Nebraska storm on June 18, 1975.



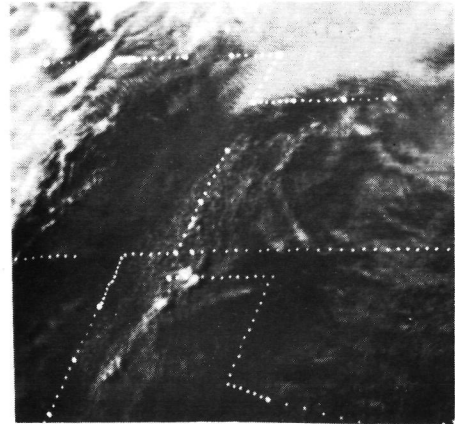
2000Z



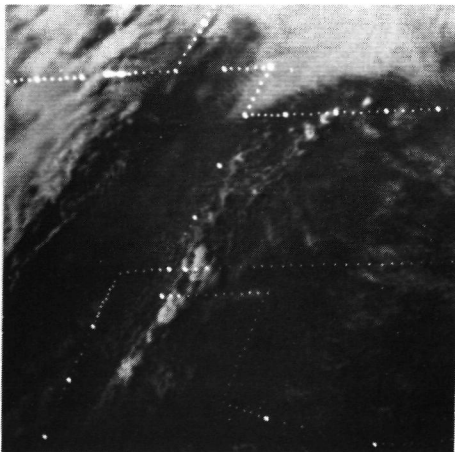
2030Z



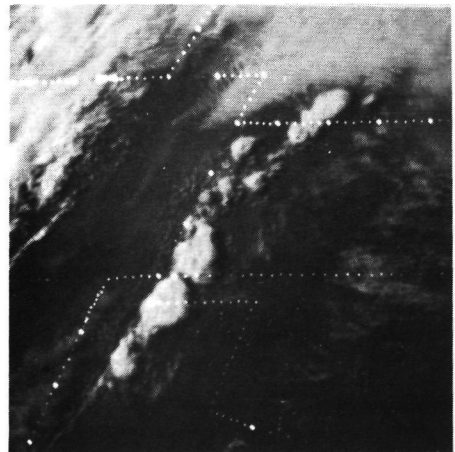
2100Z



2130Z

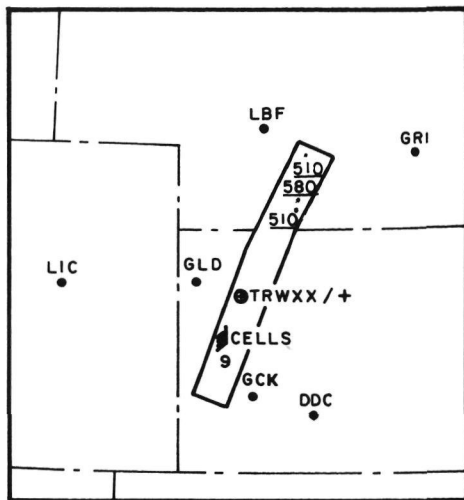


2200Z

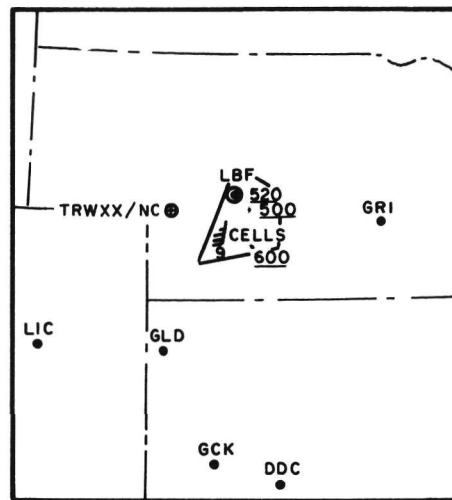


2230Z

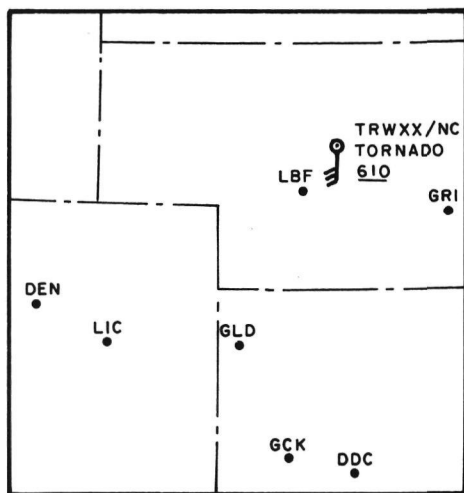
Figure 5.2. SMS-2 visual photographs taken over the Kansas-Nebraska area on June 18, 1975.



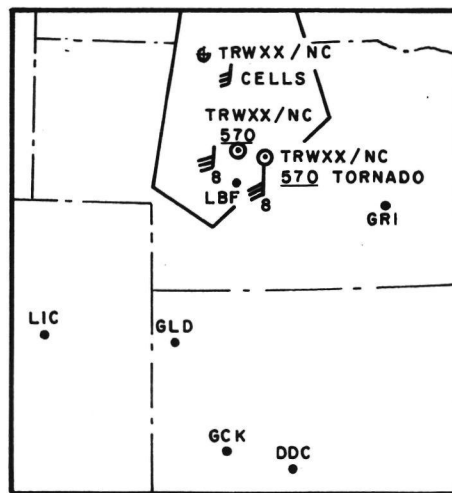
2330Z 18 Jun 75



0030Z 19 Jun 75



0205Z 19 Jun 75  
 (Only the tornado cell was  
 reported on this special)



0230Z 19 Jun 75

Figure 5.3. Grand Island, Nebraska radar summaries during period of tornado activity.

that the tornado producing cell was in the southeast section of the echo region and that its top remained between 57,000 ft and 61,000 ft. Also, note that the cell movement was southerly at approximately 15 kts throughout the period.

The concentric waves atop the cirrus outflow region of this storm first appeared on the 2317Z SMS-2 photograph (Fig. 5.4). They remained visible until 0147Z (Figs. 5.5 - 5.7), when sunset prevented the taking of any further visual photographs. Table 5.1 summarizes the wavelengths,

Table 5.1. Nebraska Case Cloud Measurements

QUADRANT	TIME	WAVELENGTH (km)	AMPLITUDE <sup>1</sup> (km)	RADIUS <sup>2</sup> (km)	OUTFLOW RATE <sup>3</sup> (m/sec)
North	2317Z	--	--	70	18
	0102Z	--	--	185	8.5
	0132Z	--	--	200	--
	0147Z	--	--	--	--
East	2317Z	10	1-3	75	23
	0102Z	11	1.5-3	220	22
	0132Z	11-14.5	.35-.85	260	28
	0147Z	11-14.5	.25-.40	285	--
South	2317Z	--	--	30	11
	0102Z	--	--	100	--
	0132Z	--	--	--	--
	0147Z	--	--	--	--
West	2317Z	10	--	60	17.5
	0102Z	--	--	170	5.5
	0132Z	--	--	180	11
	0147Z	--	--	190	--

<sup>1</sup>See Appendix A.

<sup>2</sup>Relative to southeast dome.

<sup>3</sup> $(\Delta \text{ Radius}) \div (\Delta \text{ time})$ . This is the radial speed of the cloud boundary.

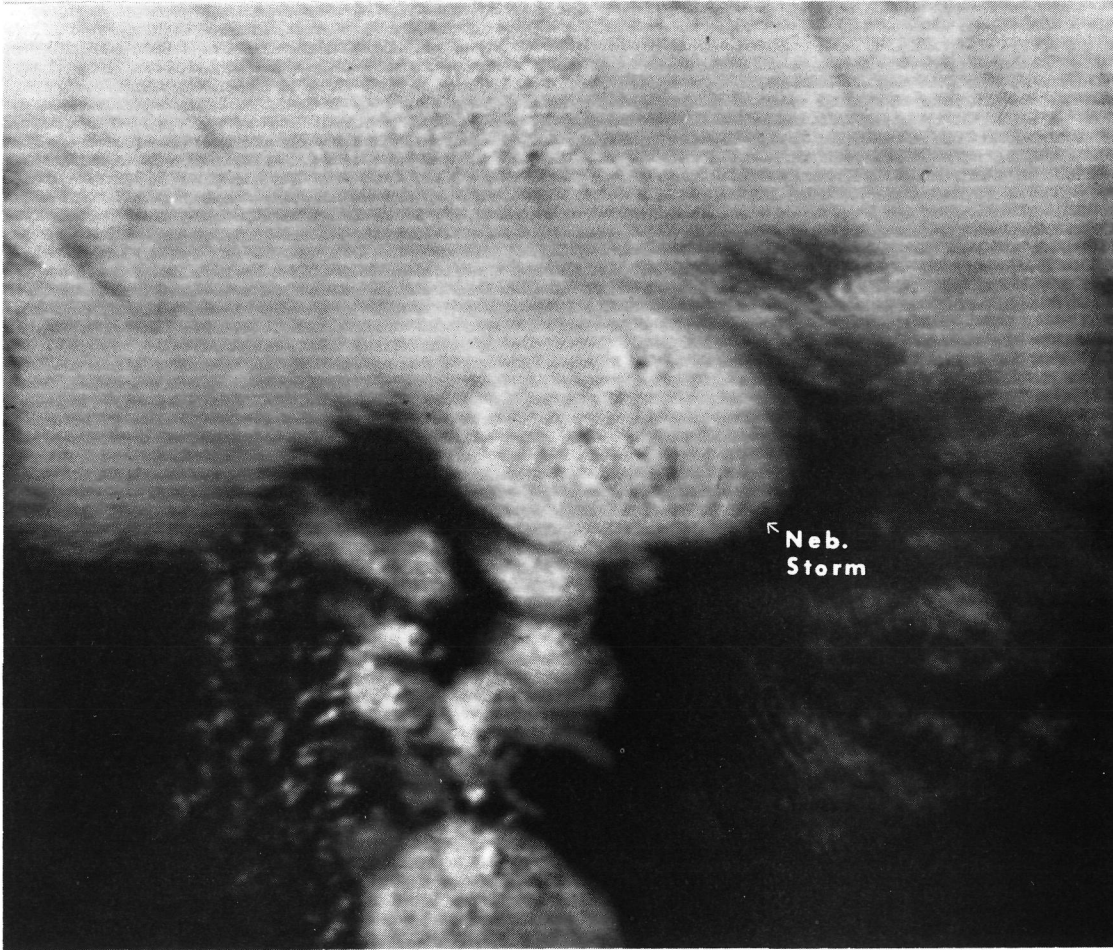


Figure 5.4. SMS-2 visual photograph taken over Nebraska at 2317Z, June 18, 1975.

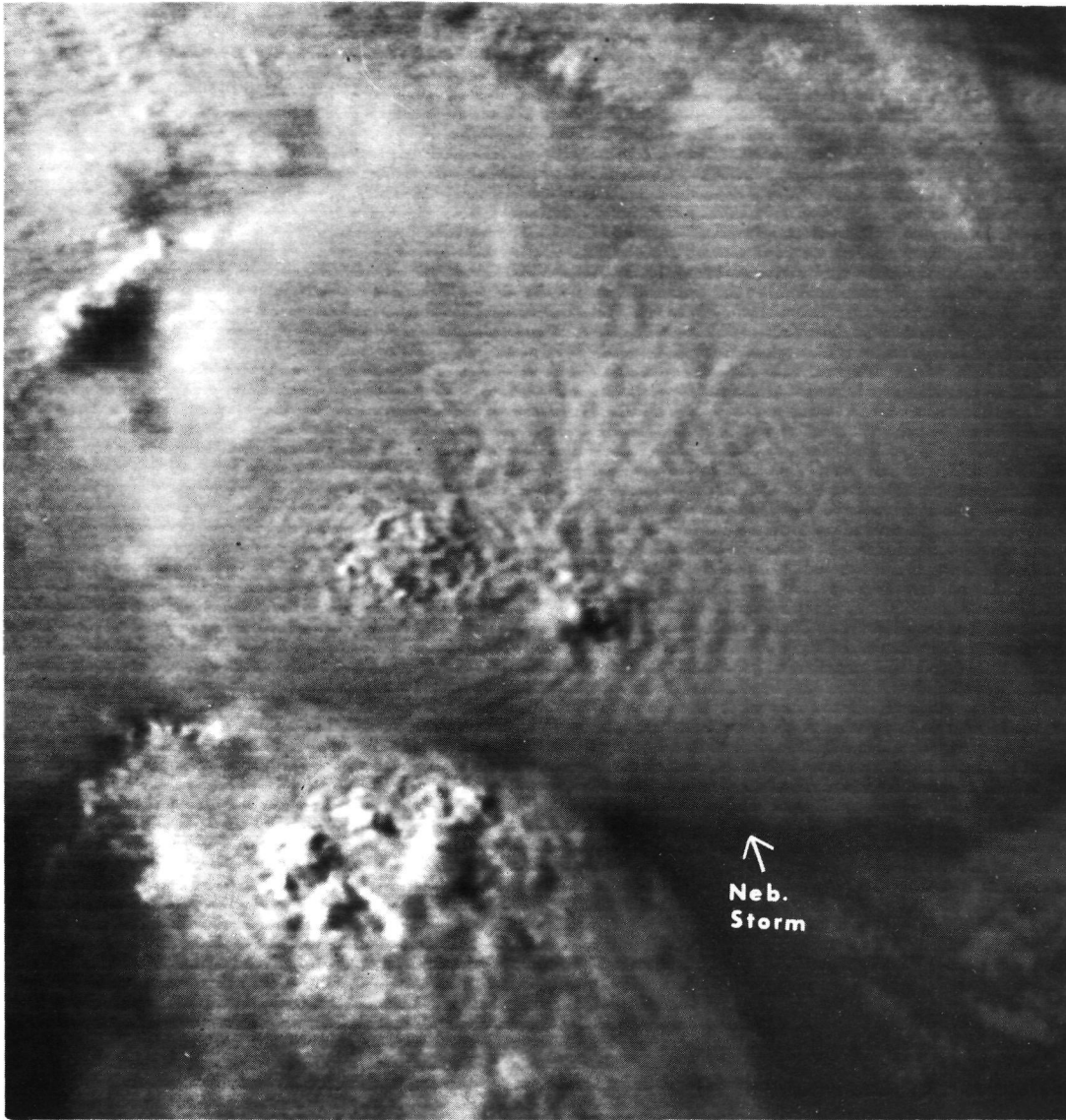


Figure 5.5. SMS-2 visual photograph taken over Nebraska at 0102Z, June 19, 1975.

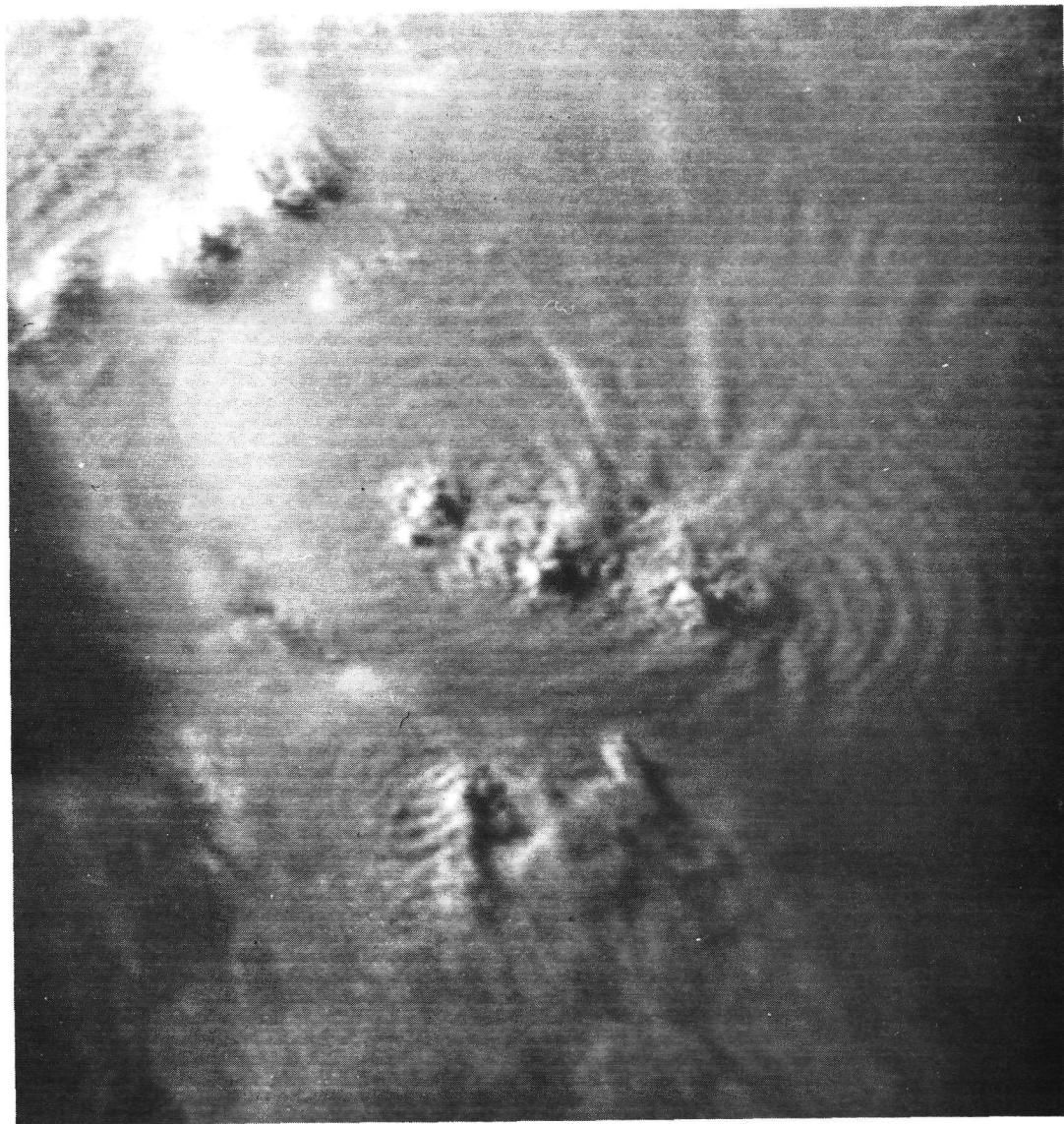


Figure 5.6. SMS-2 visual photograph taken over Nebraska at 0132Z, June 19, 1975.

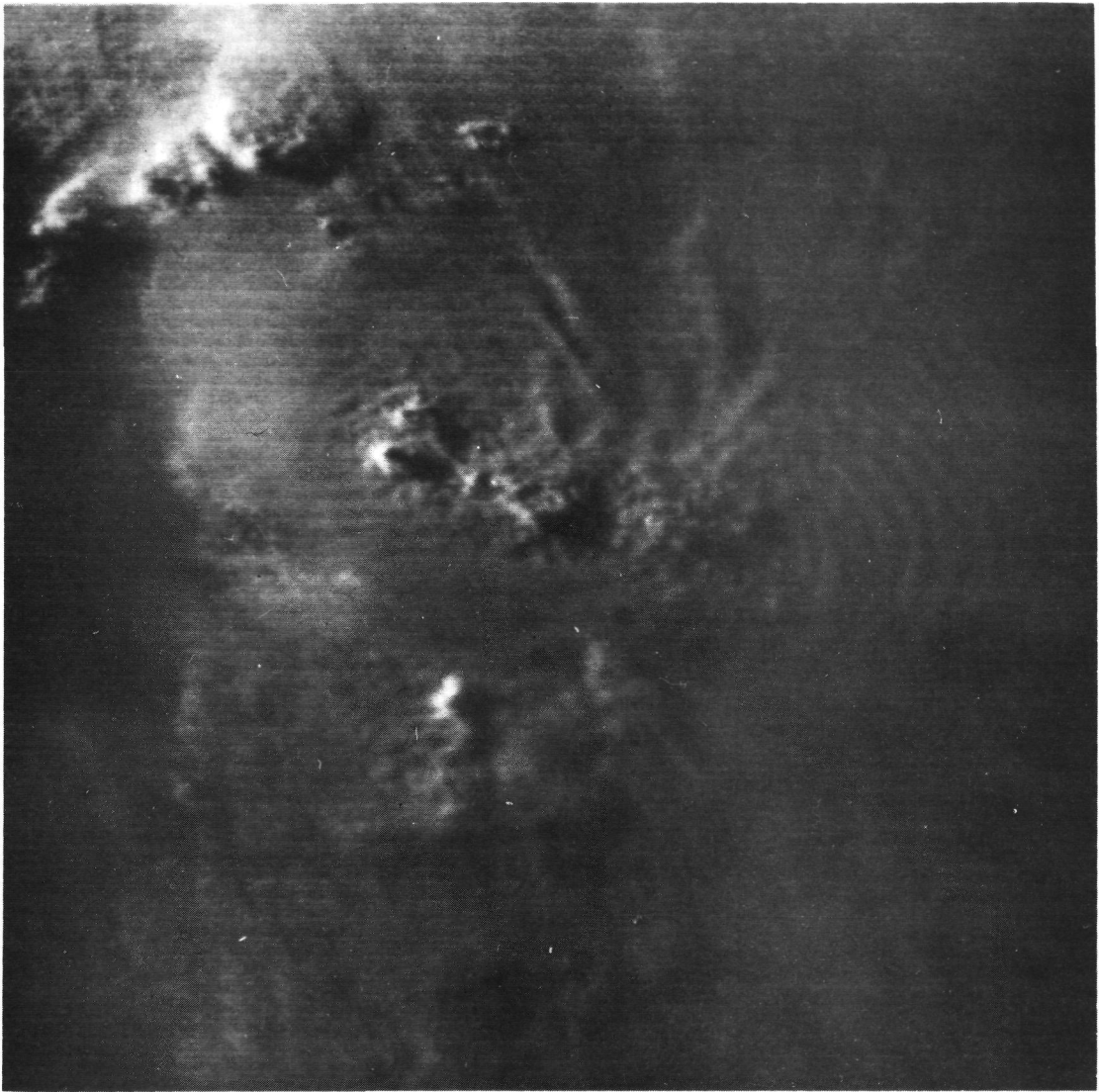


Figure 5.7. SMS-2 visual photograph taken over Nebraska at 0147Z, June 19, 1975.

amplitudes, cirrus radii, and computed cirrus outflow rates for each photograph.

The vertical profiles of wind and temperature from the 0000Z North Platte, Nebraska sounding on this date, are given in Figures 5.8 and 5.9. Table 5.2 lists the parameters from this sounding that were used to solve equation (3.94).

Table 5.2. Thermal Parameters for Nebraska Case

---

$T_{2_{up}} = 212^{\circ}\text{K}$	$P_{2_{up}} = 125 \text{ mb}$		
$T_2 = 212^{\circ}\text{K}$	$P_2 = 150 \text{ mb}$	$\theta_2 = 364.7^{\circ}\text{K}$	$N_2^2 = 4.51 \times 10^{-4} \text{ sec}^{-1}$
$T_1 = 206.7^{\circ}\text{K}$	$P_1 = 153 \text{ mb}$	$\theta_1 = 353.6^{\circ}\text{K}$	$N_1^2 = 2.12 \times 10^{-4} \text{ sec}^{-1}$
$T_{1_{low}} = 215.3^{\circ}\text{K}$	$P_{1_{low}} = 200 \text{ mb}$		

---

Before discussing the results of equation (3.94), let us first examine some of the important features exhibited by the data just presented:

1. The radar reports (Fig. 5.3) indicate that the sounding was taken less than 50 km north of the storm's center. The satellite photographs also indicate that the sounding very likely passed through the cirrus outflow layer of the northern portion of the storm.
2. The observed wind maximum near the tropopause (Fig. 5.9) appears to be the result of the intense cirrus outflow at that level. The shallowness of the wind maximum and the fact that it is near the layer where cirrus outflow would be expected, help support this conclusion. The presence of a

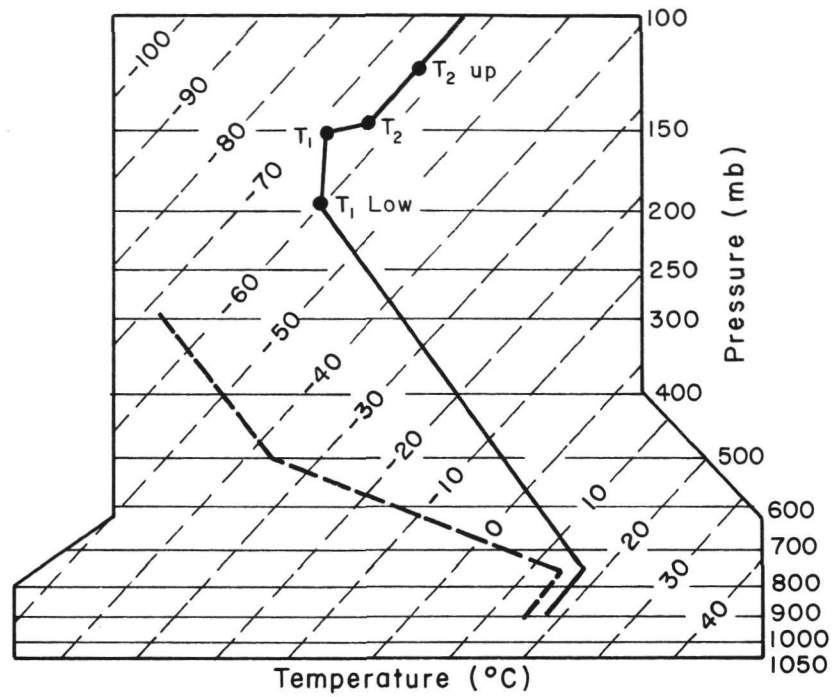


Figure 5.8. Temperature sounding from North Platte, Nebraska taken at 0000Z, June 19, 1975.

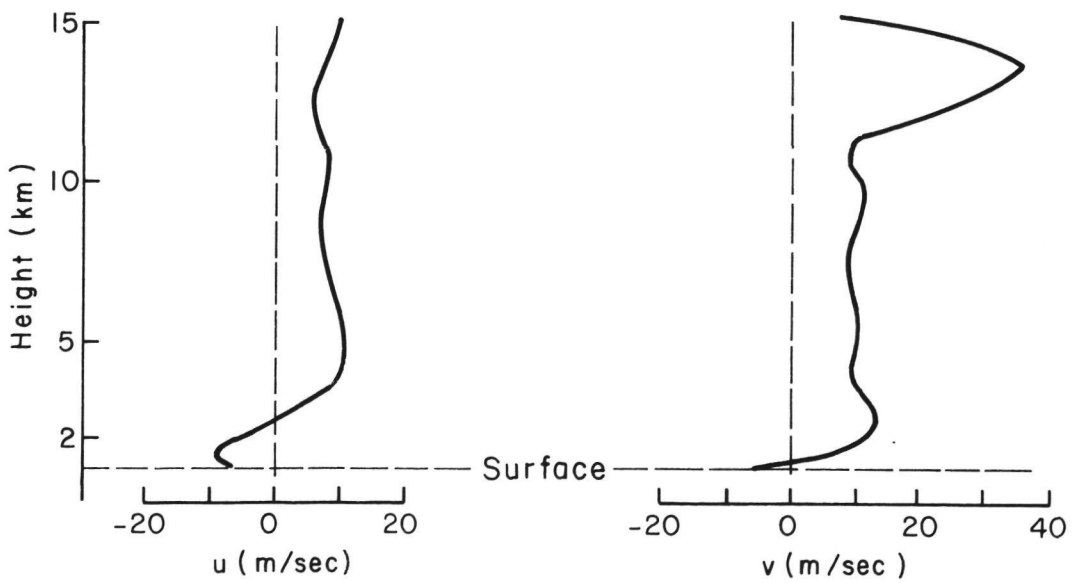


Figure 5.9. Wind profiles from North Platte, Nebraska sounding at 0000Z, June 19, 1975.

jet stream to the west and north of the area (Fig. 5.10), however, indicates that this could also be the result of a larger scale feature. In any event,  $\Delta u_0$  across the tropopause is nearly 30 m/sec in this area.

3. The eastern quadrant of the cirrus outflow contained the most distinct wave pattern throughout the period (Figs. 5.4 - 5.7). It also had the strongest outflow rate (Table 5.1).



Figure 5.10. Winds at 35,000 ft over the Western United States at 0000Z, June 19, 1975.

4. Since the radius measurements were made with respect to the southeastern dome (Table 5.1), the southern and eastern outflow rates are most likely good indications of the radial wind speed at cloud level. In the western and northern quadrants, however, outflow from new cells (Figs. 5.3-5.7) enhances the motion of the cloud boundary. Wind speeds at cloud level cannot, therefore, be accurately inferred by cloud expansion rates in these quadrants.
5. The stratospheric wind relative to the dome (Figs. 5.3 and 5.9) is approximately westerly at 10 m/sec. Therefore, the average  $\Delta u_0$  at the eastern cloud edge is 15 m/sec.
6. The top of the southeastern dome, according to the radar reports (Fig. 5.3), remained between 2 km and 5 km above the tropopause during the period for which waves were visible. The dome's diameter, estimated from the 0132Z satellite photograph (Fig. 5.6), was approximately 11 km.
7. The wavelengths in the eastern quadrant remained fairly constant throughout the period (Table 5.1), averaging about 11 km. In the 0132Z and 0147Z photographs (Figs. 5.6 - 5.7), however, waves in the far eastern portion of the outflow increased to a wavelength of about 14.5 km.
8. The amplitude of the waves showed a marked decrease from 0102Z to 0147Z (Table 5.1).

The thrust of all this is that there appears to be sufficient evidence that (1) a substantial tropopause penetration did occur in the form of an overshooting dome, (2) the cirrus outflow created some degree of wind shear across the tropopause, (3) the diameter of the

dome is of the same scale as the wavelength, and (4) the waves occurred in the area of apparent maximum wind shear across the tropopause.

Using the data from Table 5.2, we will now evaluate equation (3.94) for various  $\lambda$  and  $\Delta u_0$ . In doing so, we will attempt to evaluate the model's applicability to the case. Figure 5.11 shows the variation of  $|c_i|$  (magnitude of the imaginary component of the phase speed) and  $c^*$  (real component of the phase speed measured relative to the dome) with respect to  $\Delta u_0$ , when  $\lambda$  is held constant. Notice that each wavelength is unstable only over a certain range of  $\Delta u_0$  for which a purely real solution for  $c$  does not exist. For values of  $\Delta u_0$  either side of this range, neutral stability prevails. This result is quite unlike that obtained by the incompressible Helmholtz equation (Fig. 5.12), where  $|c_i|$  continues to increase once a critical  $\Delta u_0$  is attained.

From section 3.2 we saw that the stability amplification factor,  $\psi$ , equals  $\cosh(\mu c_i t)$ . Figure 5.13 contains a sample plot of  $\psi$  vs  $\lambda$  for a given  $\Delta u_0$  and  $t = 30$  minutes. Notice that the plot has two humps. This is consistent with the two hump configuration of  $|c_i|$  vs  $\Delta u_0$  in Figure 5.11. Plots of the right hump only and the left hump only of the  $\psi$  vs  $\lambda$  curves for a series of  $\Delta u_0$  and  $t = 30$  minutes, are given in Figures 5.14 and 5.15.

Using Figures 5.14 and 5.15, curves of  $\Delta u_0$  vs  $\lambda$  for a constant  $\psi$  are plotted in Figure 5.16. This graph shows that for a given  $\Delta u_0$ , a certain range of  $\lambda$ 's will be the most unstable. The two humps again appear, this time as two axes of maximum instability.

Let us now return to the observations to evaluate the model's results. First of all, the average wavelength is 11 km. Secondly,

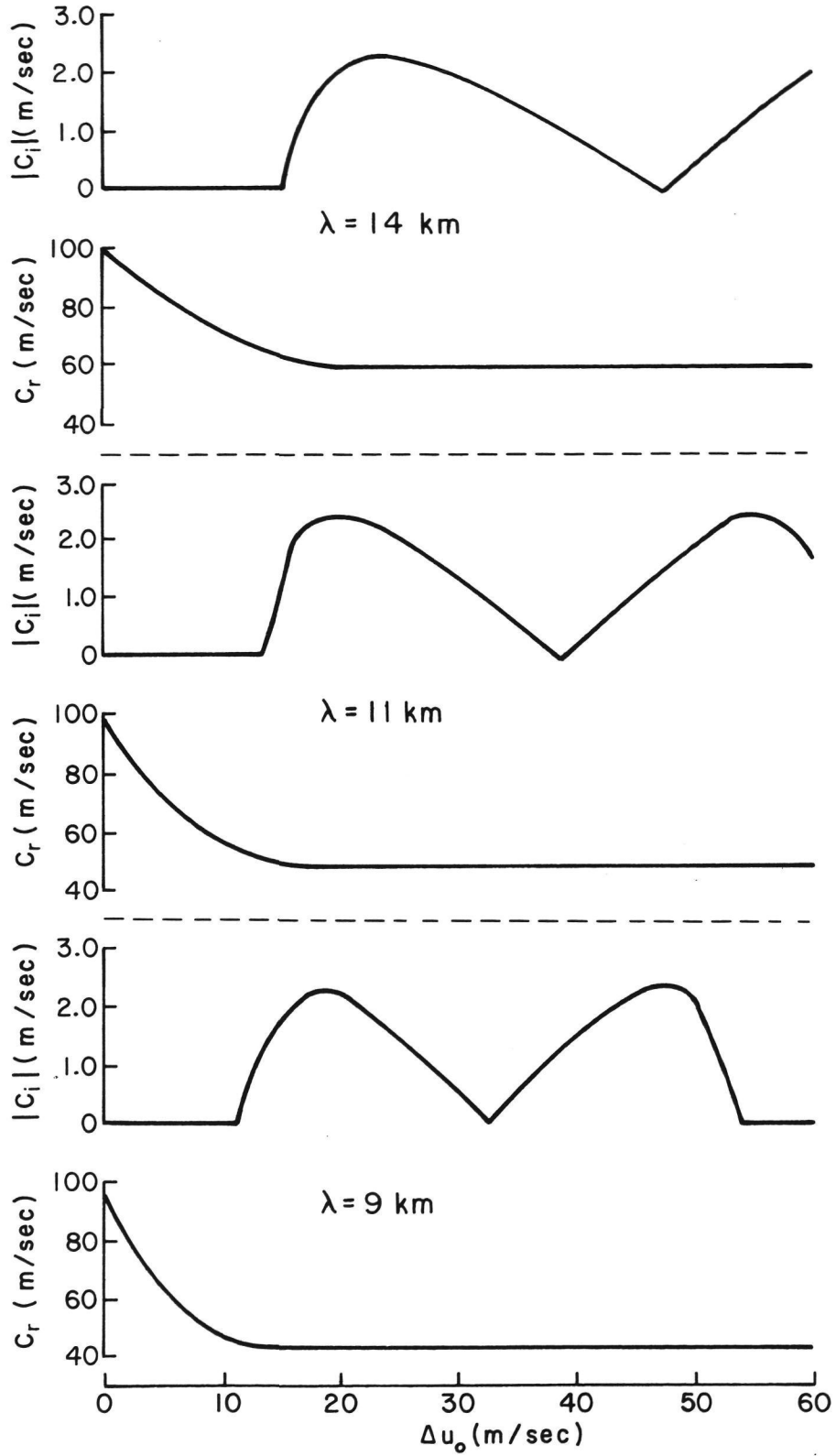


Figure 5.11.  $|c_i|$  and  $c_r$  versus  $\Delta u_o$  for selected  $\lambda$  (Nebraska case).

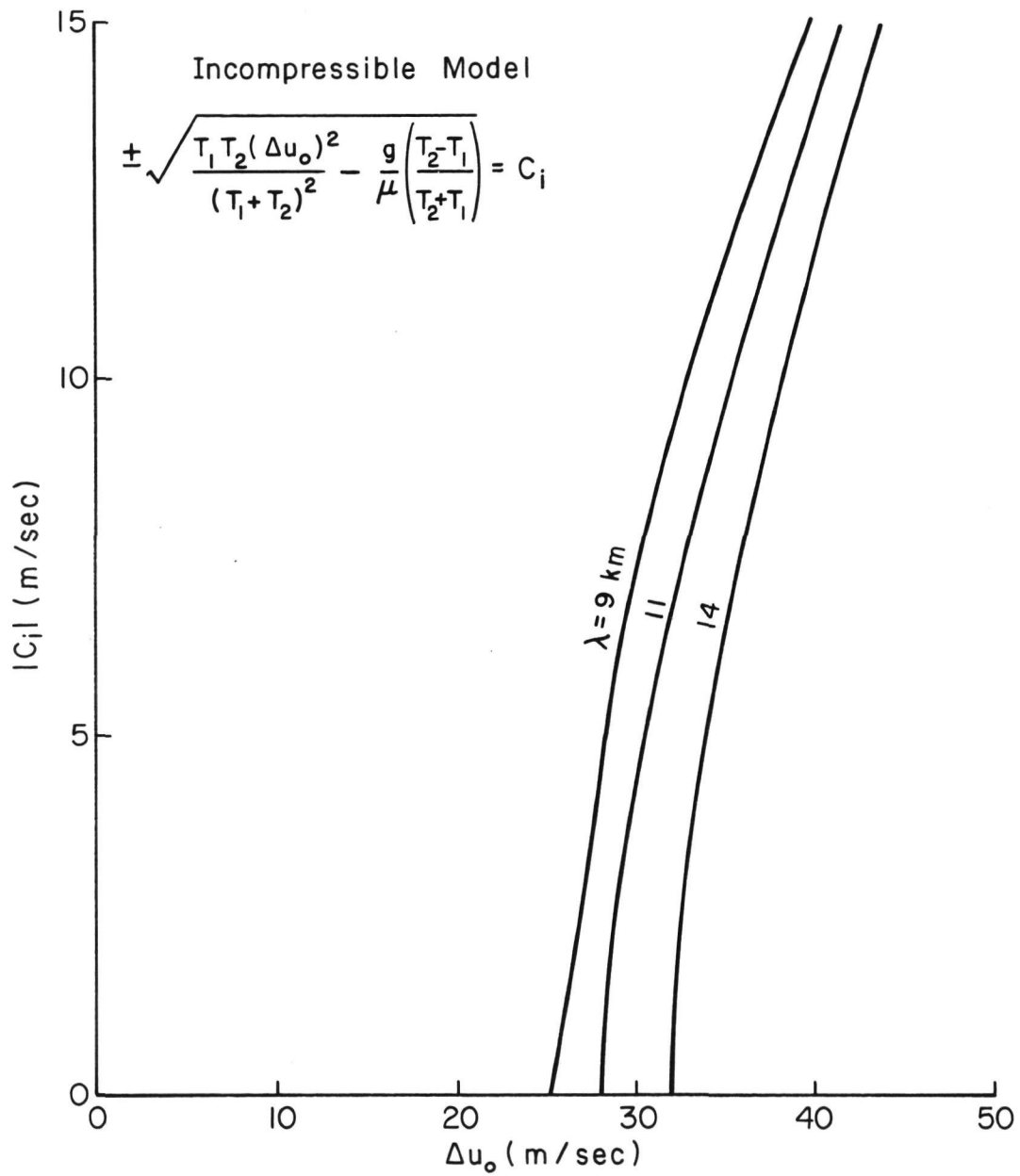


Figure 5.12.  $|c_i|$  versus  $\Delta u_o$  for selected  $\lambda$  (Incompressible model, Nebraska case).

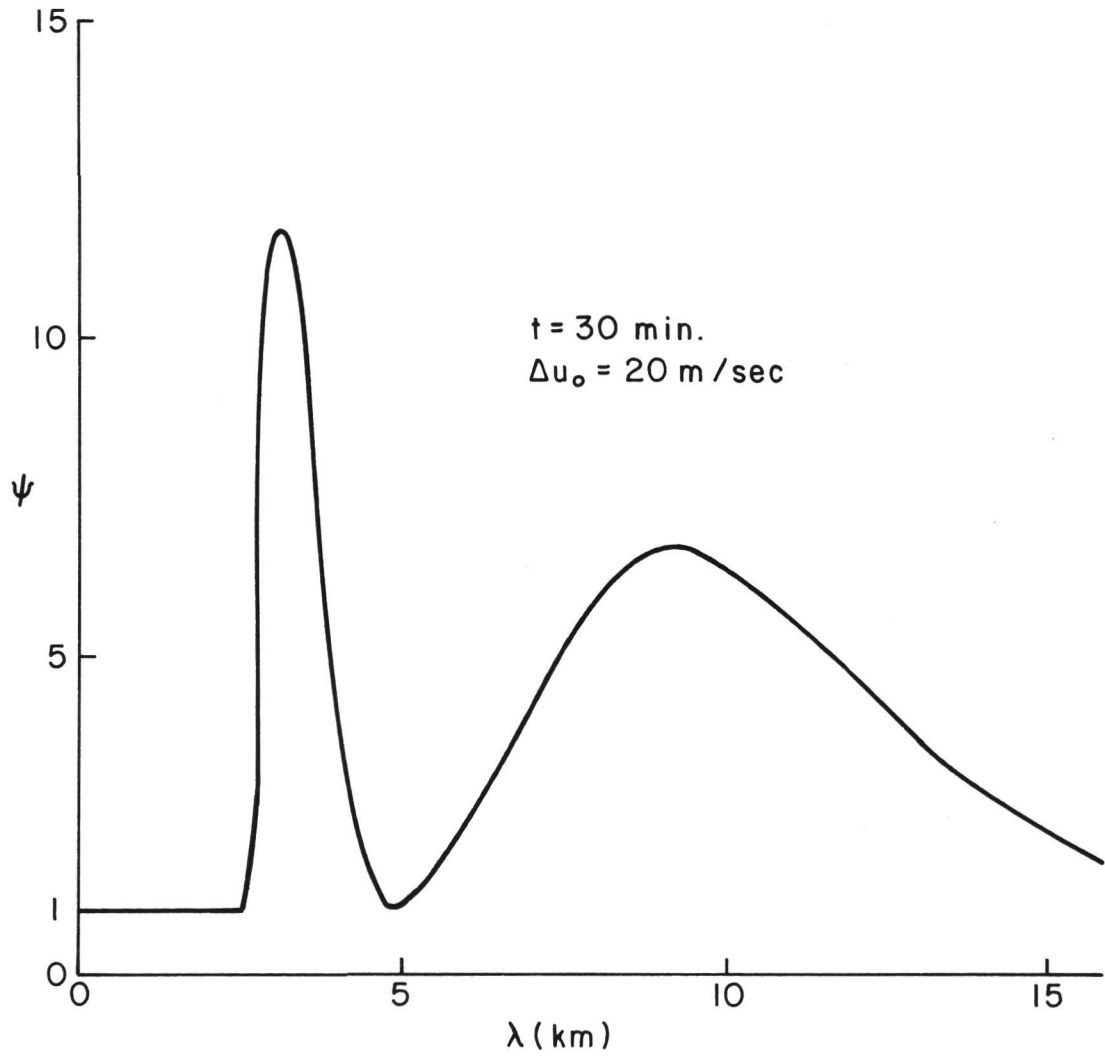


Figure 5.13.  $\psi$  versus  $\lambda$  curve for  $\Delta u_0 = 20 \text{ m/sec}$  (Nebraska case).

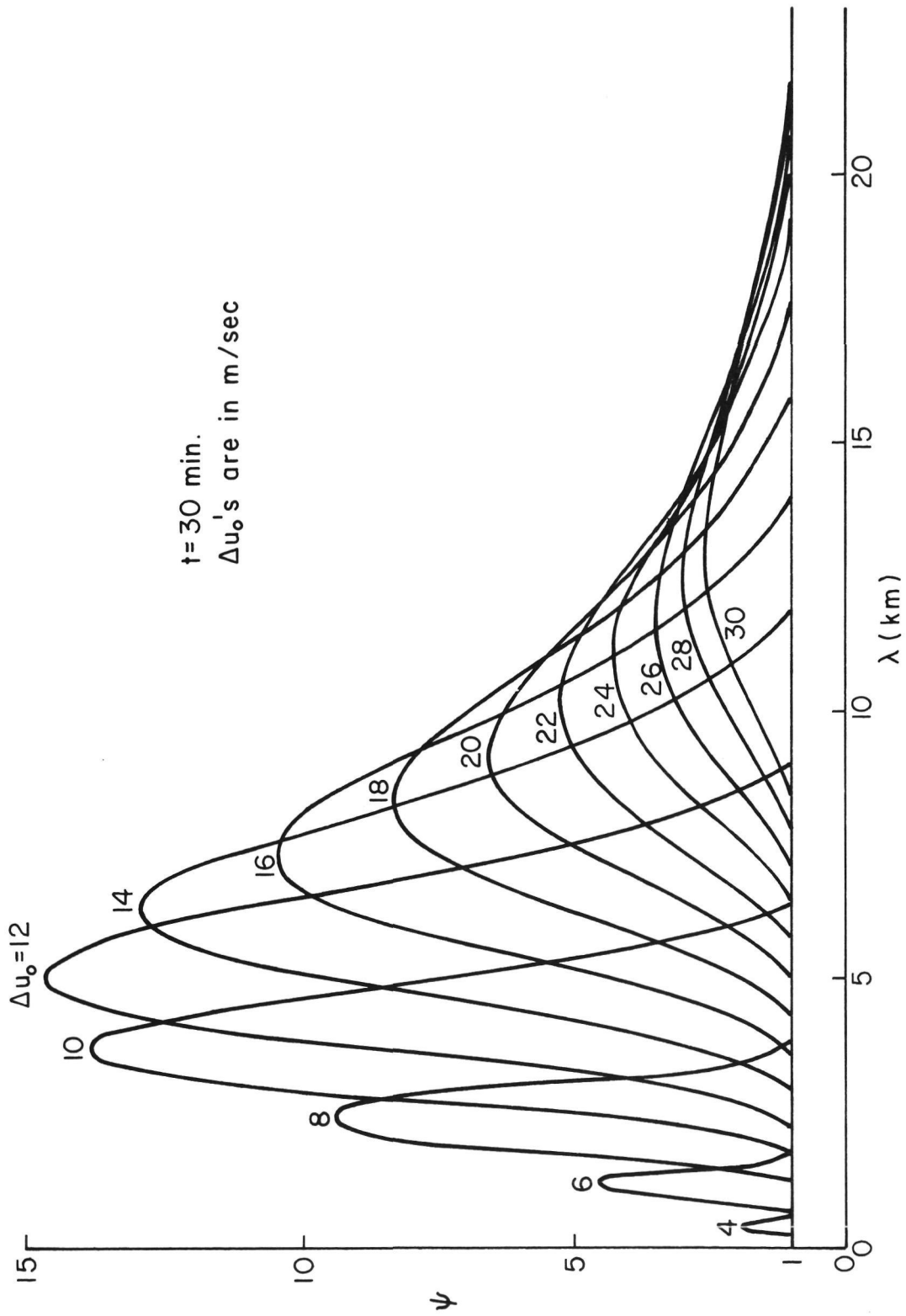


Figure 5.14. Right hump of  $\psi$  versus  $\lambda$  curves for selected  $\Delta u_0$ 's (Nebraska case).

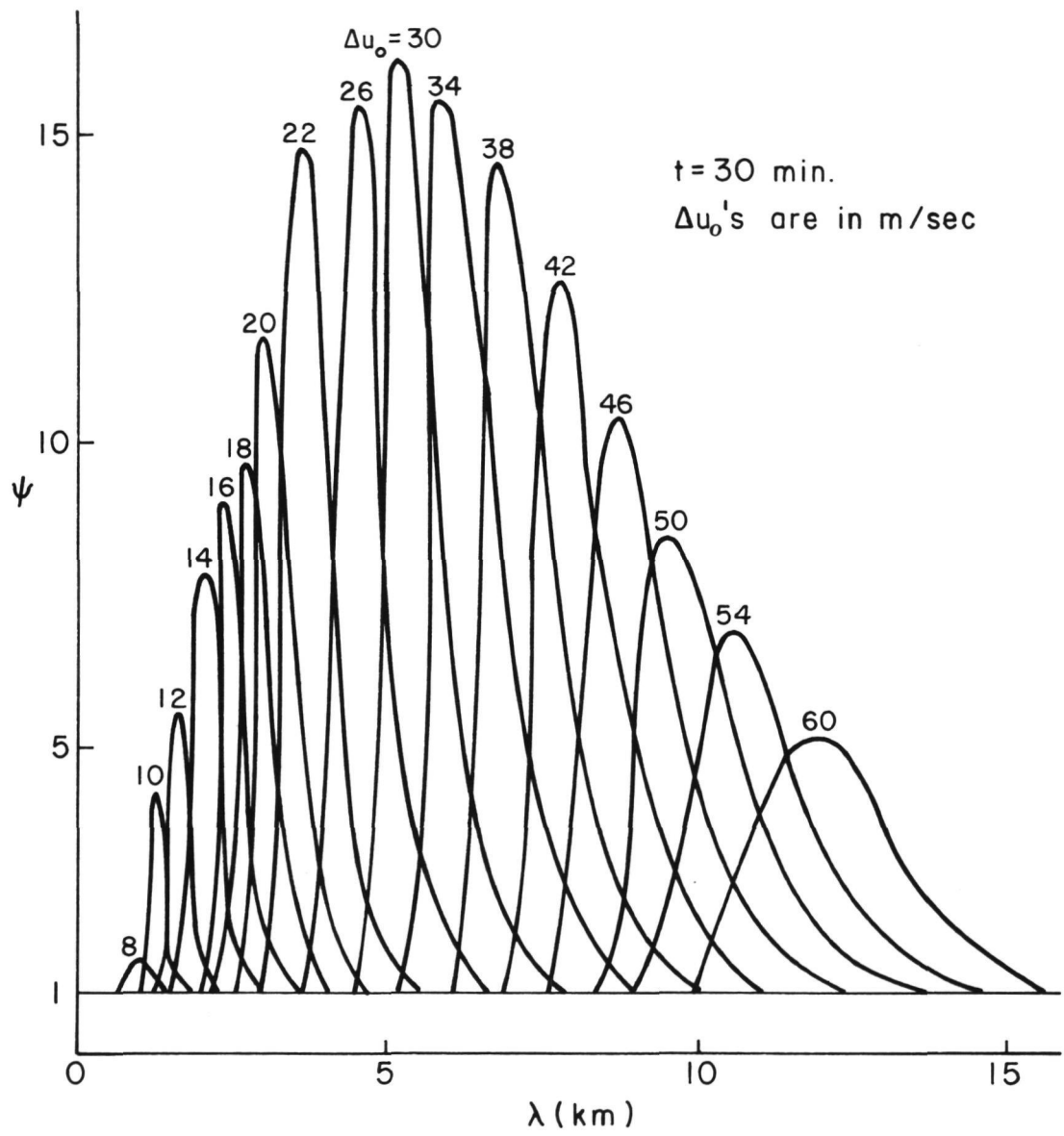


Figure 5.15. Left hump of  $\psi$  versus  $\lambda$  curves for selected  $\Delta u_0$ 's (Nebraska case).

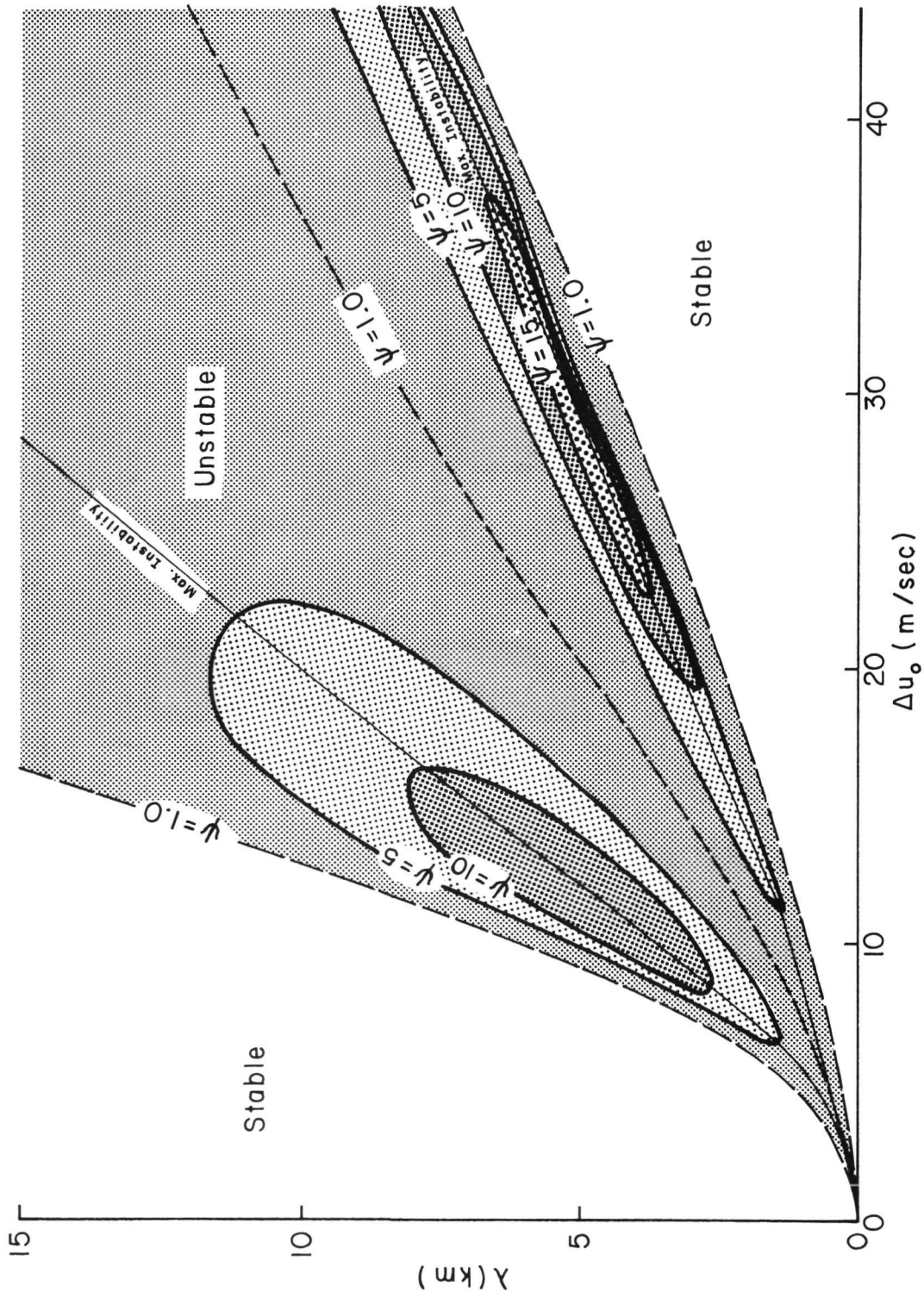


Figure 5.16.  $\Delta u_0$  versus  $\lambda$  curves for selected  $\psi$  at  $t = 30$  min (Nebraska case).

based on observed cirrus outflow rates and the sounding data,  $\Delta u_0$  in the area of the waves appears to be between 15 m/sec and 30 m/sec (Table 5.1 and Fig. 5.9). Figure 5.16 indicates that 11 km is one of two most unstable wavelengths when  $\Delta u_0 = 22$  m/sec and when  $\Delta u_0 = 56$  m/sec. Thus, for the lower predicted value of  $\Delta u_0$ , at least, the data does appear to be in fair agreement with the model. However, if, in fact,  $\Delta u_0 = 22$  m/sec, Figure 5.16 would indicate that  $\lambda = 3.7$  km would be even more unstable than  $\lambda = 11$  km. The apparent absence of this wavelength may be related to the fact that the dome's diameter is approximately 11 km. A dome of this size would likely produce higher amplitude waves at  $\lambda = 11$  km than at  $\lambda = 3.7$  km. Thus, even though  $\psi$  is slightly larger for  $\lambda = 3.7$  km, the 11 km wavelength waves still prevail since their initial amplitude was much larger.

There are two remaining observed wave characteristics that the model does not appear to predict. The first of these is the apparent drop in wave amplitude from 0102Z to 0147Z. The second is the increase in  $\lambda$  as the waves progress further eastward (Figs. 5.6 and 5.7). These two features may be related. Let us assume that near 0102Z the shear across the tropopause decreased rapidly to  $\Delta u_0 = 10$  m/sec. Figure 5.16 would indicate that the most unstable wavelength would now be approximately 3.5 km and wavelengths above 6.5 km would be stable. If, however, this decrease in  $\Delta u_0$  occurred rapidly,  $\psi$  for  $\lambda = 3.5$  km would still be relatively small since  $\psi$  increases with respect to time. Thus, we will attribute the absence of visible  $\lambda = 3.5$  km waves to the lack of time for amplification. The increase in  $\lambda$  further east may also be explained by this rapid drop of  $\Delta u_0$  to 10 m/sec. Figure 5.17 shows the dispersion curve for  $\Delta u_0 = 10$  m/sec. Notice

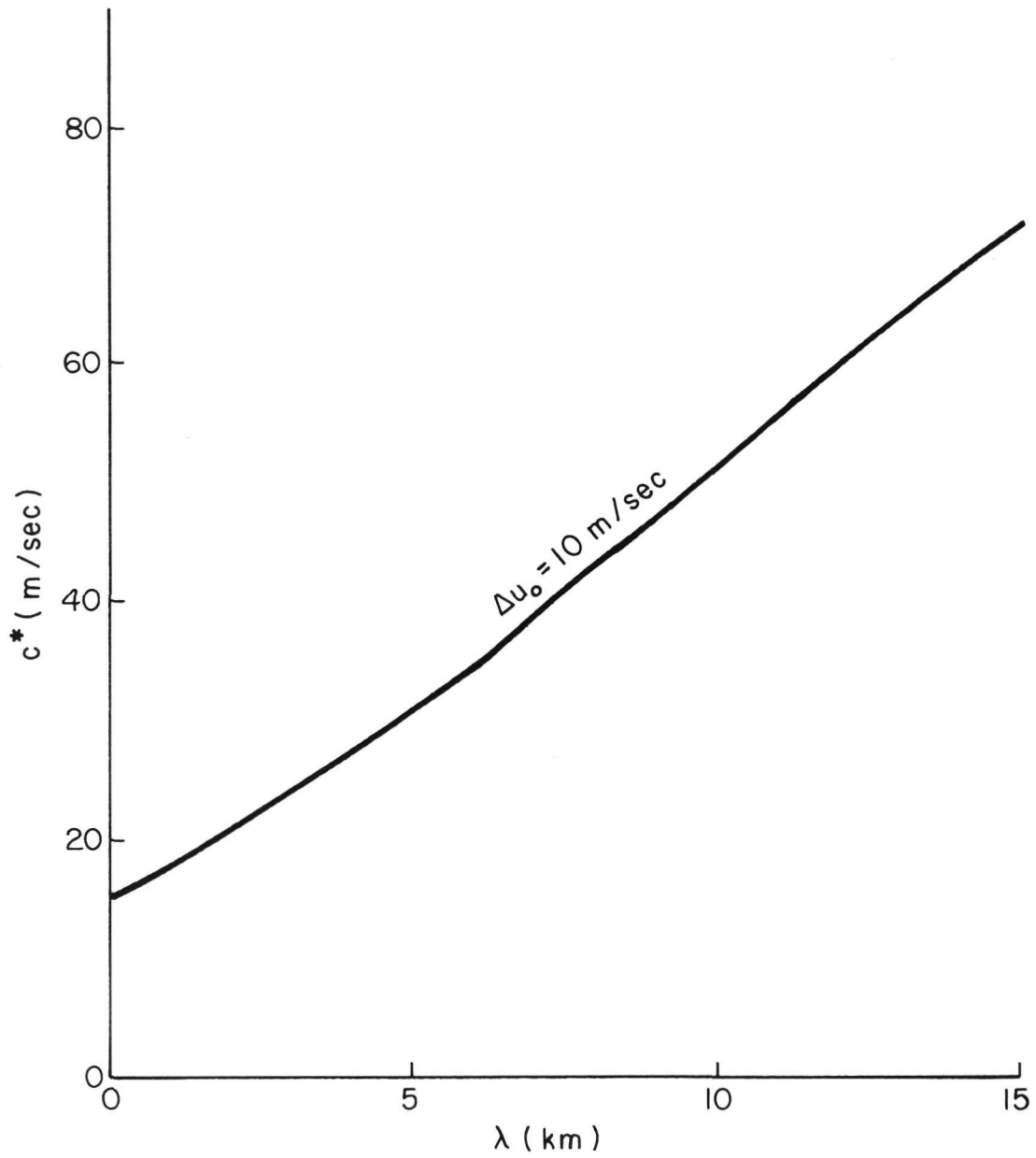


Figure 5.17. Dispersion curve for  $\Delta u_0 = 10 \text{ m/sec}$  (Nebraska case).

that the longer wavelengths move at a greater phase speed than the shorter wavelengths. Thus, just as in the case of a sea swell, the longer wavelengths will move out ahead of the shorter wavelengths. This appears to be the case in Figures 5.6 and 5.7.

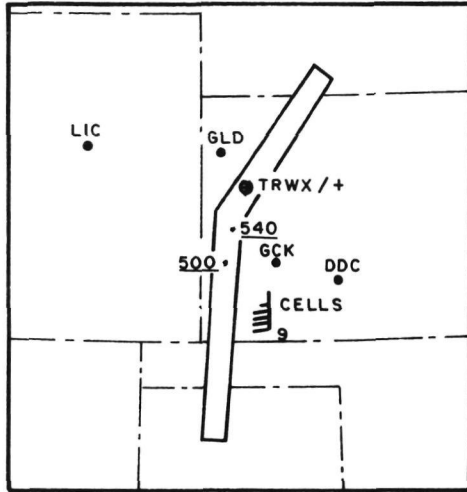
The conclusion, therefore, for this particular case, is that the stability model of section 3.2 can be used to describe some of the observed wave characteristics. However, lack of precise measurements over a substantial length of time prevent us from making a more rigorous evaluation of the model. This is especially true with respect to the features described in the preceding paragraph.

## 5.2 Kansas

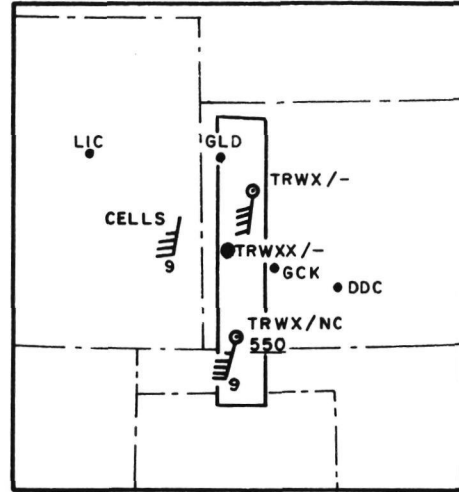
On the same date as the Nebraska storm, an intense squall line also developed over western Kansas and Oklahoma. We will refer to this storm as the "Kansas" case. This system produced several funnel clouds in its northern section, but none touched down. In the southern section, near Guyman, Oklahoma, golf ball sized hail was reported at about 0140Z on June 19, 1975.

Again, the early evolution of this storm system can be seen in Figure 5.2. The radar reports from Garden City, Kansas are given in Figure 5.18. Like the Nebraska storm, this system developed very rapidly. The average cell movement throughout the period was south-southwesterly at approximately 45 kts. The cell apparently responsible for the waves in this case was located near the Kansas-Oklahoma border on the 0030Z radar summary. Presumably, this cell was also responsible for the hail near Guyman, Oklahoma.

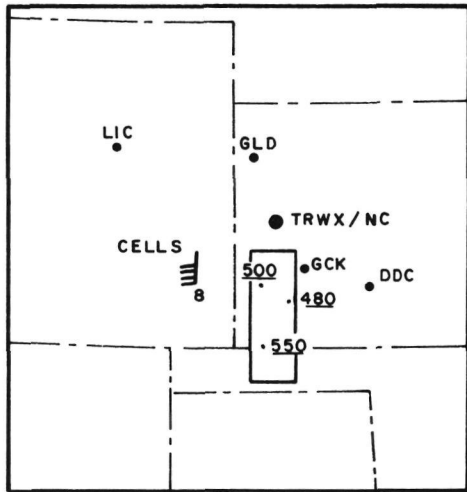
Wave patterns on the cirrus tops of this system appeared most evidently on the 2348Z SMS-2 photograph (Fig. 5.20). Photographs taken



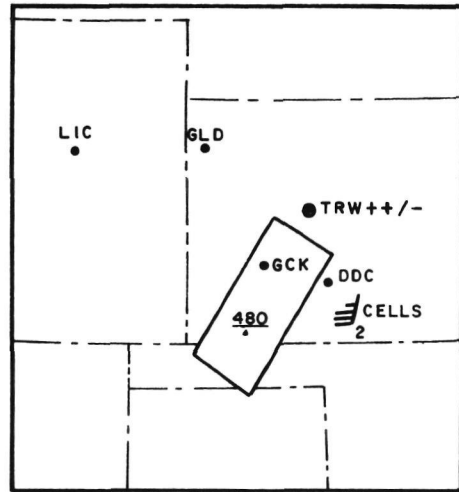
2330Z 18 Jun 75



0030Z 19 Jun 75



0130Z 19 Jun 75



0230Z 19 Jun 75

Figure 5.18. Garden City, Kansas radar summaries from June 18-19, 1975.

after this revealed very little wave activity (Figs. 5.20 - 5.24). The next photograph before 2348Z was taken at 2317Z (Fig. 5.19). It too contains no distinct wave features. Table 5.3 summarizes the key measurements taken from Figures 5.19 - 5.24.

The upper air sounding from Dodge City, Kansas, taken at 0000Z on this date is given in Figures 5.25 - 5.26. Table 5.4 lists the parameters from this sounding that were used to solve equation (3.94).

The important features to be noted in the data for this case are:

1. The radar reports (Fig. 5.18) indicate that the sounding was taken about 110 km east of the squall line's axis. The satellite data, however, indicates that the sounding passed just east of the cirrus outflow layer.
2. There was no dramatic wind shear observed at the tropopause level of the Dodge City sounding (Fig. 5.26).
3. The area of wave activity was also the area of maximum cirrus outflow (Fig. 5.19).
4. Only outflow rates perpendicular to the squall line were computed.
5. The stratospheric wind relative to the cells (according to the radar reports and the Dodge City sounding) was approximately northerly at 8 m/sec (Figs. 5.18 and 5.26). Therefore, the average  $\Delta u_0$  at the eastern cloud edge was 15 m/sec (this measurement was made at the maximum eastward cirrus outflow).
6. The diameter of the dome at the focus of the waves was approximately 8 km (Fig. 5.19).

As in the Nebraska case, there again appears to be sufficient evidence that (1) a substantial tropopause penetration occurred,

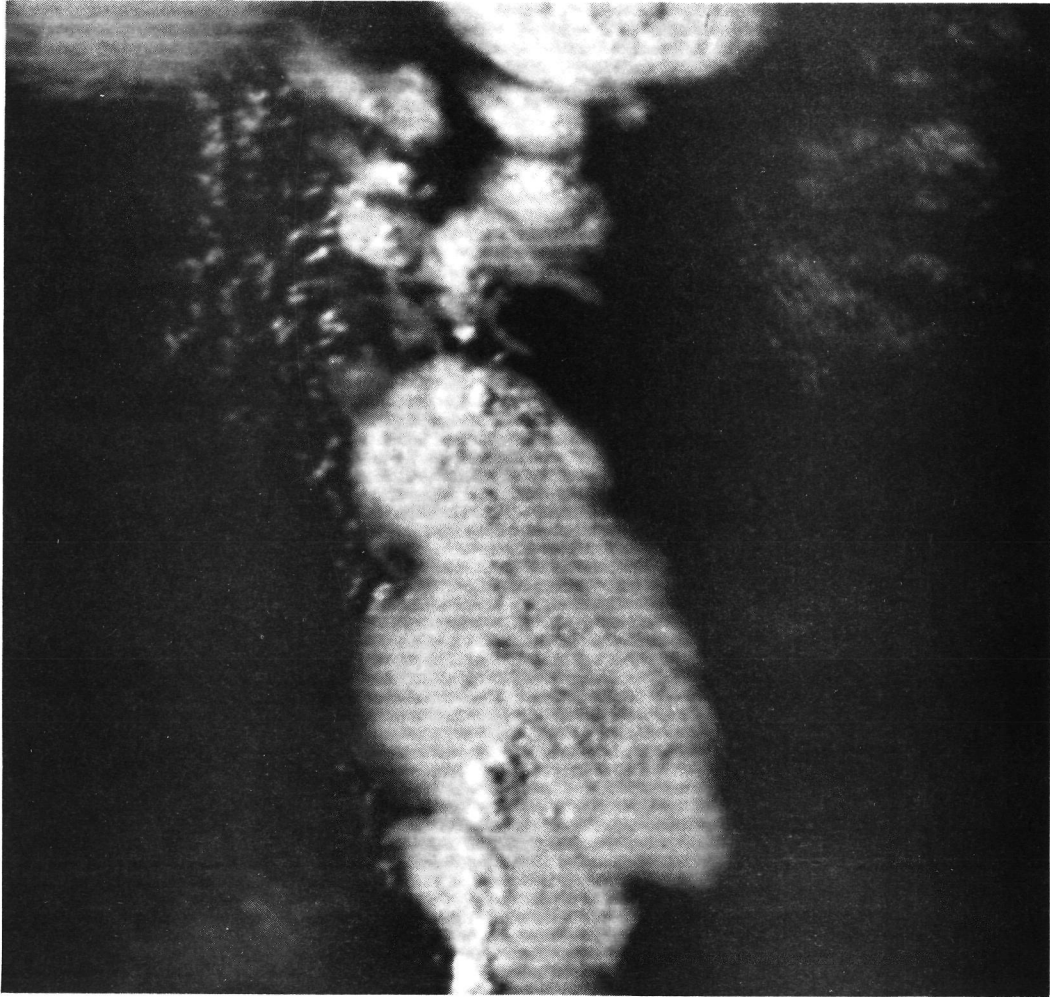


Figure 5.19. SMS-2 visual photograph taken over Kansas at 2317Z, June 18, 1975.

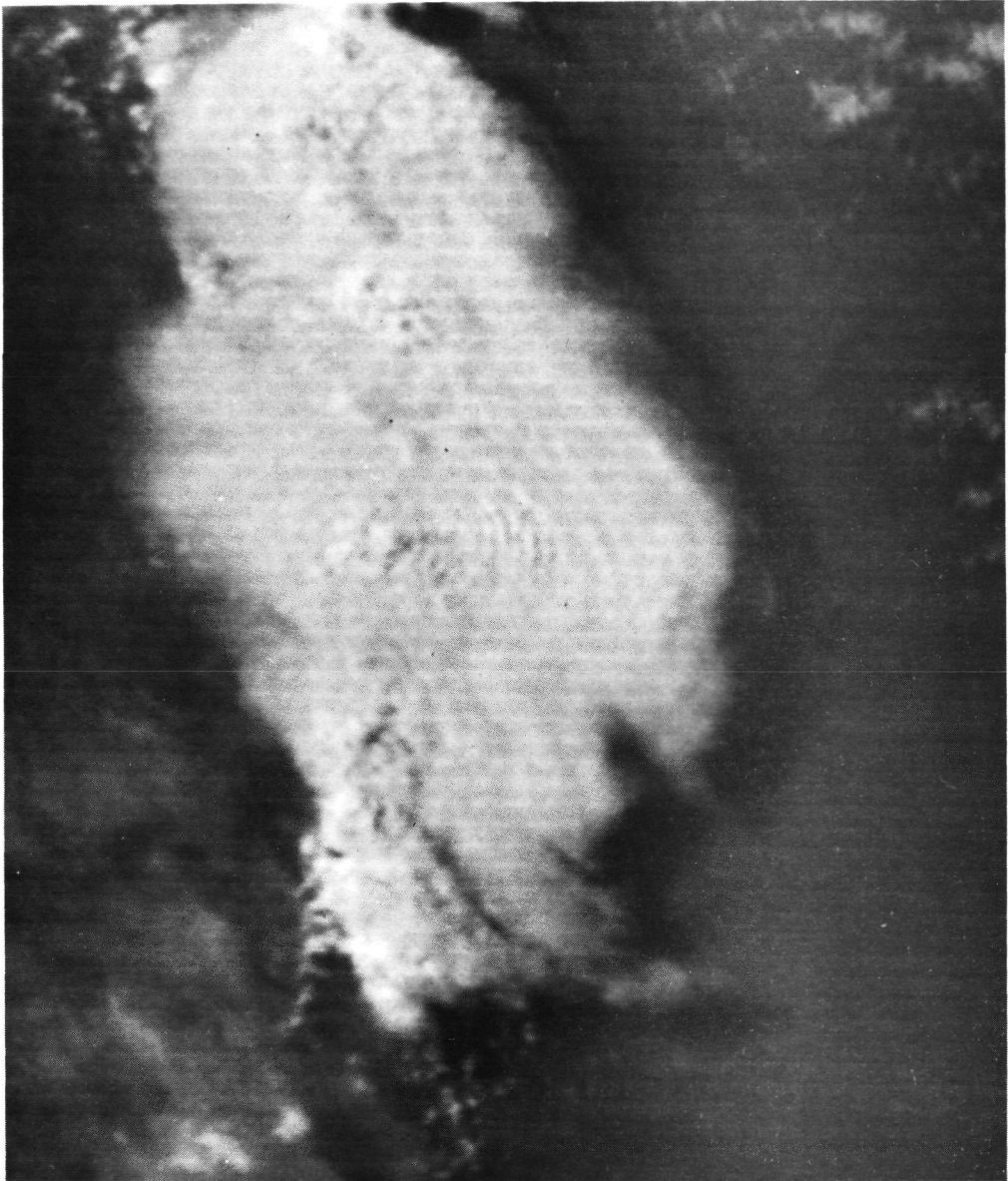


Figure 5.20. SMS-2 visual photograph taken over Kansas at 2348Z, June 18, 1975.



Figure 5.21. SMS-2 visual photograph taken over Kansas at 0002Z, June 19, 1975.

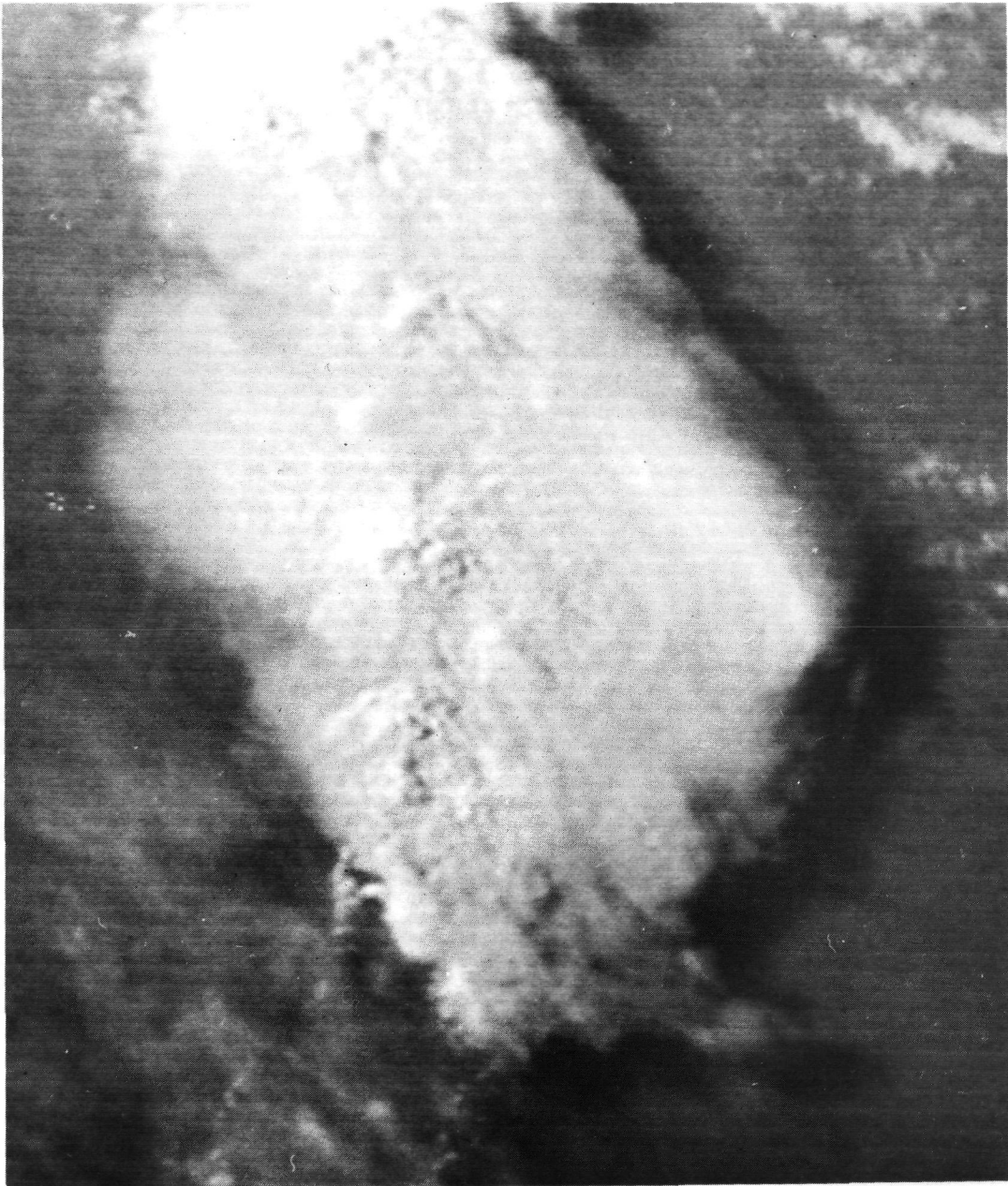


Figure 5.22. SMS-2 visual photograph taken over Kansas at 0017Z, June 19, 1975.



Figure 5.23. SMS-2 visual photograph taken over Kansas at 0032Z, June 19, 1975.

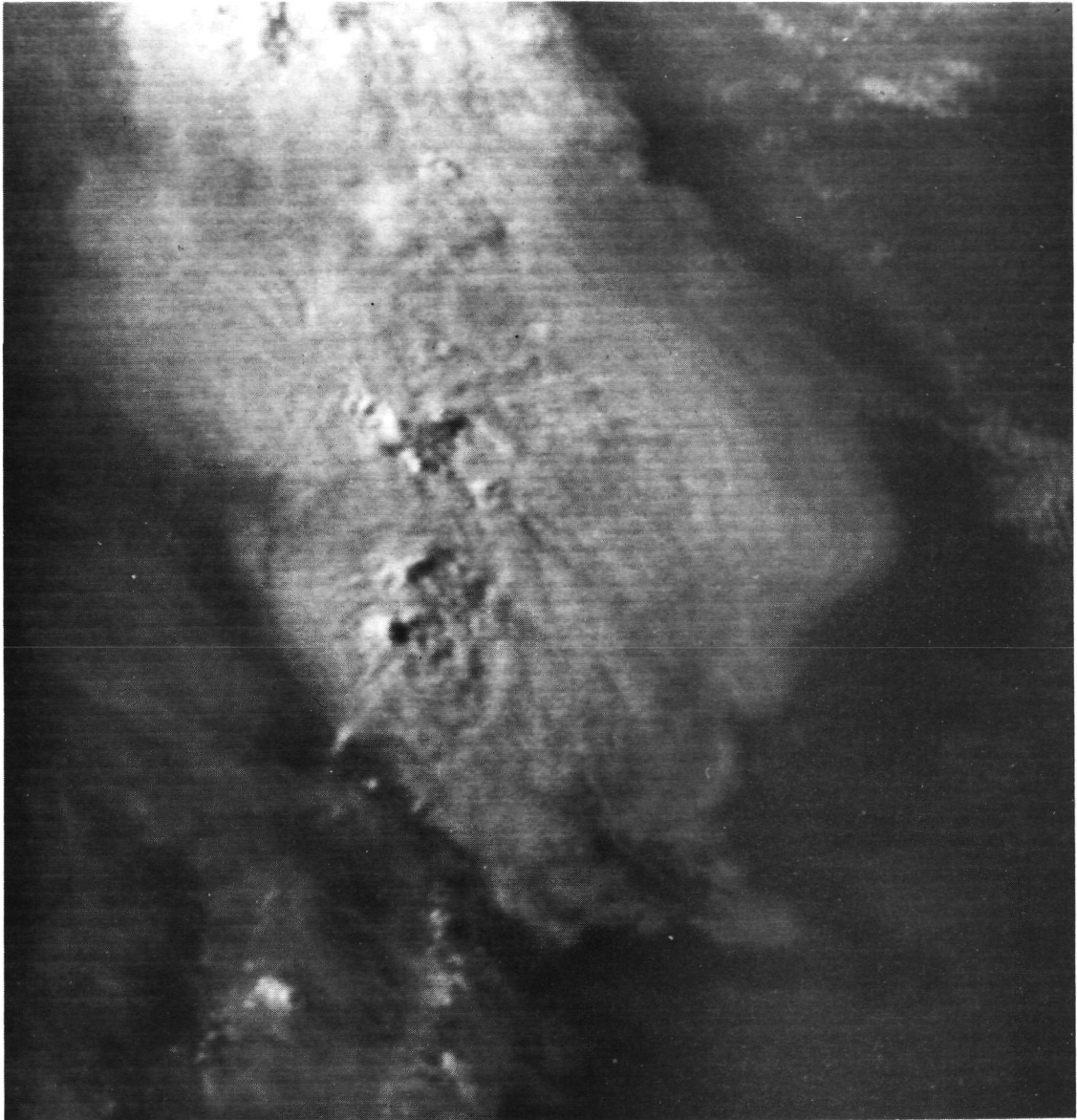


Figure 5.24. SMS-2 visual photograph taken over Kansas at 0047Z, June 19, 1975.

Table 5.3. Kansas Case Cloud Measurements

QUADRANT	TIME	WAVELENGTH (km)	AMPLITUDE (km)	RADIUS <sup>1</sup> (km)	OUTFLOW RATE <sup>2</sup> (m/sec)
East	2317Z	--	--	95	14
	2348Z	5	.5 - 1.2	120	17
	0002Z	--	--	135	17
	0017Z	--	--	150	17
	0032Z	--	--	165	17
	0047Z	--	--	180	17
	West	2317Z	--	--	65
2348Z		--	--	80	5.5
0002Z		--	--	85	11
0017Z		--	--	95	5.5
0032Z		--	--	100	5.5
0047Z		--	--	105	

<sup>1</sup> Measured relative to the dome which appears to be at the focus of the waves in Figure 5.19.

<sup>2</sup>  $(\Delta \text{ Radius}) \div (\Delta \text{ Time})$ .

(2) cirrus outflow created some degree of wind shear across the tropopause, (3) the dome's diameter is of the same scale as the wavelength, and (4) the waves occurred in the area of apparent maximum  $\Delta u_0$  across the tropopause.

Using the data in Table 5.4, equation (3.94) was solved. Figures 5.27 - 5.29 were constructed from these results. Again, the two humps in the  $\psi$  versus  $\lambda$  curves for constant  $\Delta u_0$  result in the two axes of maximum instability in Figure 5.29. Utilizing these two axes

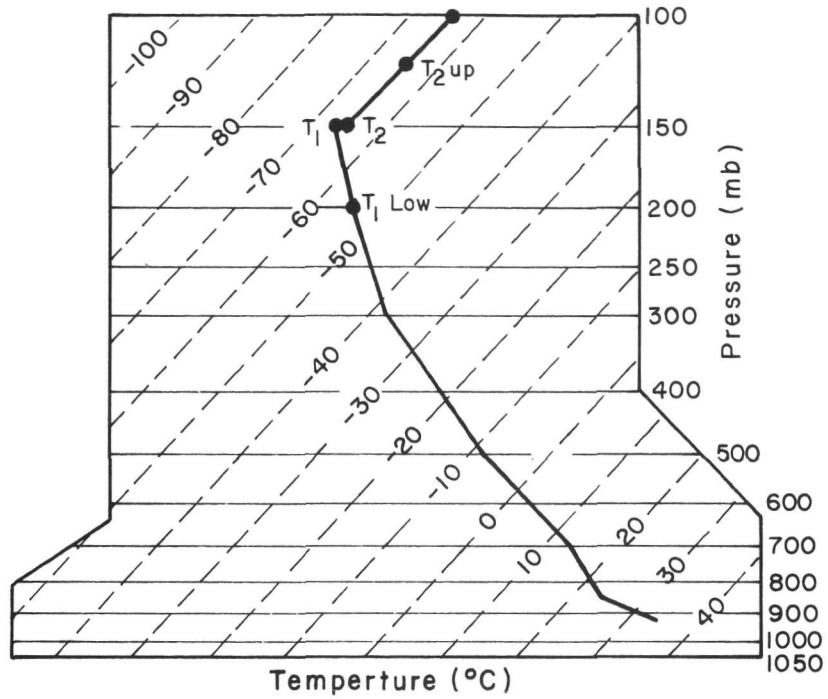


Figure 5.25. Temperature sounding from Dodge City, Kansas taken at 0000Z, June 19, 1975.

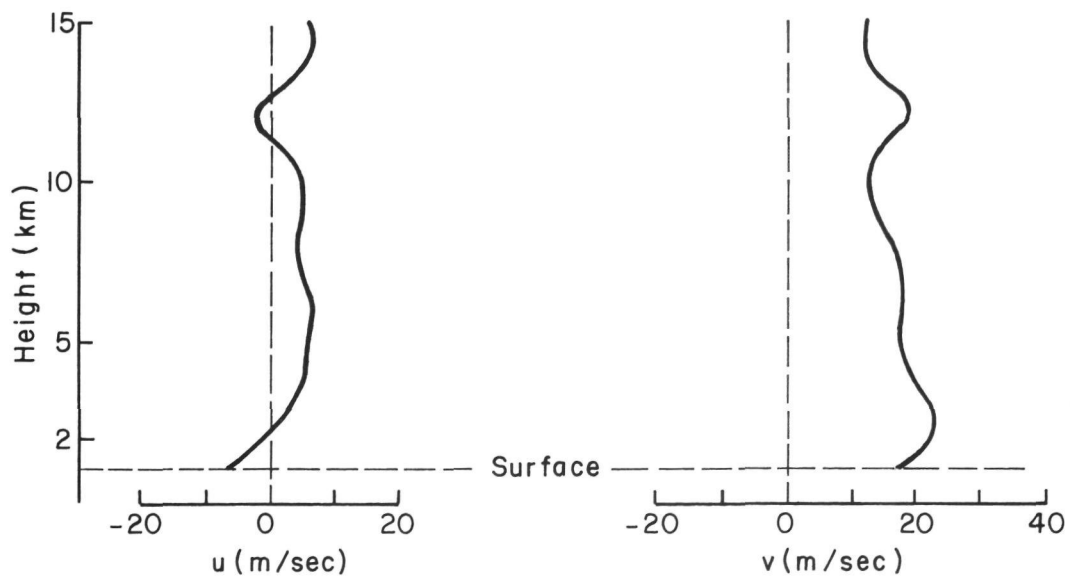


Figure 5.26. Wind profiles from Dodge City, Kansas sounding at 0000Z, June 19, 1975.

Table 5.4. Thermal Parameters for Kansas Case

$T_{2_{\text{up}}} = 209.0^{\circ}\text{K}$	$P_{2_{\text{up}}} = 125 \text{ mb}$		
$T_2 = 208.0^{\circ}\text{K}$	$P_2 = 150 \text{ mb}$	$\theta_2 = 357.9^{\circ}\text{K}$	$N_2^2 = 1.44 \times 10^{-4} \text{ sec}^{-1}$
$T_1 = 207.1^{\circ}\text{K}$	$P_1 = 154 \text{ mb}$	$\theta_1 = 353.6^{\circ}\text{K}$	$N_1^2 = 5.01 \times 10^{-4} \text{ sec}^{-1}$
$T_{1_{\text{low}}} = 217.9^{\circ}\text{K}$	$P_{1_{\text{low}}} = 200 \text{ mb}$		

one finds that 5 km is one of two most unstable wavelengths at  $\Delta u_0 = 13 \text{ m/sec}$  and  $\Delta u_0 = 25 \text{ m/sec}$ . This lower predicted value is again very close to the value of  $\Delta u_0$  (15 m/sec) calculated from the cloud motions and the sounding data.

When  $\Delta u_0 = 13 \text{ m/sec}$  on Figure 5.29, the lower axis of maximum instability predicts that  $\lambda \approx 2.3 \text{ km}$  will also be a relatively unstable wavelength. Again, the absence of visible waves of this wavelength may be due to their initially low amplitude relative to that of the 5 km wavelength waves.

Finally, the waves were no longer visible after 2348Z. This was in spite of the apparent increase of  $\Delta u_0$  to 17 m/sec throughout the next hour. Figure 5.29 would predict most unstable wavelengths of 6.5 km and 3.2 km for  $\Delta u_0 = 17 \text{ m/sec}$ . There are two possible rationalizations for the absence of visible waves during this hour. The first is that the surge of outflow that caused the waves was not evident at the cloud edge until later. This means that a lag may exist from the time a surge first occurs in the inner portions of the cloud to the time it appears at the cloud edge. In other words, the  $\Delta u_0$  in the area of the waves may have decreased already but this

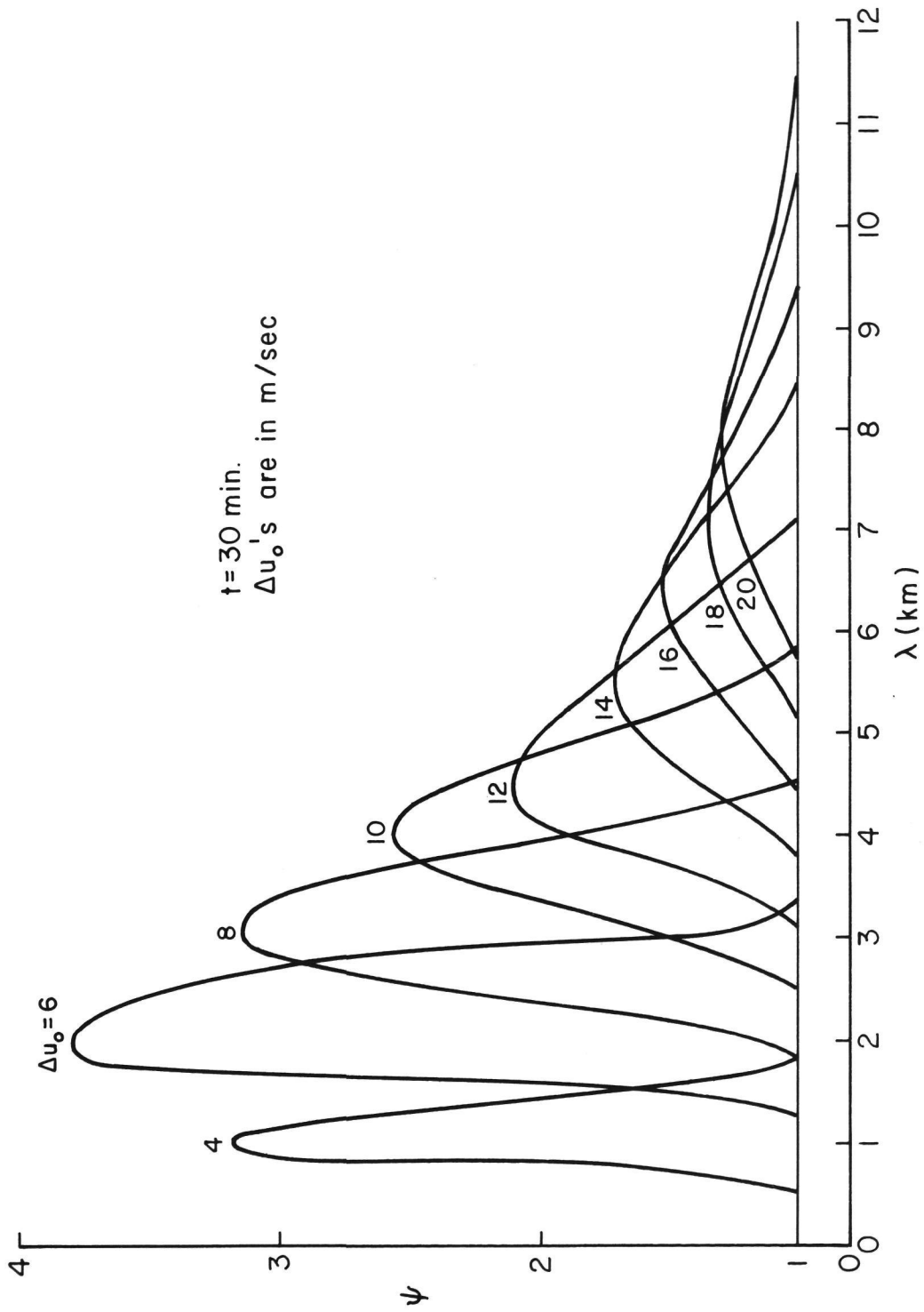


Figure 5.27. Right hump of  $\psi$  versus  $\lambda$  curves for selected  $\Delta u_0$ 's (Kansas case).

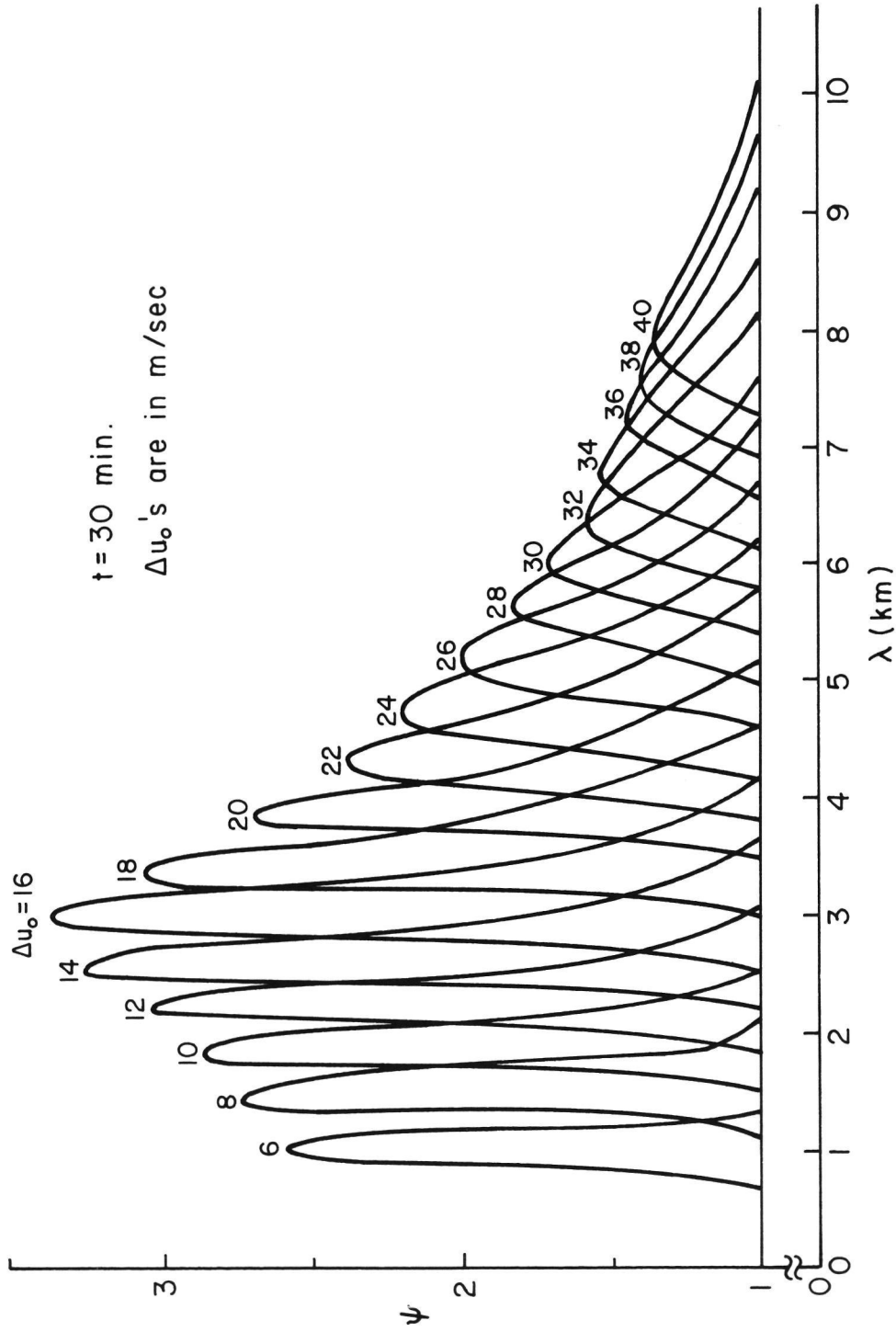


Figure 5.28. Left hump of  $\psi$  versus  $\lambda$  curves for selected  $\Delta u_0$ 's (Kansas case).

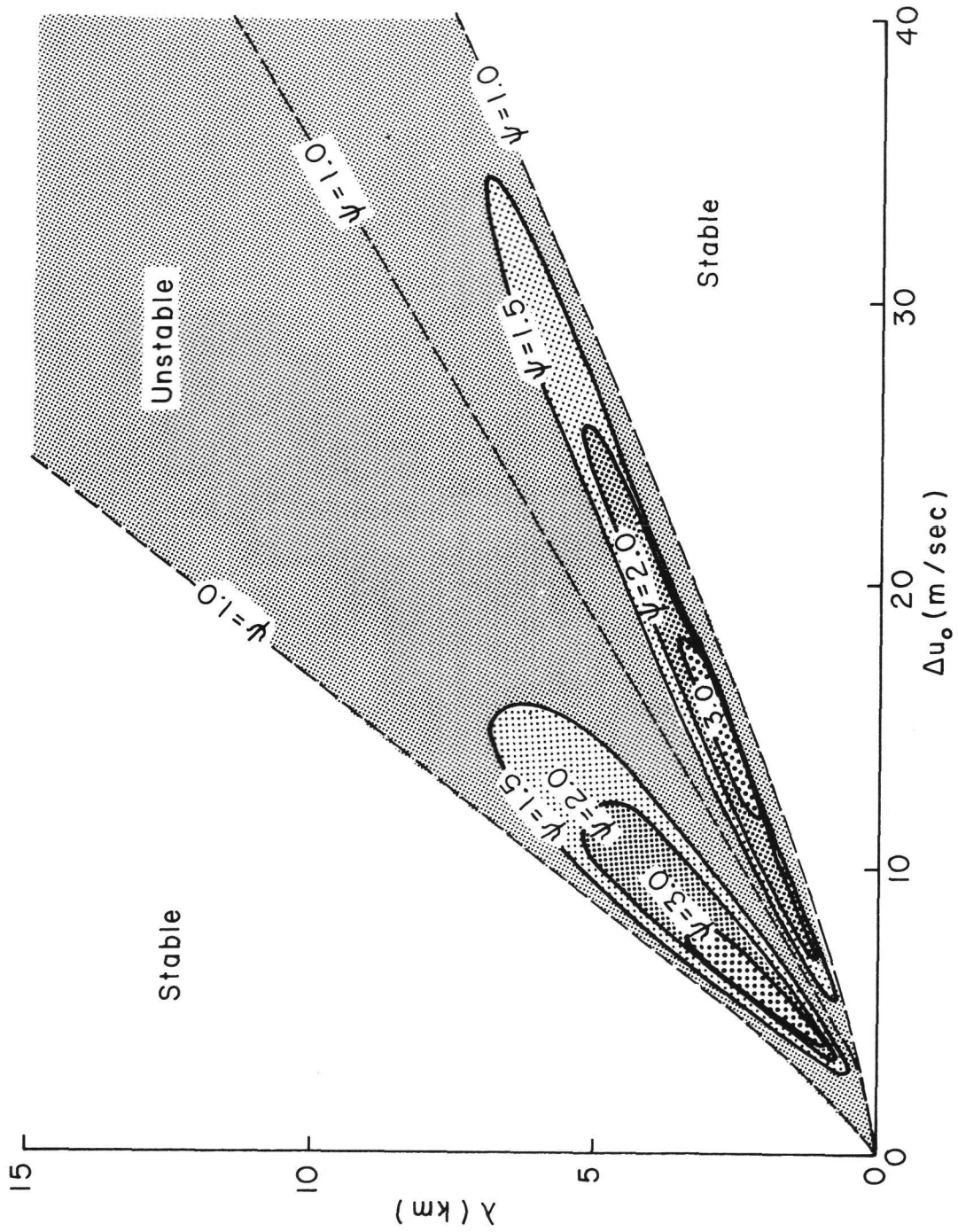


Figure 5.29.  $\Delta u_0$  versus  $\lambda$  curves for selected  $\psi$  at  $t = 30$  min (Kansas case).

will not be noticed at the cirrus edge until some time later. The second rationalization is that the initial amplitude of the other predicted wavelength waves was so small that the amplification has not yet been sufficient to make them visible in the satellite photographs.

### 5.3 Tropical Cases

As was mentioned earlier, concentric waves have occasionally been observed in DMSP photographs of tropical storms for several years. Three cases from the western Pacific are shown in Figures 5.30 - 5.32. These cases were selected from 156 visual DMSP photographs of Western Pacific tropical storms and typhoons. Of these 156 photographs, taken from June 1971 to January 1972, sixteen displayed some type of concentric wave pattern. The three cases discussed in this section were chosen because of their proximity to an upper air sounding at the time of the photograph. The data pertaining to these storms are summarized in Table 5.5. Since only one photograph exists for each case, cirrus outflow rates could not be computed. Table 5.6 summarizes the thermal parameters from the closest sounding to each storm.

The important features to be noted in the data for these cases are:

1. Only tropical storm "kit" had a sounding within 600 km of

Table 5.5. Observations from Tropical Cases

STORM NAME	TIME AND DATE OF PHOTOGRAPH	WAVELENGTH (km)	DISTANCE FROM CLOSEST SOUNDING
Gilda	2300Z June 24, 1971	5-6	950 km
Rose	2200Z August 12, 1971	4.5	650 km
Kit	2230Z January 4, 1972	3.5	less than 100 km

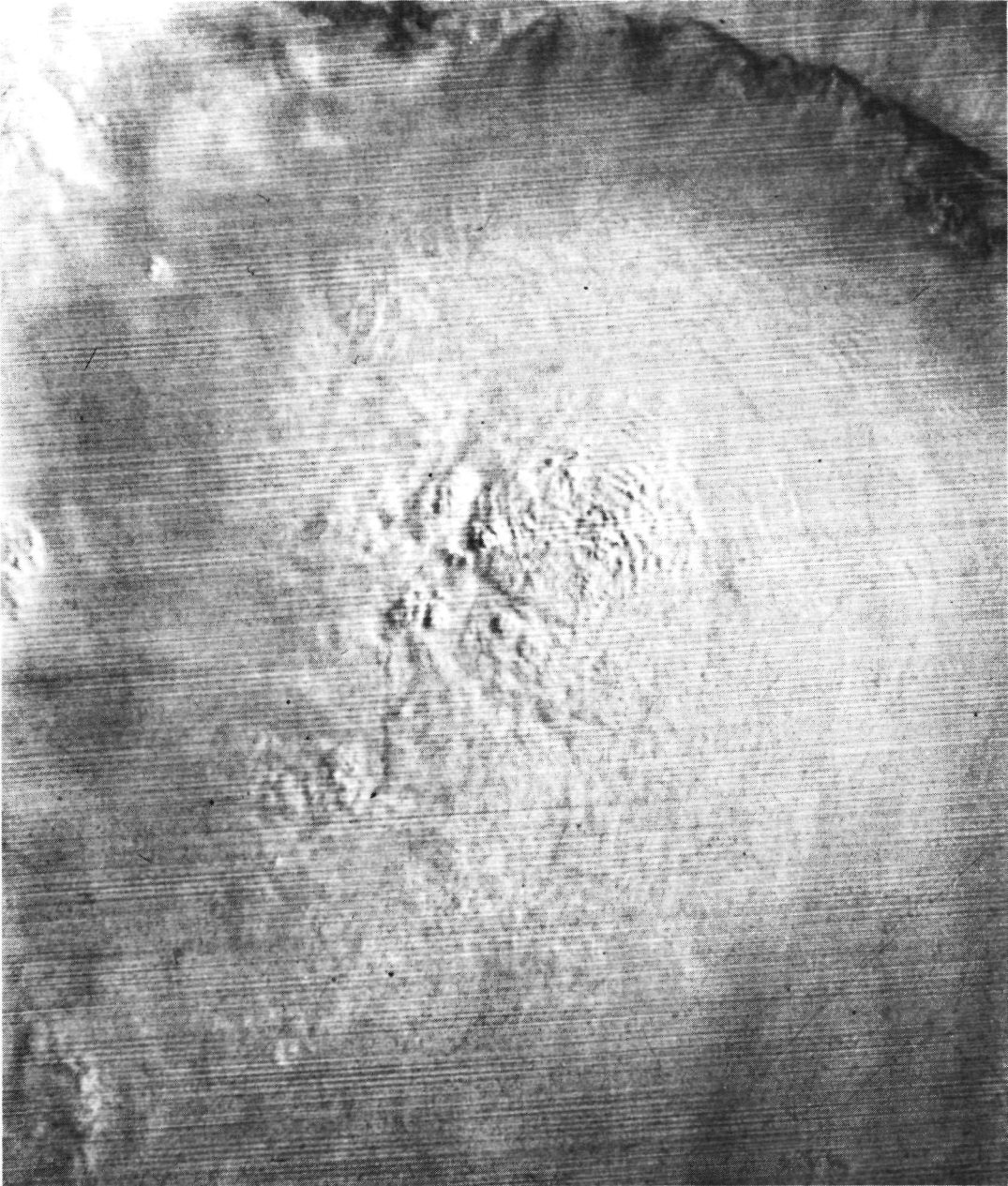


Figure 5.30. DMSP visual photograph of Typhoon Gilda taken at 2300Z, June 24, 1971.

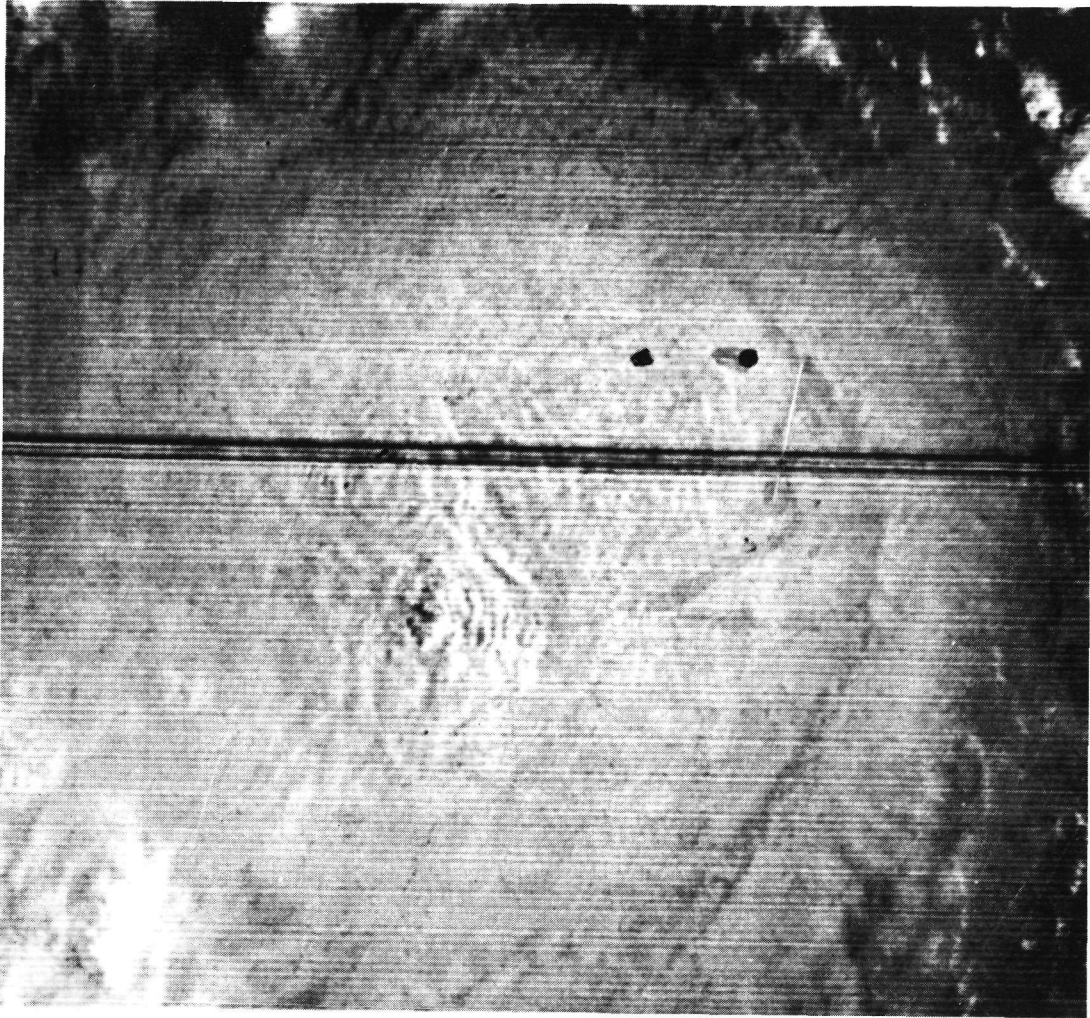


Figure 5.31. DMSP visual photograph of Typhoon Rose taken at 2200Z, August 12, 1971.

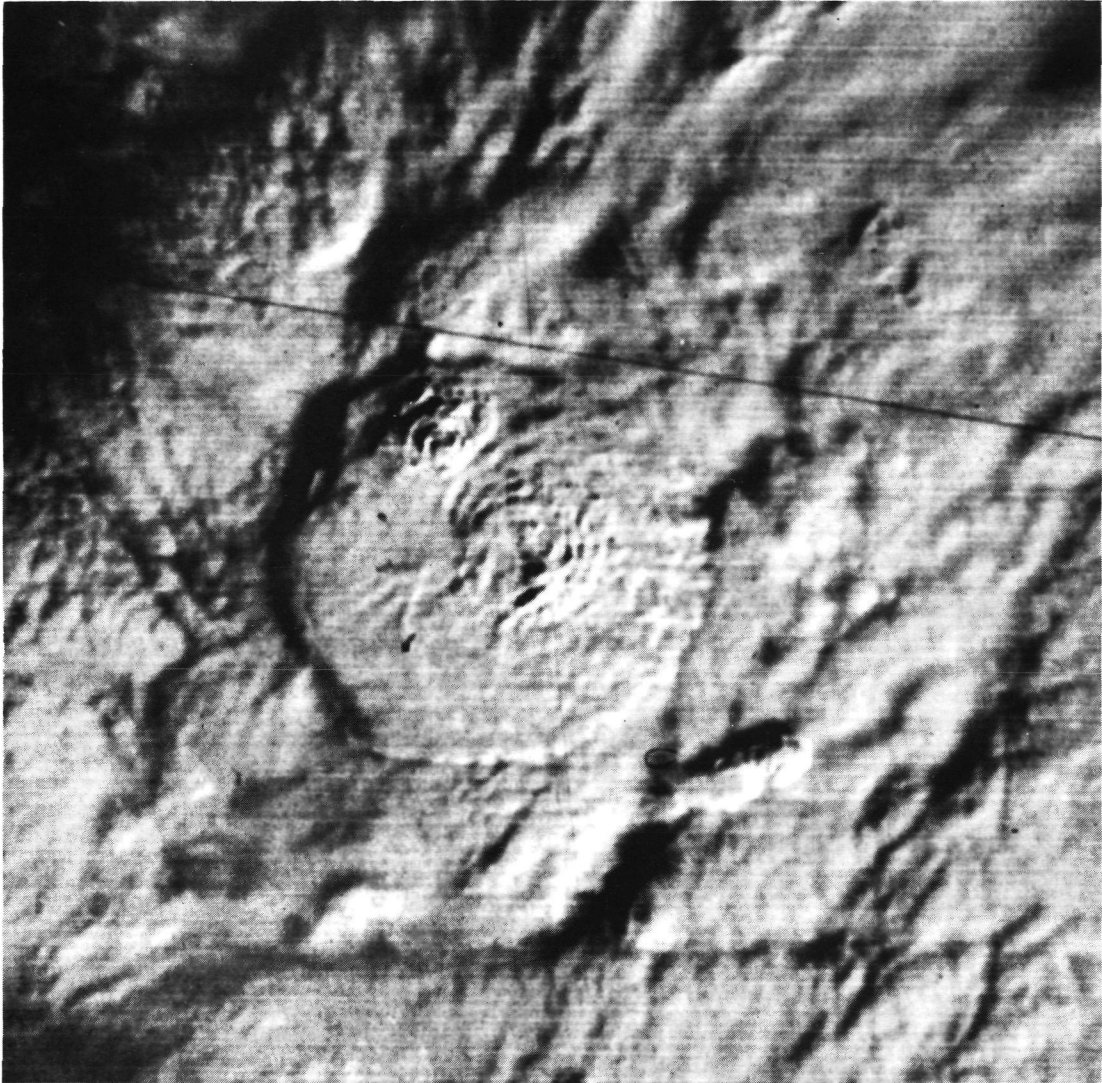


Figure 5.32. DMSP visual photograph of Typhoon Kit taken at 2230Z, January 4, 1972.

Table 5.6. Thermal Parameters for Tropical Cases

Gilda

$T_{2_{up}} = 191.9^{\circ}\text{K}$	$P_{2_{up}} = 100 \text{ mb}$		
$T_2 = 192.7^{\circ}\text{K}$	$P_2 = 112 \text{ mb}$	$\theta_2 = 370.7^{\circ}\text{K}$	$N_2^2 = 4.99 \times 10^{-4} \text{ sec}^{-1}$
$T_1 = 203.1^{\circ}\text{K}$	$P_1 = 150 \text{ mb}$	$\theta_1 = 360.4^{\circ}\text{K}$	$N_1^2 = 1.79 \times 10^{-4} \text{ sec}^{-1}$
$T_{1_{low}} = 218.5^{\circ}\text{K}$	$P_{1_{low}} = 200 \text{ mb}$		

Rose

$T_{2_{up}} = 194.7^{\circ}\text{K}$	$P_{2_{up}} = 100 \text{ mb}$		
$T_2 = 193.9^{\circ}\text{K}$	$P_2 = 104 \text{ mb}$	$\theta_2 = 376.2^{\circ}\text{K}$	$N_2^2 = 4.9 \times 10^{-4} \text{ sec}^{-1}$
$T_1 = 203.9^{\circ}\text{K}$	$P_1 = 150 \text{ mb}$	$\theta_1 = 370.4^{\circ}\text{K}$	$N_1^2 = 2.5 \times 10^{-4} \text{ sec}^{-1}$
$T_{1_{low}} = 219.5^{\circ}\text{K}$	$P_{1_{low}} = 200 \text{ mb}$		

Kit

$T_{2_{up}} = 185.9^{\circ}\text{K}^*$	$P_{2_{up}} = 80 \text{ mb}^*$		
$T_2 = 185.9^{\circ}\text{K}$	$P_2 = 100 \text{ mb}$	$\theta_2 = 359.2^{\circ}\text{K}$	$N_2^2 = 5.15 \times 10^{-4} \text{ sec}^{-1}$
$T_1 = 204.9^{\circ}\text{K}$	$P_1 = 150 \text{ mb}$	$\theta_1 = 355.5^{\circ}\text{K}$	$N_1^2 = 3.5 \times 10^{-5} \text{ sec}^{-1}$
$T_{1_{low}} = 219.7^{\circ}\text{K}$	$P_{1_{low}} = 200 \text{ mb}$		

\*Estimated values. The sounding ended at 100 mb yet did not report a tropopause.

its center. This sounding, however, did not report a tropopause. It too then, is not a very reliable source for the thermal parameters used in equation (3.94).

2. No measurements of  $\Delta u_0$  across the tropopause in each storm were available.

In spite of these shortcomings, there is still evidence that (1) the focus of the waves in each photograph is characterized by penetrative convection and (2) the intense cirrus outflow would result in some wind shear near the tropopause in each case.

Figures 5.33 - 5.35 contain graphs of the stability regimes calculated for each of these cases. In spite of the poor data base for each of the curves, they do display features consistent with the mid-latitude cases. First of all, the lower values for  $\Delta u_0$  for which each observed wavelength is one of two most unstable wavelengths, are quite close to those observed in the mid-latitude cases. Specifically, these values range from  $\Delta u_0 = 10$  m/sec for Tropical Storm Rose to  $\Delta u_0 = 15$  m/sec for Tropical Storm Gilda. The curve for Tropical Storm Kit predicts  $\lambda = 3.5$  km (observed wavelength) to be one of two most unstable wavelengths at  $\Delta u_0 = 11$  m/sec.

The magnitude of  $\psi$ , predicted in each of these cases, however, varies considerably from case to case. For Tropical Storm Kit  $\psi = 1.035$  when the observed wavelength is one of two predicted most unstable wavelengths. For Tropical Storm Rose, this value jumps to  $\psi = 16$  where the observed wavelength is one of two most unstable. This large difference in  $\psi$  from case to case is probably a result of errant data. As will be shown in section 6.0, the magnitude of  $\psi$  is very sensitive to data errors.

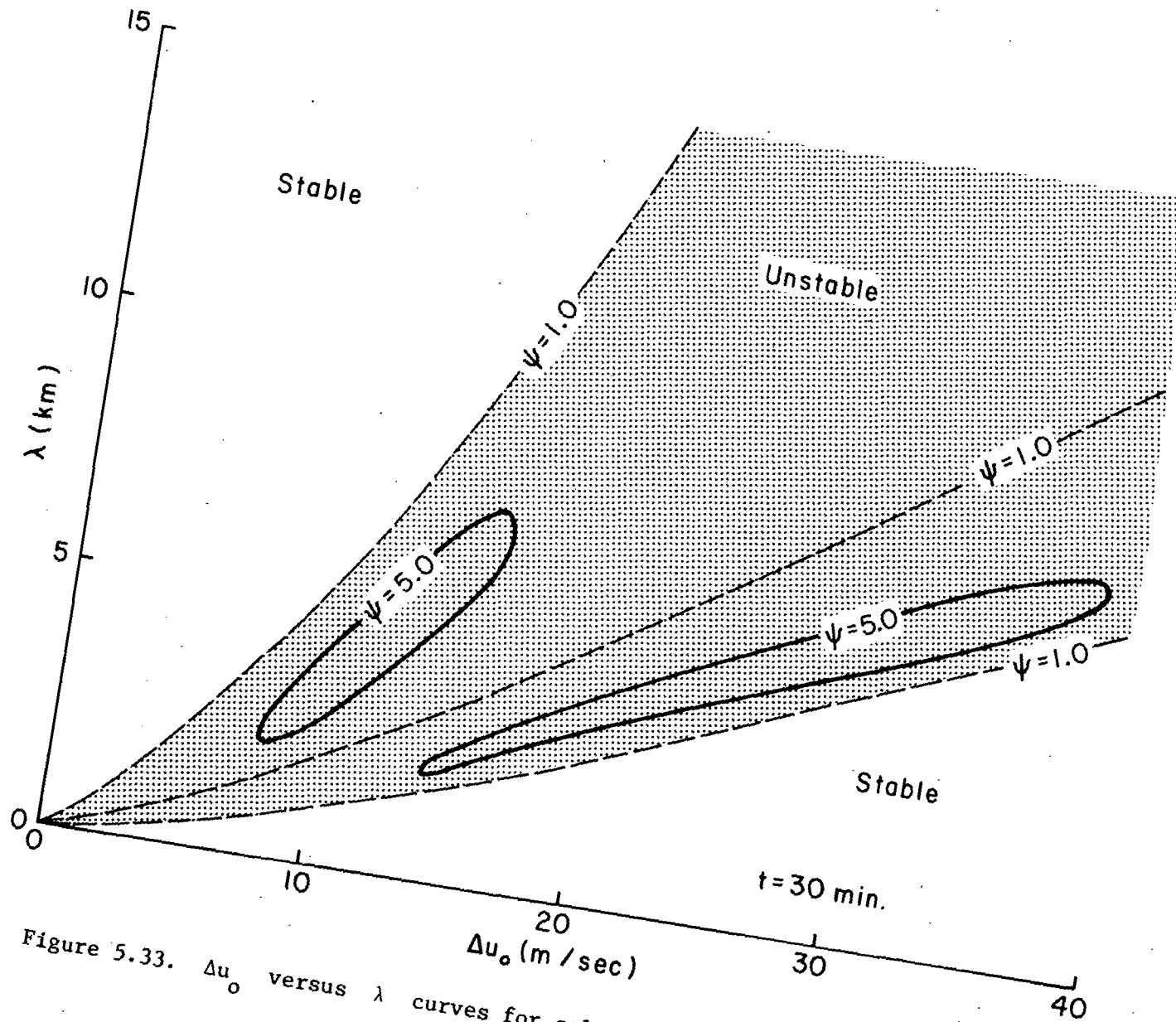


Figure 5.33.  $\Delta u_0$  versus  $\lambda$  curves for selected  $\psi$  at  $t = 30$  min (Typhoon Gilda).

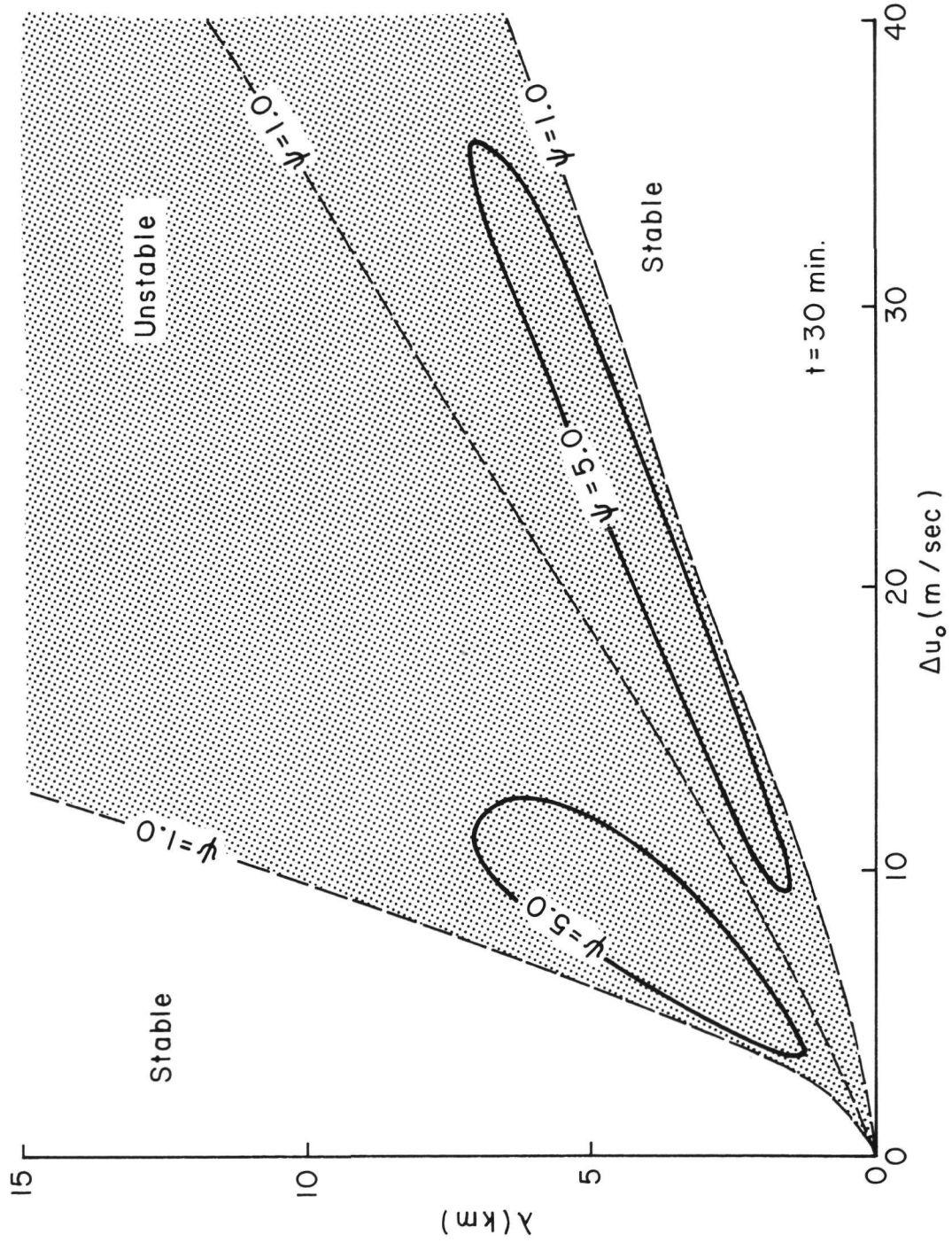


Figure 5.34.  $\Delta u_0$  versus  $\lambda$  curves for selected  $\psi$  at  $t = 30$  min (Typhoon Rose).

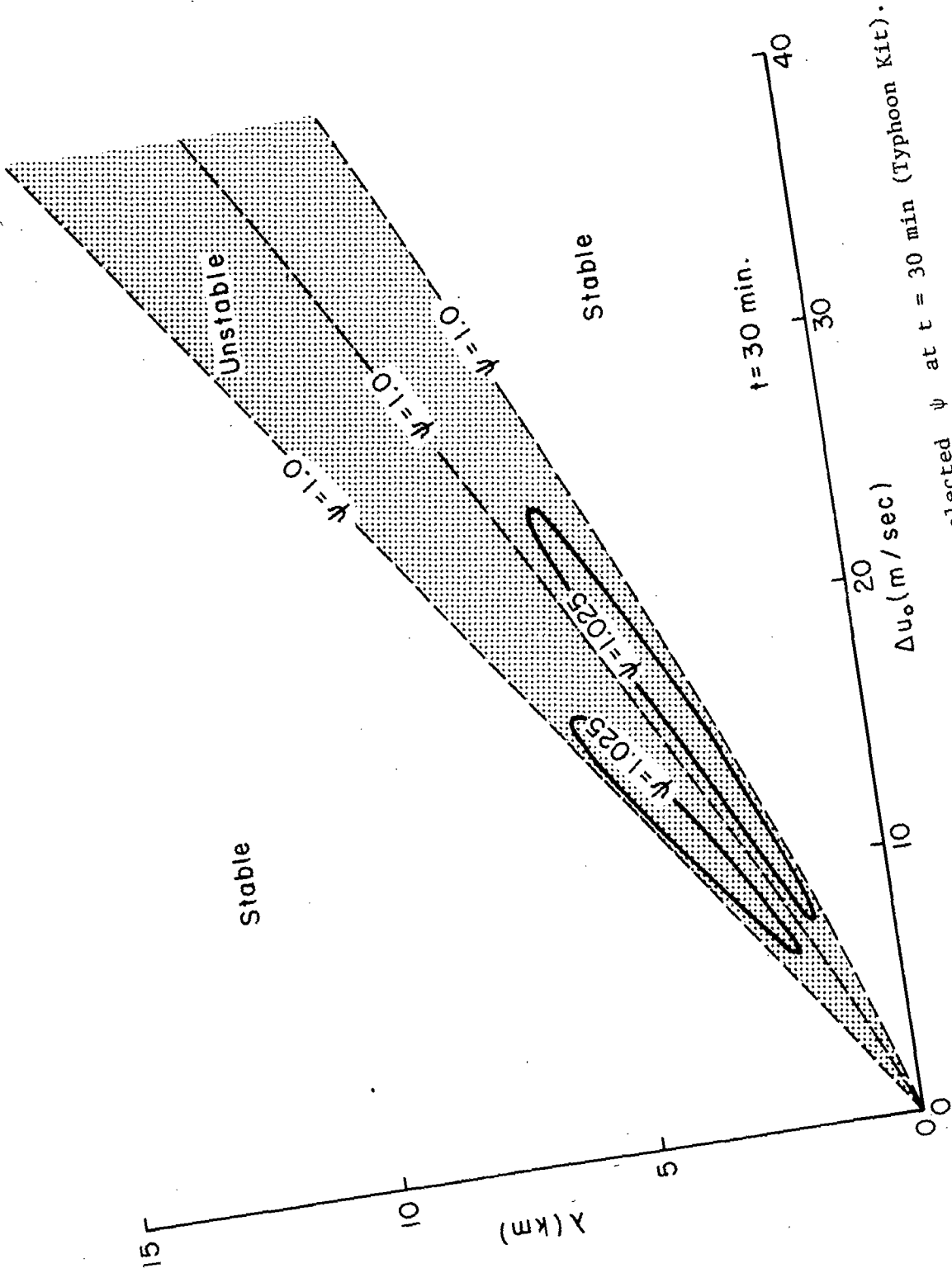


Figure 5.35.  $\Delta u_0$  versus  $\lambda$  curves for selected  $\psi$  at  $t = 30$  min (Typhoon Kit).

Unfortunately, the predicted values of  $\Delta u_0$  in each case cannot be verified by observations. However, the mere fact that they are so close to those observed in the mid-latitude cases lends credence to the stability model.

## 6. ERROR ANALYSIS

### 6.1 Measurement Errors

The data presented in this paper is, for the most part, subject to a great deal of uncertainty. This is especially true of the sounding data in the tropical cases. Even in the mid-latitude cases, the soundings were taken outside the area of visible wave activity. For this reason, a proposed range of expected values would be more or less a guess. Also, the distance measurements made on the satellite photographs are subject to error. These distance errors become even more significant when calculating amplitudes based on shadow lengths (see Appendix A). Rather than performing an arbitrary error analysis of each case study, we will use the Nebraska case data to demonstrate the sensitivity of the stability model to a selected amount of error. The Nebraska case was chosen because of its apparently superior data. We will also discuss amplitude errors resulting from inaccurate measurements and the perhaps invalid assumptions inherent in equation (A.9).

In the case of errors for the stability model, we will choose an error range of  $\pm 1^\circ\text{C}$  for each temperature measurement,  $T_{1_{\text{low}}}$ ,  $T_1$ ,  $T_2$ , and  $T_{2_{\text{up}}}$ . It can be shown that the stability characteristics would be effected most if these errors were combined in the following two ways:

Error set #1

$$T_{2_{\text{up}}}^{\prime} = T_{2_{\text{up}}} + 1^\circ\text{C}$$

$$T_2^{\prime} = T_2 - 1^\circ\text{C}$$

$$T_1^{\prime} = T_1 - 1^\circ\text{C}$$

$$T_{1_{\text{low}}}^{\prime} = T_{1_{\text{low}}} + 1^\circ\text{C}$$

Error set #2

$$T_{2_{\text{up}}}^{\prime\prime} = T_{2_{\text{up}}} - 1^\circ\text{C}$$

$$T_2^{\prime\prime} = T_2 + 1^\circ\text{C}$$

$$T_1^{\prime\prime} = T_1 + 1^\circ\text{C}$$

$$T_{1_{\text{low}}}^{\prime\prime} = T_{1_{\text{low}}} - 1^\circ\text{C}$$

Error sets #1 and #2 applied to the Nebraska case at  $\lambda = 11 \text{ km}$  and  $t = 30 \text{ min}$  result in curves #1 and #2 respectively in Figure 6.1. Obviously, the amplitude of  $\psi$  for this case is greatly affected by these errors. The values of  $\Delta u_0$  for maximum  $\psi$ , however, are not changed so drastically. For the lower hump in Figure 6.1, maximum  $\psi$  is found at  $\Delta u_0 = 14 \text{ m/sec}$  in curve #2 and at  $\Delta u_0 = 25 \text{ m/sec}$  in curve #1. These values are still within the range of possible values in section 5.1. The upper hump shows that the maximum  $\psi$  is found at nearly the same value of  $\Delta u_0$  for both cases. The conclusion from this is that the ranges of  $\Delta u_0$  for which a given wavelength will be unstable can be reasonably predicted using conventional data in the model. However, the degree of instability is far too sensitive to observational errors to permit accurate calculations of amplitude growth rates.

The most serious amplitude errors are probably a result of the assumptions which are implied in equation (A.9). Some of the suspected error producing assumptions are:

1. The cirrus top is smooth except for the wave pattern.  
(Figure 1.2 shows that this is not necessarily the case.)
2. The wave pattern is a sine wave.
3. There is no refraction or diffraction of the sun's rays.
4. The cloud's surface is totally opaque to the sun's visible radiation.

The seriousness of these assumptions, however, cannot be accurately evaluated without a case which compares calculated values to direct amplitude measurements. The effects of measurement errors, regardless of these assumptions, are shown by the range of amplitudes given in

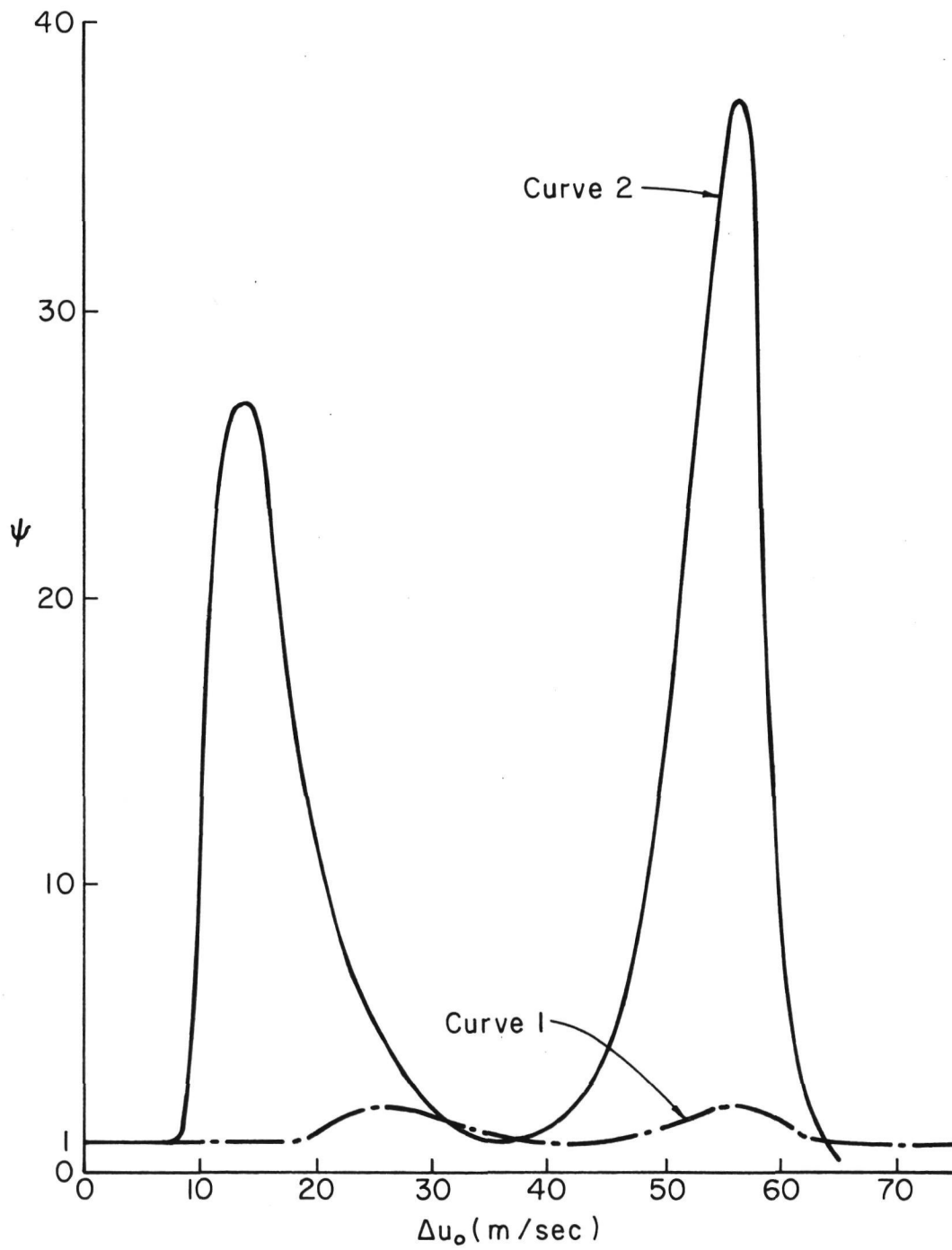


Figure 6.1. Error curves of  $\psi$  versus  $\Delta u_0$  for Nebraska case at  $t = 30$  min and  $\lambda = 11$  km.

Tables 5.1 and 5.3. These ranges were produced by assuming measurement errors of  $\pm 1$  km for both wavelength and shadow length. Obviously, only an order of magnitude estimate of amplitude is possible with these data.

## 6.2 Stability Model Errors

There were a multitude of assumptions made in the derivation of equation (3.94). Rather than attempting to evaluate each of these, we will look at the one assumption that separates this model from the incompressible model. That assumption is that  $\rho_o$  is an exponential function of height rather than a constant. This is expressed in the following equation:

$$\rho_o = e^{-\delta z} \rho_s$$

Let us now see how this reduces the error in the lower layer of the Nebraska case. First, for the incompressible case,  $\rho_o$  for the entire layer is estimated by  $\rho_o$  at the tropopause, (153 mb). Using the equation of state, this  $\rho_o$  is calculated to be  $.258 \text{ kg/m}^2$ . If we now go down approximately 2 km to 200 mb,  $\rho_o$  becomes  $.324 \text{ kg/m}^2$ . Thus the error introduced at this level is 20 percent. On the other hand, the exponential model results in virtually no error in  $\rho_o$  at this level, assuming  $\delta = 1.23 \times 10^{-4} \text{ m}^{-1}$  in the lower layer. Slight errors will be introduced as lapse rates change in each layer, but these errors are negligible compared to those introduced by the incompressibility assumption.

Before concluding our discussion of the errors in the stability model, we should mention one apparent inconsistency. This inconsistency occurs in the area of  $\beta_1 = \pm \infty$ , which results at  $c = u_{o_1}$ . This is

similar to the infinity resulting at the critical level of other gravity wave models. Its physical significance is still in question at this point.

## 7. SUMMARY AND CONCLUSIONS

This report has examined concentric wave phenomena atop the cirrus level of intense convective storms. These waves appear in satellite photographs of both mid-latitude and tropical storms. They are usually centered about an area of deep penetrative convection.

A model for the generation and growth of these waves was derived. This model proposes that the rapid penetration of the tropopause by overshooting convection initially generates the waves. Once generated, the waves are then further amplified by shearing instability. The instability equation was derived by perturbation techniques similar to those used to derive the Helmholtz equation. Incompressibility, however, was not assumed.

The approach used in creating the model for these waves had two basic steps. The first step was to determine which features occur in all of the cases observed. These included penetrative convection, intense cirrus outflow, and a cirrus cloud top location near the tropopause. Utilizing these characteristics, a model containing these same features was developed. Once developed, the results of the model were then tested for consistency with respect to the observed conditions for each case.

Two mid-latitude and three tropical cases were analyzed. The mid-latitude cases were observed from SMS-2, and thus several short time interval photographs were available. This, along with supporting radar and upper air data permitted calculations of the relative cirrus outflow rates which could then be used to approximate values for the wind shear across the tropopause. These calculated values were then compared to those predicted by the stability model. In this manner,

the validity of the model in the mid-latitude cases was evaluated quantitatively.

The tropical cases, on the other hand, contained only one photograph of each case. Thus, values for the wind shear across the tropopause could not be calculated. Therefore, only a qualitative evaluation of the stability model was made in the tropical cases.

The results from the case studies led to the following conclusions:

1. These concentric waves are initially the result of a rapid penetration of the tropopause by a deep convective storm.
2. The cirrus outflow from the storm creates a wind shear across the tropopause.
3. This wind shear is responsible for further wave growth due to shearing instability.

Any conclusions regarding the validity of the wave stability model are relatively premature at this point. However, there are several distinct characteristics of the model that do warrant consideration:

1. Incompressibility is not assumed and thus, errors created by this assumption in the Helmholtz equation are greatly reduced.
2. The results of the model predict only a certain range of unstable wavelengths for a given wind shear across the tropopause. This is unlike the incompressible Helmholtz model which predicts increasing instability for all wavelengths shorter than the "critical wavelength." It would appear from observations, that the former results better describe atmospheric gravity shear wave phenomena.

3. The range of solutions obtained from the stability model in the case studies agrees favorably with observations, even when the data may be subject to substantial errors.

This paper presents only a "first guess" as to the cause of these waves. In light of current observational data, it is an entirely feasible explanation. Only further study with more direct measurements of environmental conditions and wave motions can verify or disprove the model conclusively.

## 8. SUGGESTIONS FOR FURTHER STUDY

Obviously, a great deal of further testing of the stability model is needed before its true validity can be determined. In particular, better sounding data within the area of wave activity is needed. Also time lapse photographs would greatly aid in the verification of predicted phase speeds.

Another important study of these waves would be a statistical analysis of their relationship to severe weather occurrences. This would require a much larger and more random sample than that presented in this paper. However, the few cases analyzed so far do show encouraging signs of some type of correlation.

Finally, if the stability model is, in fact, valid, there is a possibility that these wave patterns could be used to deduce storm motions. This would be done by determining the storm motion necessary to create the observed wave pattern. Of course, temperature and wind profiles of the storm area would be necessary to make such a calculation. Still, it is possible that even composite-type values of these parameters would be sufficient to deduce at least a direction of movement, and maybe even a range of possible speeds.

## REFERENCES

- Anderson, Charles E. and Louis W. Uccellini, 1973: Studies of meteorological factors involved in the formation of severe local storms in the northeast Colorado region. Eighth Conf. on Severe Local Storms, Boston, MA., Oct.
- Arn, Robert M., 1975: Anvil area and brightness characteristics as seen from geosynchronous satellites. Masters thesis. Colorado State Univ., Dept. of Atmos. Sci., Fort Collins.
- Arnold, Charles P., 1975: A study of satellite observed Helmholtz waves within a tropical cyclone canopy. Unpublished report. Colorado State Univ., Dept. of Atmos. Sci., Fort Collins.
- Auvine, B. and C. E. Anderson, 1972: The use of cumulonimbus anvil growth data for inferences about the circulation in thunderstorms and severe local storms. Tellus, 24, 4.
- Brandli, C. O. and F. A. Lombardo, 1974: High level wave clouds not associated with terrain (billows). Bull. Amer. Met. Soc., 55, 11.
- Drazin, P. G. and L. N. Howard, 1966: Hydrodynamic stability of parallel flow of inviscid fluid. Adv. Appl. Mech., 9, 1.
- Einaudi, F. and D. P. Lalas, 1974: Some new properties of Kelvin-Helmholtz waves in an atmosphere with and without condensation effects. J. Atmos. Sci., 31, Nov.
- Erickson, Carl O. and L. F. Whitney, Jr., 1973: Gravity waves following severe thunderstorms. Mon. Wea. Rev., 101, 9.
- Ernst, John A., 1975: New synchronous meteorological satellite, SMS-2. Weatherwise, 28, 4.
- Fujita, T. T., 1972: Tornado occurrences related to overshooting cloud-top heights as determined from ATS pictures. SMRP research paper No. 97, Dept. of Geophysical Sciences, Univ. of Chicago, April.
- Fujita, T. T., 1973: Proposed mechanism of tornado formation from rotating thunderstorms. Eighth Conf. on Severe Local Storms, Boston, MA., Oct.
- Fujita, T. T., 1974: Overshooting thunderheads observed from ATS and Learjet. SMRP research paper No. 117, Dept. of Geophysical Sciences, Univ. of Chicago, Jan.
- Gossard, E. E. and W. H. Munk, 1954: On gravity waves in the atmosphere. J. Meteorol., 11, 4.

- Gossard, E. E. and William H. Hooke, 1975: Waves in the Atmosphere, Atmospheric Infrasound and Gravity Waves - Their Generation and Propagation. Elsevier Scientific Publishing Co., New York.
- Haltiner, G. J., 1971: Numerical Weather Prediction. John Wiley and Sons, Inc., New York.
- Haltiner, G. J. and F. L. Martin, 1957: Dynamical and Physical Meteorology. McGraw-Hill Book Co., New York.
- Haurwitz, B., 1941: Dynamic Meteorology. McGraw-Hill Book Co., New York.
- Hines, C. O., 1968: Some consequences of gravity-wave critical layers in the upper atmosphere. J. Atmos. Terr. Phys., 30, 5.
- Howard, L. N. and S. A. Maslowe, 1973: Stability of Stratified shear flows. Boundary Layer Meteorol., 4, 5.
- International Mathematical and Statistical Library Reference Manual. IMSL Inc., 1971.
- Kreyszig, Erwin, 1968: Advanced Engineering Mathematics. John Wiley and Sons, Inc., New York.
- Lee, J. T., 1971: Aerial survey of tornado-producing thunderstorms. Seventh Conf. on Severe Local Storms, Kansas City, MO., Oct.
- Miles, John W., 1961: On the stability of heterogeneous shear flows. J. Fluid Mech., 10, 4.
- Miller, J., 1975: Some empirical rules to follow when applying satellite data to severe weather situations. Unpublished report. Satellite Field Service Station, Kansas City, MO.
- Miller, Robert C., 1972: Notes on analysis and severe storm forecasting procedures of the Air Force Global Weather Central. Technical Report 200 (Rev), Air Weather Service Publication.
- Pierson, Willard J. Jr., Gerhard Neuman, and Richard W. James, 1971: Practical Methods for Observing and Forecasting Ocean Waves by Means of Wave Spectra Statistics. U.S. Naval Oceanographic Office, Washington, D.C.
- Purdom, James F. W., 1971: Satellite imagery and severe weather warnings. Seventh Conf. on Severe Local Storms, Kansas City, MO., Oct.
- Purdom, James F. W., 1973: Satellite imagery and the mesoscale convective forecast problem. Eighth Conf. on Severe Local Storms, Boston, MA., Oct.
- Purdom, James F. W., 1974: Satellite imagery applied to the mesoscale surface analysis and forecast. Fifth Conf. on Weather Forecasting and Analysis, St. Louis, MO., Mar.

- Roach, W. T., 1967: On the nature of the summit areas of severe storms in Oklahoma. Q.J.R. Meteor. Soc., 93, Jul.
- Shenk, William E., 1974: Cloud top height variability of strong convective cells. J. Appl. Meteor., 13, Dec.
- Smith, Arthur H. Jr., 1974: What are you looking at when you say this area is suspect area for severe weather. NOAA Technical Manual NESS 56, NOAA Publication.
- Uccellini, Louis W., 1975: A case study of apparent gravity wave initiation of severe convective storms. Mon. Wea. Rev., 103, 6.
- United States Naval Observatory, 1975: The Air Almanac. U.S. Navy Publication.
- Waco, David E., 1970: Temperature and turbulence at tropopause levels over hurricane Beulah (1967). Mon. Wea. Rev., 98, 10.

## APPENDIX A

## AMPLITUDE MEASUREMENT TECHNIQUE

Figure A.1 contains a cross-sectional view of an idealized wave pattern. Figure A.2 contains an overhead view of this same pattern. This idealized picture is used to derive a method for inferring amplitude based on the shadow length in each wave.

In Figure A.1 and A.2, the following parameters can be measured or obtained from solar tables, if the time and date of the photograph are known:

$x_s$	length of the shaded portion of the wave
$x_c$	length of the bright portion of the wave
$\lambda$	wavelength
$a$	$90^\circ - (\text{sun zenith angle})$
$b$	$90^\circ - (\text{sun elevation angle})$

In Figure A.2, we note that the wavelength as seen from the sun is  $\lambda'$ . This can be calculated by using:

$$\lambda' = \frac{\lambda}{\cos b}$$

Now, assuming that the sun's rays are straight parallel lines, we may write the equation for the ray passing through A and B as:

$$z = mx + z_3 \tag{A.1}$$

Where:

$$m = \text{slope of line AB}$$

Also the wave equation, as seen from the sun is:

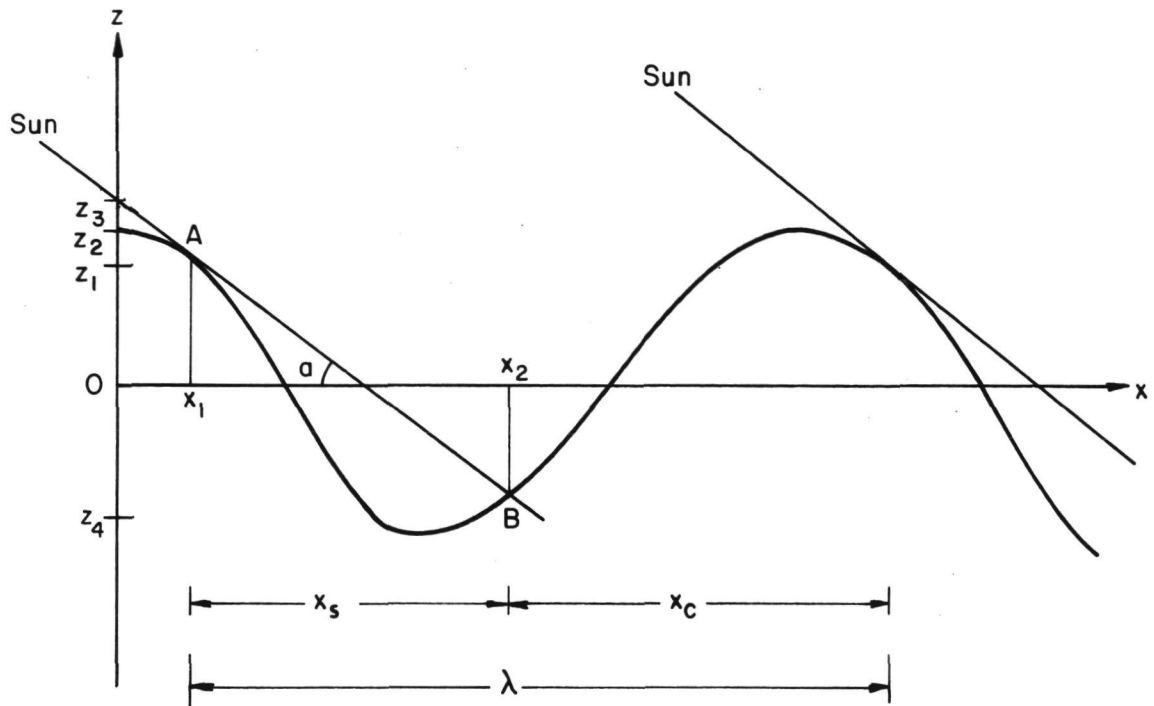


Figure A.1. Cross-sectional view of idealized wave pattern.

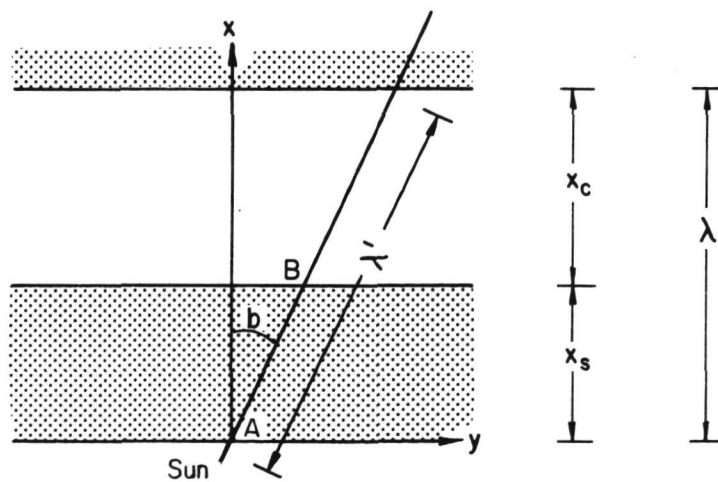


Figure A.2. Top view of same wave pattern as that shown in Figure A.1.

$$z = z_2 \cos \frac{2\pi}{\lambda'} x \quad (\text{A.2})$$

At A, the slope of the wave equation is the same as the slope of line AB. From (A.2), this slope is:

$$\frac{\partial z}{\partial x} = -\frac{2\pi}{\lambda'} z_2 \sin \frac{2\pi}{\lambda'} x = -\tan a \quad (\text{A.3})$$

We now substitute (A.3) into (A.1) at point A:

$$z_1 = -x_1 (\tan a) + z_3 \quad (\text{A.4})$$

Solve for  $z_1$  in equation (A.2) at point A:

$$z_1 = z_2 \cos \frac{2\pi}{\lambda'} x_1 \quad (\text{A.5})$$

Substitute (A.5) into (A.4):

$$z_3 = z_2 \cos \frac{2\pi}{\lambda'} x_1 + x_1 \tan a \quad (\text{A.6})$$

Similarly at point B:

$$z_4 = -(x_1 + x_s) \tan a + z_3 \quad (\text{A.7})$$

and:

$$z_4 = z_2 \cos \left[ \frac{2\pi}{\lambda'} (x_1 + x_s) \right] \quad (\text{A.8})$$

Therefore:

$$z_2 \cos \frac{2\pi}{\lambda'} x_1 = z_2 \cos \left[ \frac{2\pi}{\lambda'} (x_1 + x_s) \right] + x_s \tan a \quad (\text{A.9})$$

where from (A.3):

$$x_1 = \frac{\lambda'}{2\pi} \sin^{-1} \left( \frac{\lambda'}{2\pi z_2} \tan a \right) \quad (\text{A.10})$$

Equations (A.9) and (A.10) can now be solved for  $z_2$  which is the amplitude of the wave (see Fig. A.1).

## APPENDIX B

SELECTION OF SIGN FOR  $\beta_1$ 

The selection of  $\beta_1 > 0$  or  $\beta_1 < 0$  was, at first, determined by the process of elimination. Equation (3.94) was solved in each case, using both positive and negative values for  $\beta_1$ . In doing so, a certain trend became apparent. That is, for a selected sign for  $\beta_1$ , and certain ranges for  $\Delta u_0$ , equation (3.94) failed to converge on a solution. Thus, the sign of  $\beta_1$  for which equation (3.94) did converge, within this same range of  $\Delta u_0$ , would be used. This sign would then be maintained until either  $\beta_1$  or its coefficient became zero. The points where  $\beta_1$  changes sign are illustrated in Figure 3.7.

As a means of illustrating why equation (3.94) fails to converge for certain  $\beta_1$  and  $\Delta u_0$  a typical case will be described. The solution of equation (3.94) for this case will be determined at  $u_{01} = 0$ .

At this point equation (3.94) simplifies to:

$$\frac{c^2}{\chi_1} \left[ (\theta_{s1}\beta_2 + \theta_{s2}\beta_1) + (\theta_{s1}\Gamma_2 + \theta_{s2}\Gamma_1) \right] + g (\theta_{s2} - \theta_{s1}) = 0 \quad (B.1)$$

The following typical parameter values will be used:

$$\begin{array}{ll} \theta_{s1} = 350^\circ \text{ K} & \theta_{s2} = 370^\circ \text{ K} \\ T_1 = 200^\circ \text{ K} & T_2 = 210^\circ \text{ K} \\ N_1^2 = 2 \times 10^{-3} \text{ sec}^{-2} & N_2^2 = 3.8 \times 10^{-4} \text{ sec}^{-2} \end{array}$$

The values of  $N_1^2$  and  $N_2^2$  are both indicative of very thermally stable layers. Using these values and assuming  $(\theta_{s1}, \Gamma_2 + \theta_{s2}\Gamma_1) = 0$ , based on scale analysis of this case, (B.1) becomes:

$$\frac{c^2}{\chi_1} (\theta_{s1}\beta_2 + \theta_{s2}\beta_1) + g (\theta_{s2} - \theta_{s1}) = 0 \quad (B.2)$$

where:

$$\beta_1 = \pm \left[ \Gamma_1^2 + \chi_1 \left( \frac{N_1^2}{c^2} - \mu^2 \right) \right]^{\frac{1}{2}}, \quad \chi_1 = \frac{c^2}{\gamma RT_1} - 1 \quad (\text{B.3})$$

$$\beta_2 = + \left[ \Gamma_2^2 + \chi_2 \left( \frac{N_2^2}{c^2} - \mu^2 \right) \right]^{\frac{1}{2}}, \quad \chi_2 = \frac{c^2}{\gamma RT_2} - 1 \quad (\text{B.4})$$

Notice in this case  $N_2^2 > N_1^2$ . This is generally true since the air immediately above the tropopause is usually more stable than that immediately below.

At this point, one further simplifying assumption is made. Again, based on scale analysis:

$$\Gamma_1^2 = 0, \quad \chi_1 = -1 \quad (\text{B.5})$$

$$\Gamma_2^2 = 0, \quad \chi_2 = -1 \quad (\text{B.6})$$

The validity of these assumptions is not readily apparent at this point. However, the data from the case studies does indicate that solutions for  $c$  at  $u_{01} = 0$  are changed less than 10% under assumptions (B.5) and (B.6). Also, the results regarding the sign of  $\beta_1$ , without these assumptions, are the same as those we will obtain utilizing them. Thus, (B.3) and (B.4) become:

$$\beta_1 = \pm \left( \mu^2 - \frac{N_1^2}{c^2} \right)^{\frac{1}{2}} \quad (\text{B.7})$$

$$\beta_2 = + \left( \mu^2 - \frac{N_2^2}{c^2} \right)^{\frac{1}{2}} \quad (\text{B.8})$$

Now a wavelength of the same magnitude of those typically observed is chosen:

$$\lambda = 10^4 \text{ m}$$

Therefore:

$$\mu^2 = 3.95 \times 10^{-7} \text{ m}^{-2}$$

Under these circumstances, possible solutions for  $\beta_1 > 0$  will be investigated. First, we will look for a real solution for  $c$ . Since  $N_2^2 > N_1^2$ , the minimum real solution is:

$$c = \pm \left( \frac{N_2^2}{\mu^2} \right)^{\frac{1}{2}}$$

Using the given values for  $N_2^2$  and  $\mu^2$ , this minimum real  $c$  is:

$$c = 71 \text{ m/sec}$$

Upon substituting this value into (B.7), (B.8), and then (B.2) it is found that the first term of the left,  $\left[ \frac{c^2}{X_1} (\theta_{S_1} \beta_2 + \theta_{S_2} \beta_1) \right]$ , is greater than the second term,  $g(\theta_{S_2} - \theta_{S_1})$ . Also, any further increase in  $c$  causes even larger differences between these two terms. Therefore, a real solution for  $c$  when  $u_{O_1} = 0$  and  $\beta_1 > 0$  does not exist.

Next the possibility of either a complex or purely imaginary solution for  $c$  when  $\beta_1 > 0$  will be investigated. Rewrite (B.2) under the conditions (B.5) and (B.6):

$$c^2 \left[ \theta_{S_2} \left( \mu^2 - \frac{N_1^2}{c^2} \right)^{\frac{1}{2}} + \theta_{S_1} \left( \mu^2 - \frac{N_2^2}{c^2} \right)^{\frac{1}{2}} \right] = g(\theta_{S_2} - \theta_{S_1})$$

or:

$$c \left[ \theta_{S_2} (\mu^2 c^2 - N_1^2)^{\frac{1}{2}} + \theta_{S_1} (\mu^2 c^2 - N_2^2)^{\frac{1}{2}} \right] = g(\theta_{S_2} - \theta_{S_1}) \quad (\text{B.9})$$

Since  $g(\theta_{S_2} - \theta_{S_1})$  is real, then  $c$  must be the complex conjugate of the factor between the brackets. For example, let:

$$c = c_r + c_i i \quad (\text{B.10})$$

where  $c_r$  and  $c_i$  are real. Therefore:

$$\theta_{s_2} (\mu^2 c^2 - N_1^2)^{\frac{1}{2}} + \theta_{s_1} (\mu^2 c^2 - N_2^2)^{\frac{1}{2}} = c_r + c_i i \quad (\text{B.11})$$

Also:

$$(c_r + c_i i) (c_r - c_i i) = g(\theta_{s_2} - \theta_{s_1})$$

or:

$$c_r^2 + c_i^2 = g(\theta_{s_2} - \theta_{s_1}) \quad (\text{B.12})$$

Now substitute for  $g$ ,  $\theta_{s_1}$ ,  $\theta_{s_2}$ ,  $N_1^2$ ,  $N_2^2$ , and  $\mu^2$  from the given case into (B.11) and (B.12):

$$\begin{aligned} & [(7.6 \times 10^{-6})c^2 - (7.3 \times 10^{-3})]^{\frac{1}{2}} + [(7.4 \times 10^6)c^2 - (3.7 \times 10^3)]^{\frac{1}{2}} = \\ & c_r + c_i i \end{aligned} \quad (\text{B.13})$$

$$\therefore c_r = \pm (196 - c_i^2)^{\frac{1}{2}} \quad (\text{B.14})$$

Substitute (B.14) into (B.10):

$$c = \pm (196 - c_i^2)^{\frac{1}{2}} + c_i i \quad (\text{B.15})$$

Substitute (B.15) into (B.13):

$$\begin{aligned} & \{ [7.6 \times 10^{-6} (196 - c_i^2)^{\frac{1}{2}} - 7.3 \times 10^{-3}] + (7.6 \times 10^{-6})c_i i \}^{\frac{1}{2}} + \\ & \{ [7.4 \times 10^{-6} (196 - c_i^2)^{\frac{1}{2}} - 3.74 \times 10^{-2}] + (7.4 \times 10^{-6})c_i i \}^{\frac{1}{2}} = \\ & (196 - c_i^2)^{\frac{1}{2}} - c_i i \end{aligned} \quad (\text{B.16})$$

Since  $c_r$  and  $c_i$  are real, from (B.14) the following condition is imposed:

$$|c_i| \leq 14 \quad (\text{B.17})$$

First we will investigate the possible solutions where  $c_r = 0$  (i.e.,  $c$  is imaginary).

From (B.14):

$$c_i = \pm 14$$

If  $c_i = 14$  and  $c_i = -14$  are substituted into (B.16), a complex solution is obtained on the left side of the equation and a purely imaginary solution on the right side. Therefore, an imaginary solution for  $c$  in this case does not exist.

The only remaining possible solution is where  $c$  is complex. To examine this possibility, only the sign of each term will be dealt with. That is, if a term is greater than zero, it will be represented by {POS}, and if a term is less than zero by {NEG}.

First, we will examine the terms between the braces on the left side of (B.16). Notice, under condition (B.17):

$$(7.4 \times 10^{-6}) (196 - c_i^2)^{\frac{1}{2}} < 3.74 \times 10^{-2} \quad (\text{B.18})$$

$$(7.6 \times 10^{-6}) (196 - c_i^2)^{\frac{1}{2}} < 7.3 \times 10^{-3} \quad (\text{B.19})$$

Thus, the signs of (B.16) are:

For  $c_i > 0$ :

$$\begin{aligned} & [\{\text{NEG}\} + \{\text{POS}\}i]^{\frac{1}{2}} + [\{\text{NEG}\} + \{\text{POS}\}i]^{\frac{1}{2}} = \\ & \{\text{POS or NEG}\} - \{\text{POS}\}i \end{aligned} \quad (\text{B.20})$$

For  $c_i < 0$ :

$$\begin{aligned} & [\{\text{NEG}\} + \{\text{NEG}\}i]^{\frac{1}{2}} + [\{\text{NEG}\} + \{\text{NEG}\}i]^{\frac{1}{2}} = \\ & \{\text{POS or NEG}\} - \{\text{NEG}\}i \end{aligned} \quad (\text{B.21})$$

The formula for complex square root is defined as:

$$J = m + ni \quad (\text{B.22})$$

$$\sqrt{J} = \sqrt{\frac{|J|+m}{2}} + (\text{sign } i) \sqrt{\frac{|J|-m}{2}} i \quad (\text{B.23})$$

Notice, only with those roots that have a positive real component are dealt with. Therefore, (B.20) and (B.24) reduce to:

$$[\{\text{NEG}\} + \{\text{POS}\}i]^{\frac{1}{2}} + [\{\text{NEG}\} + \{\text{POS}\}i]^{\frac{1}{2}} = \{\text{POS}\} + \{\text{NEG}\}i \quad (\text{B.24})$$

$$[\{\text{NEG}\} + \{\text{NEG}\}i]^{\frac{1}{2}} + [\{\text{NEG}\} + \{\text{NEG}\}i]^{\frac{1}{2}} = \{\text{POS}\} + \{\text{POS}\}i \quad (\text{B.25})$$

Apply the form of solution given by (B.22) and (B.23) to equations (B.24) and (B.25):

$$\{\text{POS}\} + \{\text{POS}\}i \neq \{\text{POS}\} + \{\text{NEG}\}i \quad (\text{B.26})$$

$$\{\text{POS}\} + \{\text{NEG}\}i \neq \{\text{POS}\} + \{\text{POS}\}i \quad (\text{B.27})$$

Therefore, there are no complex solutions for  $c$  when  $u_{01} = 0$  and  $\beta_1 > 0$  for this case.

The conclusion, from all of this, is that at  $u_{01} = 0$ ,  $\beta_1 > 0$  will not necessarily have a solution. Therefore,  $\beta_1 < 0$  is selected to

determine the solution for  $c$ . Note that for  $\beta_1 < 0$ , (B.26) and (B.27) do not necessarily result due to the difference in sign between  $\beta_1$  and  $\beta_2$ .

As was mentioned earlier,  $c$  must be a continuous function of  $u_{o1}$ . Since we have chosen  $\beta_1$  (real)  $< 0$  at  $u_{o1} = 0$ , we must continue to use  $\beta_1$  (real)  $< 0$  until either  $\beta_1$  (real)  $= 0$  or the terms containing  $\beta_1$  as a factor have a real component equal to zero. The first condition,  $\beta_1$  (real)  $= 0$  is met at:

$$c = u_{o1} + \left( \frac{N_2^2}{\mu^2} \right)^{\frac{1}{2}} \quad (\text{B.28})$$

$$c = u_{o1} - \left( \frac{N_1^2}{\mu^2} \right)^{\frac{1}{2}} \quad (\text{B.29})$$

The latter condition is met at:

$$c = u_{o1} \quad (\text{B.30})$$

As is demonstrated in Figure 3.5,  $\beta_1$  does shift sign when (B.28) is true, and again, where (B.30) is true.

BIBLIOGRAPHIC DATA SHEET	1. Report No. CSU-ATSP-246	2.	3. Recipient's Accession No.
4. Title and Subtitle  GRAVITY SHEAR WAVES ATOP THE CIRRUS LAYER OF INTENSE CONVECTIVE STORMS		5. Report Date December 1975	
7. Author(s) James G. Stobie		6.	
9. Performing Organization Name and Address  Atmospheric Science Department Colorado State University Fort Collins, Colorado 80523		8. Performing Organization Rept. No. CSU-ATSP-246	
		10. Project/Task/Work Unit No.	
		11. Contract/Grant No.  NASA Grant NSG-1023	
12. Sponsoring Organization Name and Address  NASA Langley Hampton, Virginia		13. Type of Report & Period Covered Project Report	
		14.	
15. Supplementary Notes			
16. Abstracts  Recent visual satellite photographs of certain intense convective mid-latitude and tropical storms have revealed distinct concentric wave patterns. These waves appear as undulations in the top of the cirrus outflow of such storms, and are usually centered about the area of the most intense convection.  An analytical model for the generation and growth of these waves is proposed. A proposed initial generating mechanism similar to the effect noticed when a pebble is dropped into a calm pond is used to depict the penetration of the tropopause by overshooting convection. The model for wave growth involves instability due to the wind shear resulting from the cirrus outflow. This model is based on an equation for the waves' phase speed which is similar to the Helmholtz equation. It, however, does not assume an incompressible atmosphere, but rather assumes density is a logarithmic function of height.  (ABSTRACT CONTINUED BELOW)			
17. Key Words and Document Analysis. 17a. Descriptors  Gravity waves  Cirrus layer  Convective storms  Finally, the model is evaluated on the two mid-latitude and three tropical cases. The data indicate that shearing instability may be a significant factor in the appearance of these waves.			
17b. Identifiers/Open-Ended Terms			
17c. COSATI Field/Group			
18. Availability Statement		19. Security Class (This Report) UNCLASSIFIED	21. No. of Pages 116
		20. Security Class (This Page) UNCLASSIFIED	22. Price